TECHNISCHE UNIVERSITÄT MÜNCHEN

Lehrstuhl für Energiesysteme

Short-term measurement of high-temperature chlorine-induced corrosion and agglomeration during biomass and waste combustion

Elisa Alonso Herranz

Vollständiger Abdruck der von der Fakultät für Maschinenwesen der Technischen Universität München zur Erlangung des akademischen Grades eines

Doktor-Ingenieurs

genehmigten Dissertation.

Vorsitzender: Univ.-Prof. R. Macián-Juan, Ph.D.

Prüfer der Dissertation:

1. Univ.-Prof. Dr.-Ing. habil. H. Spliethoff
2. Univ. -Prof. Dr. rer. nat. F. Haider,
   Universität Augsburg

Die Dissertation wurde am 02.05.2011 bei der Technischen Universität München eingereicht und durch die Fakultät für Maschinenwesen am 11.10.2011 angenommen.

Vorwort

Die vorliegende Dissertation entstand im Rahmen meiner Tätigkeit als wissenschaftliche Mitarbeiterin am Lehrstuhl für Energiesysteme der Technischen Universität München. Ich möchte mich an dieser Stelle bei meinem Doktorvater Prof. Dr. -Ing. Hartmut Spliethoff für die mir jederzeit gewährte Unterstützung während der Promotionszeit bedanken, bei Prof. Dr. -Ing. Jürgen Karl, der verantwortlich dafür ist, dass ich eine Promotion im Lehrstuhl angefangen habe, bei Prof. Dr. -Ing. Dietmar Hein, der in den entscheidenden Momenten immer Zeit für einen guten Rat hatte und bei Prof. Dr. rer. nat. Haider, der die schwierige Aufgabe hatte, einem Ingenieur Physik beizubringen.

Diese Arbeit ist, zu meinem großen Vergnügen, das Ergebnis einer Teamarbeit. Ein Team, von dem ich viel gelernt und dem ich viel zu verdanken habe. Ein großer Dank gilt der Werkstatt. Ohne sie wären die in dieser Arbeit beschriebenen Laborversuche gar nicht möglich gewesen. Dem Sekretariat danke ich für die Geduld und die freundliche Unterstützung bei Anträgen, Rechnungen und weiteren bürokratischen Herausforderungen des Alltags. Den Studenten, die mit Semester- oder Diplomarbeiten, ein größeres oder kleineres Scherflein zu dem Ganzen beigetragen haben: Danke für Eure Motivation und Euer Engagement! Bei der Arbeitsgruppe der Universität Augsburg (Dr. S. Maisch, Prof. F. Haider und Prof. S. Horn) und bei der Fa. Corrmoran GmbH (Dr. B. Waldmann, Dr. D. Schrupp und B. Stöcker) bedanke ich mich für die Unterstützung mit den LPR-Messungen und vielem mehr. Den Mitarbeitern der Firma Martin GmbH, T. Weber, Dr. O. Gohlke und J.Horn, und der Firma CNIM, P. Seguin, Y. Laborel und M. Germany, sage ich danke für das Know-how, das entscheidend für die Durchführung der Messungen in der großtechnischen Anlage war. Danke auch an die Arbeitsgruppe von Åbo Akademi, insbesondere an unsere Gastförscherin D. Bankiewicz, mit der ich zusammen die Metallographic Tests durchgeführt habe.

Ein besonderer Dank gilt den zahlreichen und fleißigen Korrektoren dieser Arbeit: M. und K. Ottmann, Ch. Wieland, S. Kuhn, G. Balan, M. Murer, T. Stotko, R. Abad, M. Dreißig, K. Brodie und E. Alonso Herranz.

Schließlich geht an Philippe, an meine Familie, sowie an meine Freunde für ihre vertrauensvolle Unterstützung ein herzliches: ¡Gracias! Merci! Danke schön!

Kurzfassung

Die Verbrennung biogener Brennstoffe leistet einen wichtigen Beitrag zur Nutzung erneuerbarer Energien. Die Verfügbarkeit und die Energieeffizienz von Anlagen, die mit Biomasse oder Müll befeuert werden, ist allerdings aufgrund von Problemen wie der feuerseitigen Hochtemperatur-Chlorkorrosion und Agglomeration relativ niedrig. Diese Faktoren waren und sind Gegestand zahlreicher Forschungsarbeiten. Die zugehörigen Untersuchungen sind zeit- und kostenintensiv und der Wissensstand in diesem Bereich immer noch sehr begrenzt. In der vorliegenden Arbeit werden einige Möglichkeiten untersucht, Agglomeration und Korrosionsraten mittels kurzer Tests (< 1 Tag) zu quantifizieren. Korrosionsmessungen kurzer Dauer (8 bis 30 h) wurden in einer Versuchsanlage und in einem Kraftwerk durchgeführt. Dabei kamen drei unterschiedliche Messtechniken zum Einsatz, davon zwei offline (Metallographie und Eisenabtragsmessung) und eine online (linearer Polarisationswiderstand – LPR). Die Dauer der Versuche reichte nicht aus, um mit den offline-Techniken die Korrosion richtig zu quantifizieren. Dennoch konnte mit dem LPR-Verfahren eine deutliche Korrelation zwischen der Brennstoffzusammensetzung und dem Korrosionssignal online gemessen werden. Die Ergebnisse dieser Arbeit zeigen, dass eine etwas längere Versuchsdauer (~ 50 h) und kleine technische Anpassungen der Messanordnung eine vielversprechende Grundlage für Kurzzeitmessungen dieser Art darstellen.

Schlagwörter: Hochtemperatur-Chlorkorrosion, linearer Polarisationswiderstand, Biomasse, Online-Korrosionsmessung

Abstract

The combustion of biomass is one of the most important ways of harnessing renewable energies. However, the operational availability and efficiency of biomass and waste-fired facilities are relatively low due to problems such as high-temperature chlorine-induced corrosion and agglomeration on the fire-side. These issues have been investigated in laboratories, small-scale research facilities and power plants by methods that are generally expensive and time-consuming. This work aims to evaluate the feasibility of short-term tests (< 1 day) for quantifying corrosion and agglomeration. Short-term tests (8 to 30 h) were carried out in a small-scale facility and in a power plant using three different corrosion monitoring techniques: two offline (metallography and iron loss measurement) and one online (linear polarisation resistance – LPR). The duration of the tests did not suffice to quantify corrosion by means of offline techniques. However, a significant correlation between fuel composition and corrosion signal could be established online by means of LPR measurements. The results of this research show that slightly longer tests (~ 50 h) and minor changes to the LPR sensor provide a promising basis for the short-term measurement of this kind of corrosion.

Keywords: high-temperature chlorine-induced corrosion, Linear Polarisation Resistance, biomass, online corrosion monitoring.

Contents

List of figures

List of tables

List of abbreviations

AC	alternating current
AES	augen electron spectroscopy
ARMCO	American Rolling Mill Company
BSE	back-scattered electron microscopy
C	as subscript: counter (electrode, etc.)
CFB	circulating fluidised bed
DC	direct current
DIN	Deutsches Institut für Normung (German Institute for Standardization)
DIN EN	German implementation of a European norm
dm	dry matter
EDX	energy-dispersive X-ray spectroscopy
EfW	energy-from-waste [plant]
EIA	U.S. Energy Information Administration
EIS	electrochemical impedance spectroscopy
EN	electrochemical noise
ER	electrical resistance
EU	European Union
EU ETS	European Union Emissions Trading System
FBC	fluidised bed combustion
FTIR	Fourier transform infrared spectroscopy
GHG	greenhouse gas
HP	heat pipe
HT	high temperature
IPCC	Intergovernmental Panel on Climate Change
ISO	Internation Organisation for Standardization
KED	Kerntechnik Energie Dynamik [company]
KEMA	Kema company
LPC	linear polarisation conductance
LPR	linear polarisation resistance
MSW	municipal solid waste

NO_x	oxides of nitrogen (NO, NO_2, etc.)
PID	proportional-integral-derivative (controller)
ppmv	part per million by volume
PPSD	PowerPlantSimulator&Designer (software)
PVC	polyvinyl chloride
R	as subscript: reference (electrode, etc.)
RSP	winter rye straw pellets
RWW	recovered wood waste
S28	Sanicro28
SEM	scanning electron microscope
SH	superheater
STA	simultaneous thermal analysis
TGA	thermal gravimetric analysis
US	United States
US	United States
VDI	Verein Deutscher Ingenieure (The Association of German Engineers)
VGB	Vereinigung der Großkesselbesitzer e.V. (federation of the owners of large boilers in Germany)
W	as subscript: working (electrode, etc.)
WP	wood pellets
WP+S/Cl 0.02	wood pellets doped with S and Cl (S/Cl ratio: 0.02)
WP+S/Cl 0.8	wood pellets doped with S and Cl (S/Cl ratio: 0.8)
WP+S/Cl 1.5	wood pellets doped with S and Cl (S/Cl ratio: 1.5)
WP0.1%	wood pellets doped with 0.1% aqueous $ZnCl_2$ solution
WP0.5%	wood pellets doped with 0.5% aqueous $ZnCl_2$ solution
WSP	(winter) wheat straw pellets
wt.%	% by weight
XRF	X-ray fluorescence

List of symbols

(aq)	aqueous phase	
(g)	gas phase	
(l)	liquid phase	
(s)	solid phase	
A	surface involved	m^2, cm^2, dm^2
α	symmetry factor	-
$\bar{a}_m$	average crystallisation activity	-
$\bar{a}$	average reaction activity	-
a_j	reaction activities	-
Aj, Bj	coefficient	-
a_{mi}	crystallisation activities	-
b	calibration factor	Vm/(As)
β	proportionality coefficient	-
Cc	capacitance of the counter electrode	F
$C_{electrolyte}$	capacitance of the electrolyte	F
C_W	capacitance of the working electrode	F
d,D	diameter	m, mm, µm
Δh	thickness loss	µm
δh_{max}	maximal standard deviation of an individual measured thickness loss	µm
δh_{point}	standard deviation of the mean values	µm
d_p	diameter of bed particle	mm
Δp	pressure drop in the bed	mbar
d_{sv}	surface-volume diameter	m
d_v	volume mean diameter	m
ε	porosity	m
E	potential	V
e^-	electron	-
ε_L	fluidisation porosity	-
E_o	free potential of an electrochemical system, free	V

	corrosion potential	
$E_{o,j}$	free corrosion potential at point j	V
F	Faraday constant	C/mol
G	polarisation conductance	mA/V
G_j	polarisation conductance at point j	mA/V
H	height of fixed bed	m
η	polarisation	V
h	layer thickness	µm
η	polarisation	V
$\bar{h}$	mean value of the thickness	µm
ηC	potential drop in the counter electrode	V
η_c	crystallisation polarisation	V
η_D	charge transfer polarisation	V
η_d	diffusion polarisation	V
η_{el}	potential drop in the electrolyte	V
h_j	metal thickness at point j	µm
H_L	height of fluidised bed	m
η_r	reaction polarisation	V
η_W	potential drop in the working electrode	V
η_Ω	ohmic resistance polarisation	V
I	net current	A
i	current or current density (depending on context)	A/m^2
i_a	anodic current (density where specified)	A/m^2
i_c	cathodic current (density where specified)	A/m^2
I_j	measured current at point j	A
i_{max}	maximal current when transport happens much faster than the electrochemical reaction	A/m^2
i_o	exchange current; corrosion current (density where specified)	A/m^2
k	proportionality coefficient	-
kWth	thermal kilowatt	kW_{th}
l,L	length	m
M	molar mass	kg/kmol, g/mol
m	mass	kg

n	number of measurements	-
ν_j	chemical activity of each compound	-
p	pressure	bar, mbar
P_j	measuring point j	-
p_{sat}	saturation pressure	bar
R	universal gas constant	J/(mol K)
r	corrosion rate	µm/h, mm/a, m/s
ρ	metal density	kg/Nm^3
ρ_b	bulk density	kg/Nm^3
Rc	resistance of the counter electrode	Ω
R_D	charge transfer resistance	Ω
R_d	diffusion resistance	Ω
Re	Reynolds number	-
$R_{electrolyte}$	resistance of the electrolyte	Ω
ρ_p	particle density	kg/Nm^3
R_r	reaction resistance	Ω
R_{total}	total reaction of the electrochemical system in the corrosion head	Ω
R_Ω	ohmic resistance	Ω
R_W	resistance of the working electrode	Ω
S	fluidisation factor	-
S/Cl	S to Cl molar ratio	-
τ	time required for the corrosion signal to approach the actual corrosion rate	s
t	time	s,min,h,a
T	temperature	°C
τ'	time required for the corrosion signal to continue with the tendency from the previous run	s
t_{ex}	exposure time	s,min,h,a
T_{sat}	saturation temperature	°C
U	measured external voltage	V
U_f	fluidisation velocity	m/s
U_j	measured external voltage at point j	V
U_{mf}	minimum fluidisation velocity	m/s

V	volume of the bed material	ℓ
V_{flow}	volumetric flow rate at a point	Nm^3/h
ψ	particle form factor	-
z	number of involved electrons	-
Z^+	cation	-
σ	standard deviation	μm

1 Motivation and objectives

At the beginning of the 21st century, global power generation faces three main challenges. The first of these is the worldwide increase in energy demand. The world's population growth and economic development are responsible for an annual rise in energy consumption figures. Heat and power generation technologies must be developed further in order to satisfy the demand. In the last decades this increase has been driven particularly by the rapid development of some emerging economies such as China and India. The US Energy Information Administration (EIA) predicts an increase of 49% in the global energy consumption from 2007 to 2035 [1].

One consequence of the increasing energy demand, and this is the second challenge, is the shortage of fossil fuels and the consequent need for alternative energy sources. Although fossil fuel production still increases yearly, the amount of existing fossil fuels is finite. Fossil fuels will run out. The EIA estimates that oil production will reach a peak between 2021 and 2110 [2]. At present, the fossil fuel consumption is still increasing worldwide, but the tendency is not sustainable and alternative energy sources must be investigated.

The last main challenge is the reduction of greenhouse gas (GHG) emissions. The Intergovernmental Panel on Climate Change (IPCC) reports that "*most of the observed increase in global average temperatures since the mid-20th century is very likely due to the observed increase in anthropogenic GHG concentrations*" [3]. Anthropogenic GHG emissions are assumed to have an influence on the reported climate change. In order to prevent the dangerous consequences of a climate change, most industrialized countries signed a treaty in Kyoto committing themselves to reduce their greenhouse gas emissions [4]. In Europe for instance, an emissions trading system (EU ETS) regulating the buying and selling of emission allowances has been established. Since a large proportion of the GHG emissions can be attributed to the traditional energy supply based on fossil fuels, it is mainly the energy suppliers who are affected by and involved in the ETS.

The main strategy worldwide to face these three challenges is to improve energy efficiency on the one hand and to increase the share of renewable energies on the other hand. For example, the European Union (EU) has defined the goal to reduce CO_2 emissions by 20%, to increase the share of renewables to 20% and to decrease energy demand by 20% by 2020 [5, 6]. These goals are the main driving forces behind European research in the field of energy conversion. Current research can be divided into four main streams:

- increasing the efficiency of existing technologies
- development of new technologies
- CO_2 sequestration
- use of renewable energy sources

This work focuses on one type of renewable energy source: the combustion of renewable solid fuels. Renewable solid fuels are byproducts from agriculture (straw, etc.) and forestry (logging remains), energy crops (miscanthus, triticale, etc.), industrial waste (demolition wood, etc.) and organic waste (organic fraction of municipal solid waste (MSW), sewage sludge, etc.). As already mentioned above Europe aims to cover 20% of its electricity demand with renewable sources by 2020 [6]. At present, renewable solid fuels generate about 15% of the electricity obtained from renewable sources and about 2% of the total electricity production in Europe [7]. According to the statistics of the German Federal Environment Ministry, biomass accounted for more than 50% of the energy generated from renewable sources in 2009 [8].

The main advantage of renewable fuels in comparison to fossil fuels is that they do not run out, are almost CO_2-neutral and can be produced locally. The main disadvantage is that they usually have lower calorific values and contain more water, ash and impurities than standard fossil fuels. These disadvantages result in a problematic behaviour during combustion. Plants firing renewable fuels have generally lower operational availabilities than plants firing coal or gas. Figure 1.1 shows the results of a study carried out by VGB, in which the availability of several German biomass and waste wood plants (from 5 to 20 MW_{el}) was investigated [9]. As a reference, the average availability of German hard coal power plants in 2009 has been included (8000 h/a) [10]. It is noteworthy that the operating hours of most of the biomass plants in Figure 1.1 are below 8000 h/a. These availabilities are usually also far below the design values of the plants, thus threatening their profitability [11].

Figure 1.1: Availability of different biomass power plants (adapted from [9])

Figure 1.2 shows the reasons for the limited operation times and the frequency of outages mentioned by the operators [9]. This work deals with two of the problems listed: corrosion and agglomeration (included in the “fluidised bed” factor in Figure 1.2). A typical example of corrosion damage is the premature failure of the superheater tubes of the plant due to their constant exposure to high temperatures and a corrosive atmosphere. In fluidised bed reactors the agglomeration of the bed particles results in big clumps that fall down to the bottom of the bed and can lead to its defluidisation. Both problems are related to the high alkali and chlorine content of renewable fuels compared to fossil fuels.

Avoiding high temperatures and using wood-based renewable fuels with low alkali and chlorine content helps to reduce such problems. However there is still a great lack of understanding concerning the mechanisms governing corrosion and agglomeration. At the moment the rising price of wood-based fuels is forcing plant operators to increase efficiency or to use more “problematic” renewable fuels. Therefore further research is necessary in this domain.

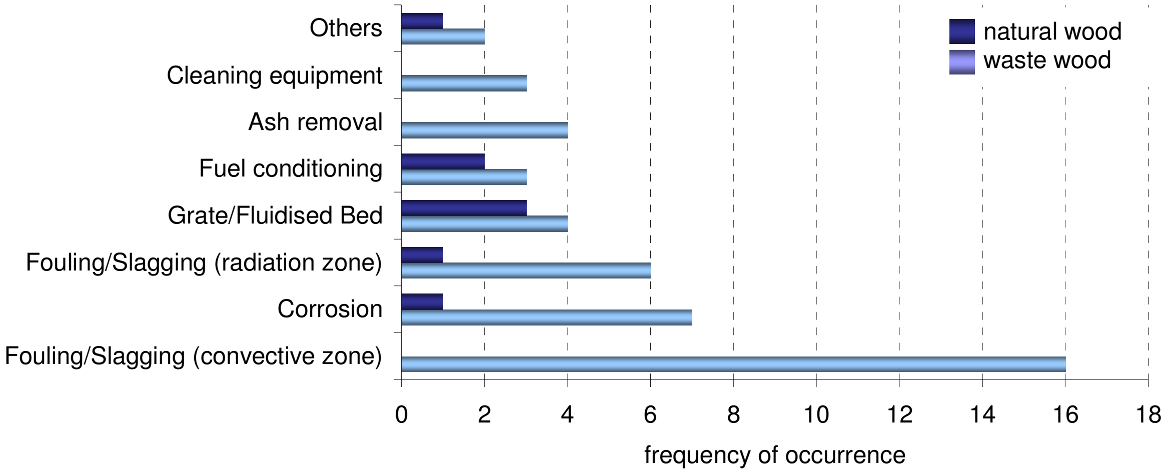

Figure 1.2: Factors limiting plant operation (adapted from [9])

A better understanding and control of corrosion and agglomeration benefits

- existing and future biomass- and MSW-fired plants aiming to increase their availability and efficiency
- corporations producing agricultural, forestry, household or industrial waste of high calorific value and
- operators of fossil fuel plants interested in the co-combustion of biomass in order to reduce CO_2 emissions whilst aiming to increase their efficiency towards the "best available technology" guidelines.

One option for the investigation of the impact of corrosion and agglomeration on plant operation is to carry out tests in a laboratory. Laboratory conditions are close to ideal: test parameters are well known and can be controlled precisely, accurate scientific measuring equipment is available, no perturbations arise and long-term tests are possible. The typical approach of laboratory corrosion tests is the use of probes of the material of interest that are exposed to high temperatures in an oven with a controlled atmosphere. In order to study the influence of deposits on the corrosion mechanism the probes are covered with deposits extracted from power plants or with synthetic mixtures prepared in the laboratory. Typical exposure times are 100 to 500 hours. This kind of test is essential in order to understand the corrosion mechanisms and the influence the different test parameters have on them. On the basis of this knowledge a detailed corrosion theory can be developed. However, these mechanisms are not yet fully understood and laboratory results cannot easily be extrapolated to real conditions since the conditions in a power plant are very different to those in the laboratory.

The second experimental approach to understanding corrosion and agglomeration is the analysis of samples which have been exposed to the flue gas of a power plant. Water- or air-cooled corrosion probes are introduced into the boiler for a certain period of time and analysed in the laboratory. However the control and monitoring of the operational parameters in a power plant is also subject to some important limitations:

- due the fact that in a power plant the first priority is the controlled operation of the plant, the variation of operational parameters in order to study their influence on corrosion is limited and extreme conditions cannot be tested
- The parameters of a power plant are often strongly correlated so that they cannot be investigated separately.
- The reaction of the plant to changes in the input parameters is slow and tests are usually time-consuming.
- The number of measuring points is typically much smaller than in a laboratory test rig, the laboratory equipment is often not able to stand the extreme conditions at the plant (dust and gas emissions, high temperatures, etc) and in most of the plants only standard and less accurate measuring devices can be used.

Series of measurements in a power plant have the advantage that tests are carried out under real conditions and thus “real” corrosion rates can be measured. However, due to all the factors mentioned above it is often difficult to correlate the measured corrosion rates with the test parameters and to draw conclusions that can be extrapolated to other plants.

To this day the corrosion (and agglomeration) behaviour of renewable fuels cannot be accurately predicted. There is a lack of information for plant operators planning new facilities, looking for alternative fuels or facing corrosion problems in their existing facility. Small-scale tests represent an intermediate approach. They reproduce the facility on a small scale and usually in a simplified way. Some (usually not all) parameters are well known and controlled whilst conditions are closer to those in a real plant than they are in the laboratory. The flue gas from a small-scale facility, where combustion takes place, is more similar to the flue gas in the power plant than the synthetic mixtures used in the laboratory. Concerning measuring variables there are more measuring points and more measured variables when compared with power plant tests and the facility reacts faster to changes in input parameters.

Despite this, only few investigations on fuel corrosion behaviour during short-term tests in small-scale facilities are available in the literature. Corrosion progress in the material after some few hours of exposure is minimal and difficult to measure with standard measuring techniques. New approaches are needed and therefore the aim of this work is:

1. to evaluate the feasibility of short-term tests (~ 8 h) in a small-scale fluidised bed reactor (50 kW_{th}) in order to study the correlation between combustion parameters and the behaviour of renewable solid fuels in terms of corrosion and agglomeration.
2. to compare different corrosion monitoring techniques for the short-term measurement of corrosion.

Therefore, short-term tests in a small-scale facility will be carried out. In the tests different corrosion probes will be exposed to flue gases for a relatively short period of time (8 to 30 h). Straw, wood and doped wood pellets will be used as fuels. Three different corrosion monitoring techniques will be compared:

- *Metallography* as a standard measuring technique
- *Iron loss* as a measuring technique proposed within the framework of this research
- *Linear Polarisation Resistance* (LPR) as an online electrochemical measuring technique that has recently been developed for its application in power plants.

The short-term behaviour of the three above-mentioned corrosion monitoring techniques will be analysed both theoretically and experimentally and will be discussed. In addition to this, the short-term agglomeration behaviour of the fuels tested will be investigated. Finally, measurements will be carried out in a power plant for comparison.

After a short introduction to high-temperature corrosion in chapter 2 the small-scale facility used for this work will be described in chapter 3. Chapters 4, 5 and 6 present the results of the three small-scale series of measurements: metallography, iron loss and LPR respectively. Chapter 7 investigates the observed short-term agglomeration behaviour of the fuels tested. The results of the measurements carried out in the power plant are included in chapter 8. All the results obtained are analysed and discussed in chapter 9, which includes the main conclusions drawn from this work.

2 Theory

In this chapter a short introduction to high-temperature chlorine-induced corrosion is given. Due to the complexity of the topic and the vast amount of information available in the literature, the aim of this introduction is to offer the reader an overview of current knowledge and the main literature sources on the subject, where more detailed information can be found.

2.1 High-temperature chlorine-induced corrosion

According to the ISO standard 8044 [12] corrosion is defined as a “physicochemical reaction (often of electrochemical nature) between a metal and its environment that results in changes in the properties of the metal, and which may lead to significant impairment of the function of the metal, the environment, or the technical system, of which these form a part”. Due to its many fields of application the term corrosion is subdivided into different categories. This work deals with one specific sort of corrosion: so-called high-temperature chlorine-induced corrosion [13].

In a power plant fired by a solid fuel the combustion of the fuel results in a high-temperature flue gas (800 to 1200°C). The main combustion technologies for solid fuels are explained in [14]. From its generation in the furnace until its emission to the atmosphere this flue gas flows through different heat exchangers transferring as much energy as possible to the water-steam path. The main aim is to generate high-temperature steam in order to obtain heat or to drive a steam turbine and produce electricity.

After some operation time, general corrosion (as defined in [12]) on the fireside of the heat exchanger’s walls is observed. The typical corrosion rates of the superheaters in a state-of-the-art coal power plant are about 0.1-0.2 mm/year [15]. Due to this metal loss the superheaters in such power plants have to be replaced every ten to twenty years. These costs are born by the power plant operator or manufacturer, included in the financial plans of the plant and accepted as normal. In some plants however, additional corrosion effects (pitting, selective corrosion, etc.) and much higher corrosion rates can cause a premature failure of the heat exchangers. Corrosion rates of the superheaters in these cases can reach 2 mm/year. In the case of such metal losses superheaters must be replaced almost yearly and this entails very high costs for the power plant operator or manufacturer [16]. A comprehensive report on typical corrosion-induced failures in energy-from-waste and biomass power plants can be found in [17].

In the work of Nielsen *et al.* [13] this kind of corrosion is called high-temperature chlorine-induced corrosion (HT Cl-corrosion). According to the norm it can be defined as a physicochemical reaction between the heat exchanger metal and the high-temperature flue gas from chlorine-containing fuel, causing a rapid metal loss (which in turn results in cracks and pitting or other changes in the properties of the metal). Consequently, the heat exchanger has to be repaired or replaced before schedule due to the influence of its environment (the hot flue gas).

The main components of the high-temperature materials used for the fabrication of steam superheaters are Fe, Cr and Ni with some other minor components (e.g. Mo). In the following discussion Fe will be used for the examples but a similar argumentation (with different corrosion mechanisms) can be applied to Cr and Ni.

The following parameters have proved to play an important role in this kind of corrosion:

- flue gas temperature
- tube wall temperature
- Cl content in the flue gas (Cl_2(g), HCl(g) or NaCl(g))
- S content in the flue gas (SO_2(g) or SO_3(g))
- alkali chlorides (KCl, NaCl, $CaCl_2$ (g,s or l)) and other chlorides ($ZnCl_2$, $PbCl_2$, etc.)
- O_2 content in the flue gas: oxidizing or reducing atmosphere
- thermal gradient in the deposits

- flue gas velocity

In the German literature on energy-from-waste plants the corrosion potential is often graphically represented as a function of the flue gas temperature and the tube wall temperature in the so-called Flingern corrosion diagram (see Figure 2.1). According to Foster *et al.* [18] the diagram is the result of long-term experience of the operators on the German plant Düsseldorf-Flingern. They exhaustively examined corrosion rates at the plant and displayed them as a function of flue gas temperature (X-axis) and tube wall temperature (Y-axis). In the diagram, zones of high and low corrosion risk can easily be identified. It can be seen that the high corrosion zone is located in regions with high flue gas and high tube wall temperatures. This diagram is not based on theoretical predictions but on measured values from a real plant. Although extrapolation of this correlation to other plants is risky, this diagram has proved to be useful as an orientation for the design and planning of new plants. Warnecke added a further region as a function of a new parameter: the flue gas velocity (5 -10 m/s) near the wall's surface [16] (also seen in Figure 2.1).

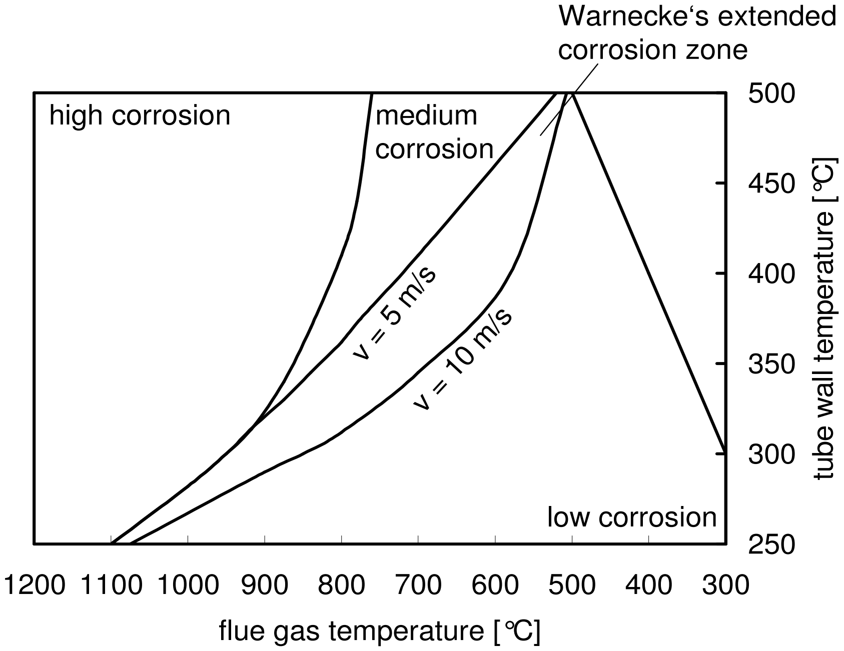

Figure 2.1: The Flingern corrosion diagram (adapted from [16])

It is widely accepted that chlorine, whether in the flue gas or in the deposits, in solid or liquid form, plays the most important role in this kind of corrosion.

2.1.1 Corrosion mechanisms

A large number of corrosion mechanisms in form of different reactions with several participating chemical species are proposed in the literature to explain HT Cl-induced corrosion. It is therefore outside the scope of this work to discuss each proposed mechanism whose applicability may often be restricted to the particular conditions under which it was investigated. The aim of this section is to give an overview of what all the theories have in common and to classify their differences. The corrosion mechanisms have been divided into two main categories, distinguished by certain basic characteristics: gaseous-phase and molten-phase corrosion.

2.1.1.1 Gaseous-phase corrosion

In this mechanism the corrosion agent chlorine is present in gaseous form. Nielsen *et al.* [13] describes in detail the two properties of chlorine mainly responsible for its high corrosivity:

- Chlorine is able to penetrate metal oxide layers. Other corrosive species also present in the flue gas like O_2 or SO_2 are stopped by the oxide layer. In the corrosion reaction $Fe + O_2 \rightarrow FeO, Fe_2O_3, Fe_3O_4$, for instance, the corrosion agent is O_2 and once an oxide layer of a certain thickness has formed, the contact between the O_2 and the metal is hampered and corrosion almost stops. If chlorine is present, the oxide layer is only a barrier for O_2 but not for chlorine, which is able to reach the metal surface. It is still not fully understood how this penetration occurs. The process is too fast to be associated with any kind of diffusion (solid, grain boundary or molecular). Grabke *et al.* [19] suggest the creation of fast diffusion paths. Under the oxide layer, the chlorine partial pressure is high and $FeCl_2$ is thermodynamically stable. Figure 2.2 shows the stability diagram (called Ellingham-Pourbaix diagram) of iron chlorides and oxides for 727 °C (similar diagrams can be found for Cr and Ni). It can be observed that $FeCl_2(g)$ is thermodynamically stable if Fe comes into contact with a high Cl_2 partial pressure ($\log pCl_2 > -13$ atm) at low O_2 partial pressures ($\log pO_2 < -20$ atm).

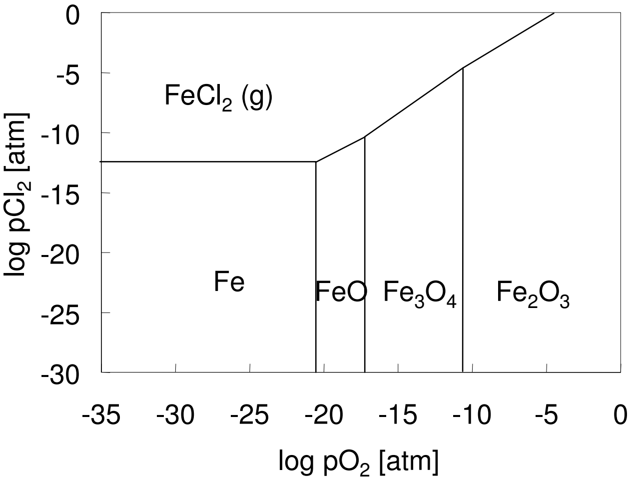

Figure 2.2: Stability diagram of Cr/Fe/Ni-O-Cl at 727 °C (adapted from [13])

- Vapour pressures of the metal chlorides are high (above 10^{-4} atm) and increase sharply with the temperature. Figure 2.3 shows vapour pressures of chlorides as a function of the temperature (adapted from [13]). For vapour pressures over 10^{-4} atm volatilisation of the metal chlorides is said to be the dominant factor in this corrosion mechanism [13].

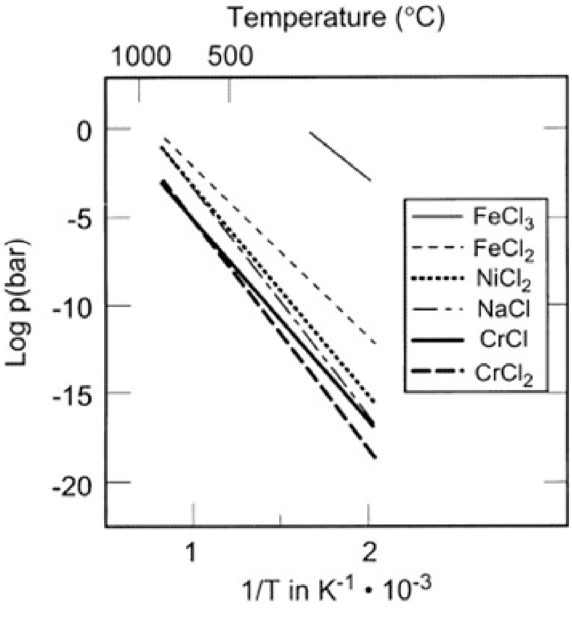

Figure 2.3: Vapour pressures of condensed Fe, Ni, Na and Cr chlorides (source [13])

In Figure 2.3 it can be seen that for temperatures above 500 °C chloride vapour pressures reach this value. In this case, the chlorides formed at the metal surface do not form a stable chloride layer like the oxide layer above them. The investigations of Waldmann *et al.* show that the chloride and oxide layers grow up to a certain thickness and then stop growing. At high temperatures (above 500 °C) $(FeCl_3)_2$ is highly volatile and is assumed to be responsible for the iron transport from the metal through the stationary chloride layer; it evaporates and may escape from the metal surface through the oxide layer into the environment (gaseous atmosphere) taking iron with it. A description of the corrosion mechanism proposed by this group can be found in [20-22].

Presumably the increase in volume from Fe to $FeCl_2$ (V_{FeCl_2}/V_{Fe} ~ 6 [23]) may cause additional spalling or chipping of the oxide layer so that after chloride formation other corrosive species (e.g. SO_2) can reach the metal surface. Figure 2.4 shows the resulting chlorine cycle.

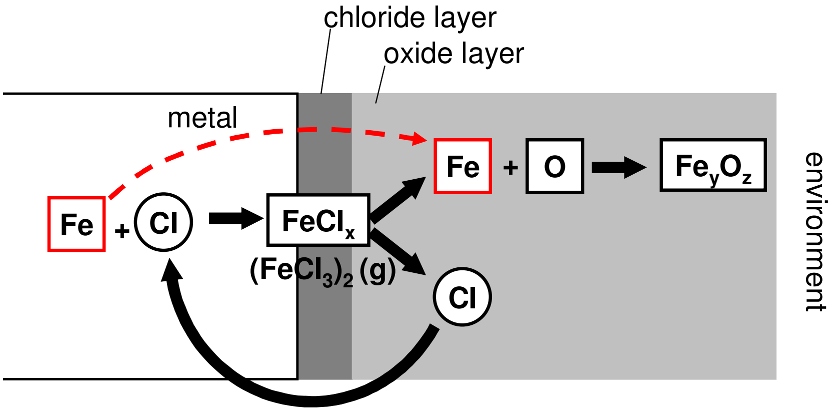

Figure 2.4: Chlorine vapour corrosion cycle (adapted from [13])

2.1.1.1.1 Typical corrosive atmospheres of gaseous-phase corrosion

Oxidizing conditions resulting in active oxidation: The term “active” describes a corrosion process without reaction constraints, see [12]. After the evaporated chlorides diffuse through the oxide layer, they come into contact with the environment. Under oxidizing conditions a high O_2 partial pressure prevails in the environment and chlorides are converted into oxides liberating chlorine. Thus the chlorine initially bound in a chloride is available again for the formation of new chlorides, i.e. chlorine is recycled in the process and acts as a carrier of Fe ions from the metal surface to the oxide layer. This explains why small amounts of chlorine are enough to cause high corrosion rates. Probably due to the above-mentioned change in volume, the new oxides form a low-density, non-protective layer. This results in a constant corrosion rate since nothing inhibits the reaction.

Reducing conditions: Reducing conditions prevail in the first regions of the flue gas path as a result of low oxygen concentrations in the first zone during staged combustion, inhomogeneous mixture of fuel with air or cleaning actions in the boiler. According to Hupa *et al.* [24] low O_2 concentrations in the environment prevent the formation of an oxide layer and evaporated chlorides escape very easily from the metal surface. This results in high corrosion rates.

2.1.1.1.2 Chlorine sources of gaseous-phase corrosion

The origin of the chlorine coming into contact with the metal can be described by two possible scenarios: the existence or absence of deposits.

No deposit: The corroded metal component of the boiler (tube, wall, etc) is covered by an oxide layer (rust) without any significant deposits. Chlorine in form of HCl(g), Cl_2(g) or alkaline chlorides (e.g. NaCl(g)) is present in the flue gas.

Deposit: The wall or tube is covered by a thick deposit under which the corrosion of the tube occurs. Chlorine is present in chloride-rich solid deposits (NaCl(s), KCl(s), $CaCl_2$(s), $ZnCl_2$, $PbCl_2$, etc) and is released when deposits react chemically with the flue gas or the oxide layer. Several mechanisms are proposed in the literature: (1) sulphation of chlorides with $SO_{2/3}$ in the flue gas; (2) reactions of chlorides with the oxide layer and (3) other mechanisms. No consensus has been reached on this point.

2.1.1.1.3 Characteristics of gaseous-phase corrosion: example

This corrosion mechanism can be identified by a very uniform corrosion over the metal surface [12]. Figure 2.5 left shows the typical appearance of a superheater tube affected by this kind of corrosion. A more or less uniform corrosion can be observed over the whole surface of the tube. Under the microscope well-defined horizontal layers of different composition can be observed, see Figure 2.5 right. In this Figure the white layer at the bottom is the metal surface. Close to the metal surface a thin layer of chlorine is typically found, followed by an iron oxide layer and a matrix of chlorides, sulphates and oxides that is typically the inner part of the deposit. For fuels with high chlorine content, such as MSW, the small amounts of chlorine near the metal surface can form a layer of some micrometers thickness. In some cases there is a sulphur rich layer between the chlorine and the oxide layer. According to [20] the thickness of both chloride and oxide layer reaches a constant value after a certain time.

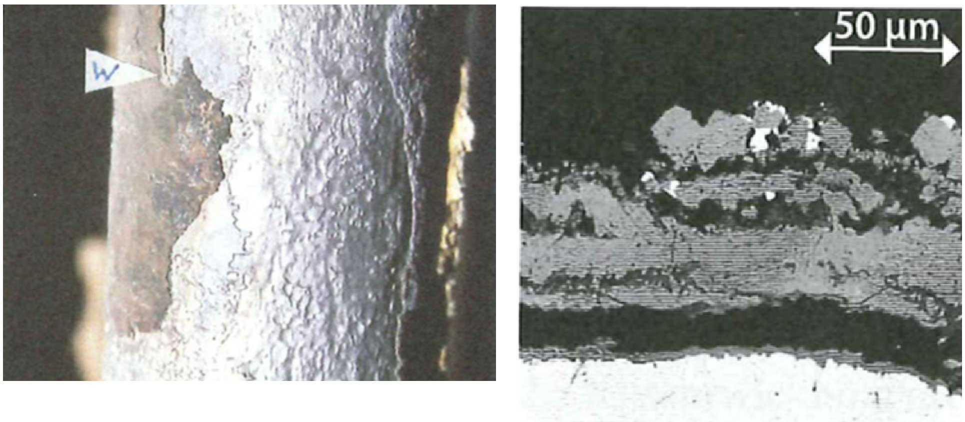

Figure 2.5: Example of gaseous-phase corrosion (adapted from [17])

2.1.1.2 Molten-phase corrosion

If the deposits on the wall or tube melt, the transport of the ions participating in the corrosion reaction is accelerated. The molten phase acts as an electrolyte for the corrosion reaction. In the liquid phase reactions proceed much faster and this mechanism can also be responsible for high corrosion rates.

The melting points of the main chlorides contained in the deposits can be found in [13]. Mixtures of these chlorides can form low-melting eutectics with melting temperatures far below 400 °C.

The dominant reaction mechanisms in this kind of corrosion are even less understood than those involved in gaseous-phase corrosion. Some mechanisms are evaluated in [23].

2.1.1.2.1 Characteristics of molten-phase corrosion: example

This corrosion mechanism can be identified by small cavities in the metal surface [12]. Figure 2.6 left shows the typical appearance of this kind of corrosion. In Figure 2.6 right, rounded regions (lacking sharp edges) characteristic of molten phases are observed. They typically show a very homogeneous composition, due to effective mixing in the liquid phase.

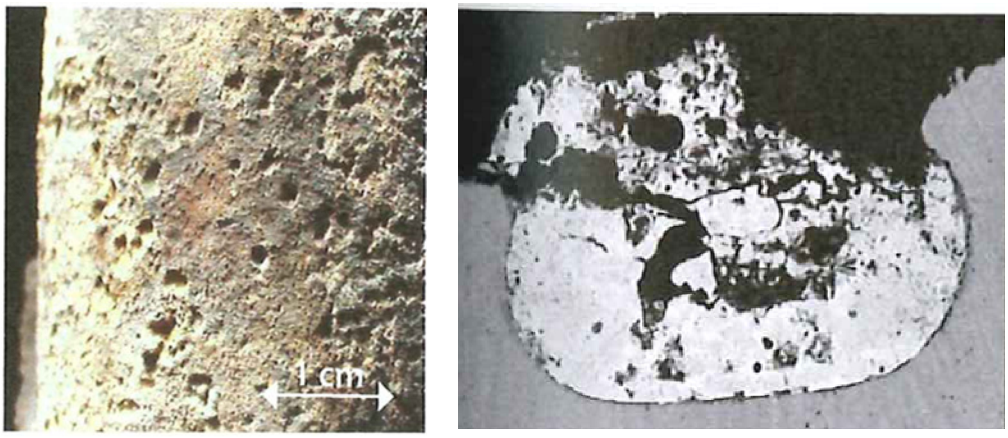

Figure 2.6: Example of molten-phase corrosion (adapted from [17])

2.1.2 Corrosion kinetics

Corrosion kinetics has been studied extensively under laboratory conditions. The thickening of the oxide layer on probes and metal loss (in terms of mass) on their surfaces have been described in the laboratory experiments of [23-25] and [26-29] under conditions closely resembling those of power plant superheaters (referred to as “superheater conditions” in the following).

The corrosion rate r is calculated as the metal loss (mass m or thickness h) per unit time ($dm/dt\,[kg/s], dh/dt\,[m/s]$). According to Schroer *et al.* [23] the corrosion rate can be expressed as:

- the decrease in thickness of the tube wall, although this is often difficult to measure;

- the distance between the metal surface before corrosion and after corrosion (in this case the material surface must be marked with an inert marker before the tests so that it former position can be identified after corrosion) or
- the thickness of the scale formed on the metal during the experiment.

Kinetic laws can be classified as linear, parabolic or paralinear [23] (see Figure 2.7). According to this source the metal losses observed under superheater conditions predominantly adhere to a paralinear kinetic law. The paralinear law may be interpreted as the result of the superposition of simultaneous parabolic and linear mechanisms. At the beginning of the exposure corrosion proceeds uninhibited and therefore the corrosion rates are high. If some of the reactions involved are physically or chemically restrained (for instance due to the formation of protective oxide layers, etc.) the corrosion rate decreases. In a system where corrosive conditions are not changed and a steady state is reached a constant corrosion rate is observed.

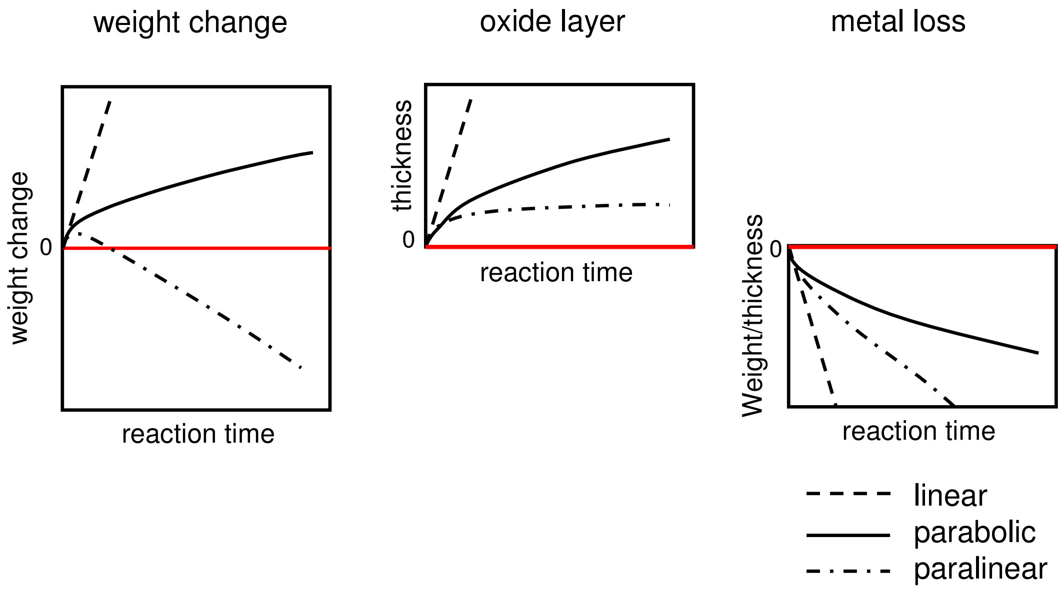

Figure 2.7: Main laws of corrosion kinetics (adapted from [23])

This introduction aims to present some basic concepts of high-temperature chlorine-induced corrosion that are considered necessary for the understanding of the later sections in this work. The reader will find more detailed information in the following publications:

- corrosion models: different corrosion models are proposed in the works of Nielsen, Kawahara, Warnecke and Krause [13, 16, 25-27].
- general surveys of literature on high-temperature corrosion: Schroer [23] and Nielsen [13] give an extensive review of the literature on corrosion in Energy-from-Waste (EfW) and biomass plants; references to a large number of research papers are included.
- laboratory measurements: documentation of many laboratory tests has been published by the research groups of Spiegel, Jensen, Hupa, Schütze and Brossard [24, 28-35].
- power plant measurements: results from power plant corrosion investigations can be found among others in the work of Jensen, Spiegel, Herzog, Kawahara, Waldmann, Warnecke, Hupa and Brossard [17, 23, 24, 26, 29-31, 33-35][36-38].

2.1.3 Current HT corrosion monitoring techniques in power plants

Although techniques for measuring corrosion are applied commercially in a number of industries, the complexity of the corrosion processes causing metal loss and the particularly demanding conditions in solid fuel combustors and boilers are responsible for their limited applicability in the field of power plants fired by solid fuel [39]. In this work the main state-of-the-art corrosion monitoring techniques are discussed and evaluated. The existing techniques can be classified as follows:

1) Metal loss techniques are defined as methods that measure changes in a physical property of the material due to corrosion.
    a) Metallography: Probably the most widely used technique to measure the corrosion of a component of a power plant is to observe its cross section with a scanning electron microscope (SEM). Thus the thickness and microstructure of deposits or oxide layers can be determined. As already mentioned, this monitoring technique is one of the standard techniques for the study of corrosion in boilers [40]. The

corroded components are extracted from the boiler and studied in the laboratory. In the previous section references to some laboratory research groups were given. With additional techniques such as back-scattered electron imaging (BSE) and energy-dispersive X-ray spectroscopy (EDX) among others, the layers' composition can be determined. This supplies information on the corrosion mechanism. Recently developed measuring techniques (surface profilometry, for instance) are used in the work of Linjewile [41]. The advantages of metallographic analysis are the accuracy and large amount of information that can be obtained from the examination of the layers. The main disadvantages are twofold: firstly it is a destructive method and secondly it cannot be implemented online. The analysis takes place after the probe cools down and this may influence the observed layers.

b) Weight loss measurements: The change in weight of a component or sample during the corrosion process is a primary measure of the corrosion rate. The weight change of a corroding sample can correlate with reaction time in various ways, as already shown in Figure 2.7. In order to determine the metal loss of the sample corrosion products must be removed before weighing. More sophisticated laboratory techniques such as thermal gravimetric analysis (TGA), where the weight loss of the coupon is monitored online, cannot be properly applied under the unfavourable power plant conditions. These days corrosion coupons are commercially available (e.g. KEMCOP© provided by the KEMA company [42]). Corrosion coupons are small specimens of the materials of interest. They are inserted into the process stream near the walls so that they do not need additional cooling. Although the accuracy is low, it is a cheap and robust system that does not need much maintenance. Furthermore, coupons can later be analysed in a laboratory (e.g. SEM or EDX), yielding information on the corrosion mechanism involved [43].

c) Online electrical resistance measurements: With electrical resistance (ER) sensors the electrical resistance of a conductor is measured. The resistance is inversely proportional to its cross-sectional area. If the conductor corrodes, its cross-section (and thus its electrical resistance) changes and so the average rate of corrosion can be determined. Commercially available ER sensors consist of a wire of the material of interest that is exposed to the corrosive atmosphere (an example is the CEION® technology provided by the Cormon Company [44]). The electrical resistance of the wire can be measured continuously so that the corrosion rate can be monitored online. If the wire corrodes, its electrical resistance increases. The main drawback of this monitoring technique is the temperature dependence of the resistance. Although electrical resistance sensors are commercially available, the author has not found any report about their application in power plants.

   d) Pyrometry (online): according to KEMA pyrometric techniques can be used to measure changes in the heat conduction properties of a metal foil due to corrosion. Although the KEMA company has a patent pending for a sensor based on this principle, neither a more detailed description of the measuring principle nor further results of pyrometric measurements in this context are known to the author [45].

2) Electrochemical methods measure changes in voltage (or current) due to the exchange of charges during the corrosion process. All electrochemical measuring systems use similar equipment. The sensor head typically consists of three electrodes (working, counter and reference electrode). Two geometric arrangements of the electrodes on the sensor's head are used: linear with three separated electrodes or cylindrical with electrode rings electrically isolated. The electrochemical systems are classified according to the measuring techniques used:

   a) Electrochemical noise (EN) (online): Electrochemical processes taking place on the electrode's surface cause small fluctuations of the electric potential of the electrode. On a corroding electrode the order of magnitude of these fluctuations is about 1mV. EN techniques are able to measure such small potential fluctuations. The EN signals are then analysed statistically (including simple standard deviations as well as more complex transforms to the frequency domain). The behaviour of the EN signals gives information on the types of corrosion damage (pitting, selective corrosion, etc.). This technique has proved to be very useful for the detection of pitting corrosion. On the other hand, this method presents a challenge as it is sensitive to external noise and signal deterioration. Different research groups [41, 46] have developed their prototypes of EN sensors and carried out tests in several power plants. However, no commercially available EN sensors are known to the author.

b) Linear polarisation resistance (LPR) (online): For the measurement of the polarisation resistance an external DC voltage is applied between working and counter electrode and the resultant current is measured. Since the electrodes are electrically isolated, any electric current from one to the other requires an ion-conducting layer ("electrolyte") between them. Taking into account the system’s free corrosion potential, the approximately relationship between applied voltage and current yields a resistance value that can be converted to an average metal loss rate [47, 48]. A more detailed description of this technique will be given in the following sections. The company Corrmoran GmbH [49] offers an LPR corrosion probe that has proved suitable for long-term operation in numerous EfW plants.

c) Electrochemical impedance spectroscopy (EIS) (online): This technique uses an imposed AC signal over a stepped frequency range to generate a response. This response is analysed to infer the resistance and capacitance at each frequency. The principle is similar to the LPR technique. The use of AC voltage instead of DC yields not only the polarisation resistance but also the capacitive and inductive component of the impedance and thus more information on the electrochemical process involved. The University of Essen-Duisburg has developed an EIS corrosion probe that has been tested in the laboratory [50].

Table 2.1 summarises the described methods. Online methods are those which can measure corrosion during exposure of the probe to the corrosive environment. Their main advantage is that they supply information on the corrosion progress in real time. This has two main benefits:

1. It allows the plant operator to react on time to changes in the corrosivity of the gas or deposits. In particular, this is necessary when firing or co-firing very heterogeneous fuels (like biomass) or when the plant is operated at high live steam parameters (high temperature or high pressure). Therefore online monitoring techniques may become a very useful tool for more flexible plant operation in the coming years.
2. It allows studying the progress of corrosion with time under real conditions offering a range of new possibilities for corrosion research.

Table 2.1: Corrosion monitoring methods

Type	Name	Status	online
Metal loss	Metallography	Commercially available	
	Weight loss measurements	Commercially available	
	Electrical resistance	Commercially available*	✓
	Pyrometry	Tested in the laboratory	✓
Electrochemical	Electrochemical noise (EN)	Prototype	✓
	Linear Poliarsation Resistance (LPR)	Commercially available	✓
	Electrochemical Impedance Spectroscopy (EIS))	Tested in the laboratory	✓

*only for low-temperature applications

In the literature the term "*in-situ*" is used for corrosion monitoring methods whose sensors are able to stand the high-temperature conditions in a power plant. A corrosion probe with rings of different materials that is exposed to the flue gas for a certain time and analysed later on in the laboratory is an example of a sensor that is used *in situ*, but does not supply information online. An electrochemical corrosion sensor measuring corrosion signals while exposed to the corrosive gases is an example of an online sensor that is used *in situ*.

Finally the author would like to introduce the term "second generation" for those online corrosion monitoring methods that can measure corrosion rates on real components of a power plant. Current online corrosion methods use a corrosion probe, which differs from the real heat exchangers of a power plant. To evaluate measurements it must be confirmed that conditions around the probe are similar to conditions around the plant components whose corrosion is being simulated. Only in this case the corrosion signal will be representative of real corrosion rates. The term second generation stands for a further development of existing corrosion monitoring methods or the development of new ones with the aim of measuring actual corrosion rates directly on the plant components.

2.2 Agglomeration

One of the main technologies for biomass combustion is the fluidised bed technology. The turbulent mixing of fuel and bed material (typically sand) in a fluidised bed allows the combustion of heterogeneous fuels like biomass that are difficult to burn with other technologies.

In the field of fluidised bed combustion and gasification agglomeration is defined as the cohesion of bed particles or fuel ashes forming big clumps and disturbing fluidisation. If agglomerates are big and adhesive enough, defluidisation can occur. Agglomeration thus decreases plant efficiency and can even force a shutdown of the plant causing high costs for the plant operator.

Agglomeration may be the result of the formation of low-melting eutectic mixtures of bed particles and ashes in the bed. Si, K and Ca play the most important role. According to Olofsson *et al.* and Lin *et al.* [51, 52], the agglomeration tendency may increase with the K content and decrease with the Ca content in the fuel. Potassium forms low-melting eutectics with Si which have melting temperatures far below 800 °C. On the other hand Ca increases the melting temperature of the mixture, thus decreasing the agglomeration risk. The agglomeration tendency is often illustrated in SiO_2-K_2O-CaO or Si-Ca-K ternary diagrams [53-57]. Figure 2.8 shows the liquidus projection of this diagram.

Straw agglomerates are characterized by a high SiO_2 (80-100%) and a relatively high K_2O content (5-30%) together with a low CaO content. They are located in a low-melting zone where the melting temperature is approximately 720 °C. Other alkalis and alkaline earth metals like Na or Mg can further shift the melting point of the eutectic compounds formed [51].

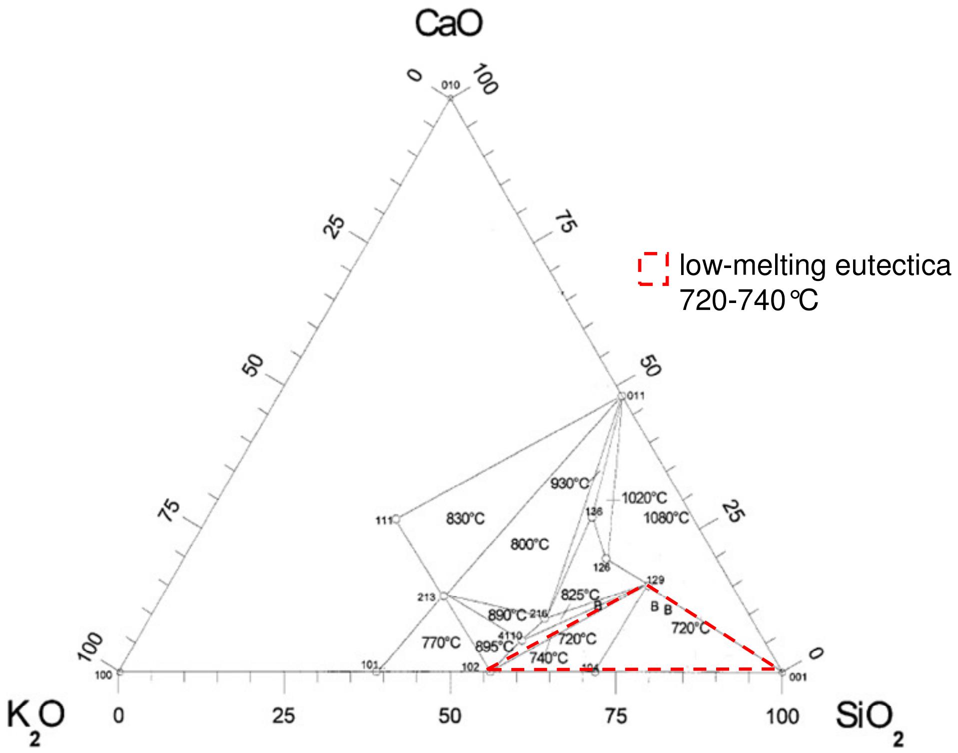

Figure 2.8: SiO_2-K_2O-CaO ternary diagram liquidus projection (adapted from [57])

2.2.1 Agglomeration mechanisms

In the literature different agglomeration mechanisms are described [48, 49, 51-58]. They can be divided into two main categories (see Figure 2.9):

1. Coating-induced agglomeration: this kind of agglomeration is due to the sintering of layers formed on the particles' surface. The agglomerated particles are covered by a layer of some micrometres thickness that forms bridges between them and glues them together. Agglomeration occurs when the coating formed on the particles reaches a critical thickness, different values of which are reported in the literature [58]. This layer consists mainly of K, Ca and Si, the ratios depending on the fuel used. Alkali metals present in biomass are mainly organically bound and highly volatile. Potassium vapours may react with the quartz sand particles forming a coating of low-melting eutectic on them [59]. For straw combustion a mixture of SiO_2 and K_2O (~80/20%) is reported in [52]. Different theories are proposed in the

literature regarding the formation of this coating. Olofsson *et al.* [51] attribute the coating to the formation of hot spots in the bed. Local high temperatures can melt alkali silicates that are adhesive and cover bed particles with a thin layer of the molten phase. When temperature decreases, silicates solidify and bed particles glue together. On the other hand Brus *et al.* [58] studied the growth of the coating during the combustion of olive residues and concluded that the layer grows inward towards the particle, so a chemical interaction between the bed particle and the surrounding ashes must be responsible for its formation. Other authors suggest that the formation of this layer is only related to physical processes.

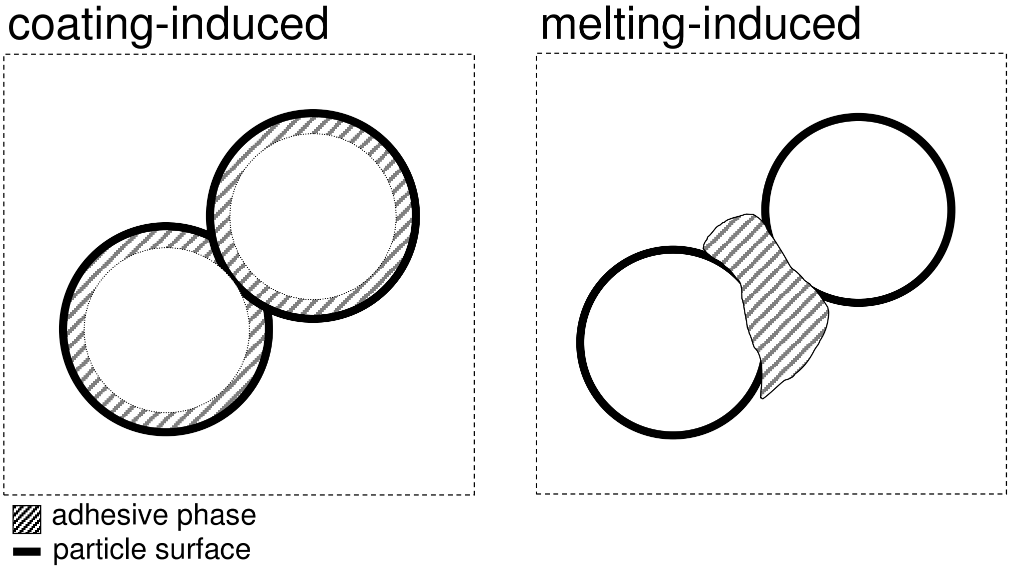

Figure 2.9: Agglomeration mechanisms (adapted from Visser et al. [60])

2. Melting-induced agglomeration: In this case no coating can be observed on the bed particles which are glued together by molten ash fragments. This mechanism depends mainly on the fuel ash composition, especially on the K, Ca and Si content in the fuel.

Due to its high alkali and chlorine content, straw is one of the most problematic biomasses. During its combustion in fluidised bed reactors the agglomeration of bed particles leads to the defluidisation of the bed and the shutdown of the plant at a high cost for the plant operator. The high price of “traditional” and less problematic biomasses (such as wood) alongside new European policies increases however the interest of plant operators in straw as an alternative fuel.

In the present work the agglomeration behaviour of rye straw, wheat straw and wood during small-scale tests in a fluidised bed reactor is compared. In the case of straw ashes both mechanisms are reported in the literature [47, 48, 54]. Straw agglomeration in fluidised bed combustors has been studied by various research groups from an experimental point of view. In the following an overview is given.

2.2.1.1 Alkali release during combustion

According to thermodynamic calculations in Baxter *et al.*, Lin *et al.* and Michelsen *et al.* [48, 59, 60] K is first released in form of KCl. KCl(g) release starts at temperatures between 700 and 800 °C. At temperatures above 800 °C other compounds like $(KCl)_2$(g), KOH(g), K(g) and K_2SO_4(g) can also be formed. According to Jensen *et al.* [30] approximately 25% of the potassium volatilizes during straw pyrolysis at temperatures above 700 °C: in form of chlorides at temperatures between 700 °C and 830 °C, in form of potassium hydroxides at temperatures between 830 and 1050 °C. Arvelakis *et al.* [61] studied the volatilization of potassium by means of simultaneous thermal analysis (STA) of straw ashes and synthetic mixtures of SiO_2 with potassium and calcium silicates and carbonates. They observed that between 850 °C and 1150 °C potassium is released in form of chlorides and above 1150 °C in form of K_2O but most of the potassium still remains in the ashes. They associated high alkali release with a high chlorine and a low silicon content in the fuel. Skrifvars *et al.* [62] reported that under FBC conditions no potassium compounds are released in the gaseous phase and all the potassium remains in the ash matrix.

2.2.1.2 Ash melting behaviour

Skrifvars *et al.* [62] studied the sintering behaviour of wheat straw ashes. Straw ashes start to melt at about 625 °C. Between 625 °C and 765 °C the molten phase consists only of alkali salts. Above 765 °C silicates melt. At a temperature of 800 °C around 30 to 50 wt.% of the wheat straw ashes may melt. Arvelakis *et al.* [61] reported initial melting points for straw ashes with high chlorine content between 600 and 700 °C.

The work of Hansen *et al.* [63] and Skrifvars *et al.* [62] notes that the temperature at which an initial deformation is observed may be far below the melting point of the ash.

2.2.1.3 Defluidisaton temperature

Visser *et al.* [60] studied the defluidisation temperature for straw-derived bed material (after being used in a straw gasifier). The temperature of the bed was increased without adding more fuel by means of electric heating. The temperature was increased until defluidisation for different fluidisation velocities. The defluidisation temperature is about 700 °C for low fluidisation velocities ($U_f \sim U_{mf}$; U_{mf} = minimum fluidisation velocity). With rising velocities ($U_f \sim 4U_{mf}$) defluidisation temperature increases asymptotically to about 850 °C.

2.2.1.4 Influence of combustion parameters

Combustion temperature: The temperature has a strong influence on agglomeration. All studies performed so far confirm that the agglomeration risk increases with temperature [45, 46, 54]. Lin *et al.* [52] studied the defluidisation time as function of the bed temperature in a FBC. They found a nearly exponential decrease of defluidisation time with temperature. Above 700 °C the defluidisation time halved with every 50 °C temperature increase in the bed.

Bed material: Several research papers compare the behaviour of different bed materials during straw combustion. De Geyter *et al.* [64] and Olofsson *et al.* [51] carried out combustion tests comparing different fuels and bed materials. They observed agglomeration in all the tests using straw as fuel. Interestingly, the best results were obtained with Fe and Al rich bed materials.

Size of bed particles: Lin *et al.* [52] measured the influence of bed particle size on the defluidisation time: the bigger the particles, the higher the agglomeration tendency.

Other parameters: No influence of fuel size, stoichiometry or reactor pressure on agglomeration behaviour could be detected in the work of Lin *et al* [52] and Olofsson *et al.* [51].

3 Small-scale set-up

This chapter describes the experimental set-up for the small-scale tests considered here. This work has been carried out within the framework of different research projects. The main parameters and operating conditions of the tests have thus been conditioned by the aims and requirements of every project. The small-scale tests consisted in combustion runs of between 8 and 30 hours of duration in a fluidised bed reactor designed and constructed at the Institute for Energy Systems (Technical University of Munich). In the following the experimental setup is described.

3.1 Description of the fluidised bed reactor

A fluidised bed consists of a packed bed of fuel particles above a grid through which air can be passed upwards the bed [14]. At enough air velocity the bed fluidises resulting in a turbulent mixing of the bed particles, the fuel and the fluidisation air. The turbulent mixing accounts for very homogeneous temperatures and high heat flow rates in the fluidised bed [65] which makes this technology particularly attractive for the combustion of heterogeneous fuels and/or fuels with low heating values.

The fluidised bed reactor used for the tests is shown in Figure 3.3. It is a bubbling fluidised bed reactor of about 30 $kW_{th.}$ The reactor is made of high-temperature steel and it has an inner diameter of 190 mm and 550 mm height. The furnace above the bed, called freeboard, has a diameter of 310 mm and is 450 mm height. The function of the freeboard is to decrease the flue gas velocity avoiding the bed particles to be carried out of the bed. At the bottom of the bed there is a perforated plate (91 holes with $d = 1.8$ mm) used for the distribution of the fluidisation air. An even distribution of the fluidisation air is necessary in order to guarantee a uniform fluidisation of the bed.

The fuel is fed into the reactor by means of a screw feeder. Screw feeders have delivered a good performance as a conveying system for biomass pellets in a great number of applications. The feeding rate can be controlled by varying the frequency of the motor powering the feeding screw.

During start-up the reactor must be heated up electrically. Resistors around the reactor are able to heat up the bed to 570 °C. Additionally the combustion air can be preheated to 600 °C by an electric heater and an additional electric resistance (2.7 kW). Once the bed temperature reaches the autoignition temperature of the fuel (~350 °C) fuel is fed and combustion starts.

The gas velocity in the reactor is about 0.5 m/s, slightly lower than typical velocities in industrial bubbling fluidised bed furnaces (1-2 m/s [14]). The pressure drop in the bed is about 40 mbar during fluidisation.

Before being released into the atmosphere the ash particles are removed from the flue gas. Coarse particulate matter is separated from the flue gas in a cyclone and fine particles are filtered downstream the cyclone. More details about the reactor can be found in the work of Ottmann [66].

In the following a short overview of the measuring instruments and data collection in the facility is given:

- Bed temperature: At various heights along the fluidised bed (80, 90, 100 and 120 mm above the perforated plate) there are ports for thermocouples (type K) for the measurement of the bed temperature.
- Pressure: The air pressure is measured upstream of the bed. A differential pressure transmitter is used to measure the pressure drop in the bed. A low pressure transmitter measures the pressure in the freeboard and the exhaust gas pipe.
- Volumetric flow: The volumetric flow rate of the air is measured by means of a thermal flow sensor and a variable-area flow meter measures the secondary air flow.
- Data acquisition: The sensor's signals are transmitted to the PC by two A/D-convertors with USB connection to the computer. The programme LabVIEW^{TM} 8.5 of the National Instruments company is used for the digital data processing.

- Gas composition: The flue gas is sampled from the freeboard and led into the Fourier transform infrared (FTIR) spectrometer for the online measurement of HCl and SO_2. The measuring set-up is explained in section 3.3. Downstream of the cyclone, flue gas composition (O_2, CO_2 and CO) is measured with a standard portable gas analysis device.

The position of all these measuring points is included in Figure 3.3.

3.1.1 Fluidisation and combustion parameters

In order to achieve a complete combustion of the fuel in the bed an adequate fluidisation must be guaranteed. The fluidisation of the bed depends on the fluidisation air flow, its distribution, the material and size of the bed particles, etc. All these fluidisation parameters must be properly combined in order to obtain a stable and uniform fluidisation of the bed. The physical fundamentals for the calculation of the main fluidisation factors can be found (among others) in the work of Hofbauer and Basu [65, 67]. Table 3.1 includes the input values used for the calculations and for the fluidisation tests. Figure 3.1 compares the calculated and measured pressure drop in the bed as function of the bed temperature.

Prior to fluidisation, the pressure drop increases with temperature. At this stage the bed particles remain in one aggreagate state. Once a certain temperature is reached the aerodynamic drag forces counteract with gravitational pull and the bed fluidises. The measured fluidisation temperature (the temperature of the bed at which fluidisation starts) is around 320 °C. Once fluidised, the pressure drop of the bed keeps a constant value of about 40 mbar.

For the combustion experiments 8 ℓ of quartz sand (0.7-1.2 mm grain diameter) are introduced in the reactor. As already mentioned the bed is electrically preheated to a temperature of about 570 °C by means of an electric heating jacket. For this preheating phase the fluidisation air is heated to about 450 °C by means of an electric heater and an additional electric resistance. The primary air flows at about 15 Nm^3/h. The development of the bed temperature over time can be seen in Figure 3.2.

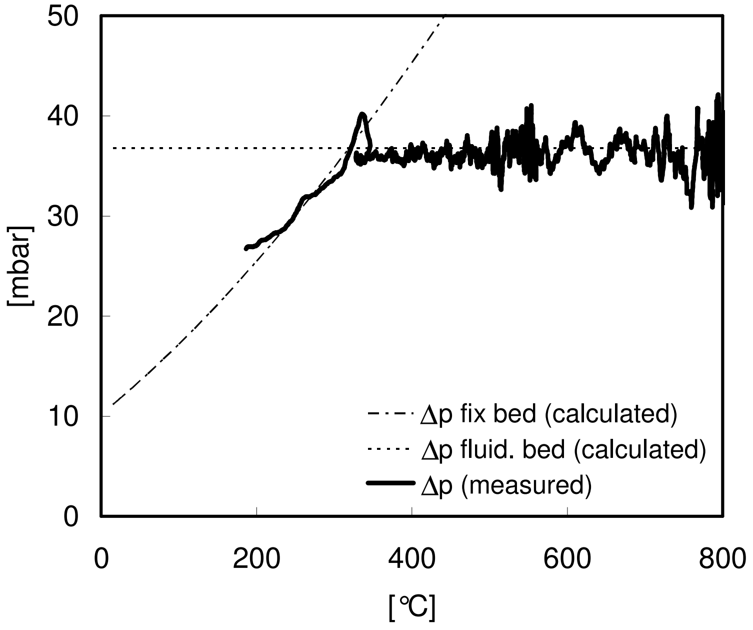

Figure 3.1: Calculated and measured pressure drop in the bed

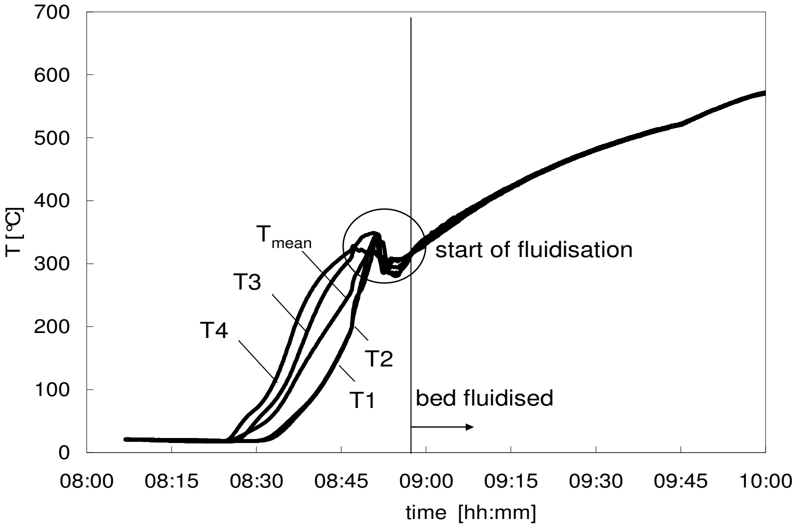

Figure 3.2: Bed temperatures during the initial heating of the facility (the positioning of the thermocouples in the bed is shown in Figure 3.3)

The lower thermocouples in contact with the hot fluidisation air indicate higher temperatures. Before fluidisation the pressure drop in the bed increases with the temperature, too. Between 300 °C and 320 °C the fluidisation of the bed starts. This can be detected by the convergence of the different bed temperatures measured. During fluidisation the hot zones at the bottom of the bed mix with the cold zones at the top of the bed so that the four measured temperatures converge to the same value. Once the bed is fluidised the pressure drop in the bed does not increase with the temperature. The convergence of the bed temperatures and the constant value of the pressure drop serve as indicators of a complete fluidisation of the bed. When the bed temperature reaches 570 °C fuel feeding starts and combustion begins. At this temperature the combustion of the pellets that fall in the bed is guaranteed. The primary air flow is then reduced to about 10 Nm^3/h. An additional secondary air flow of 5 Nm^3/h is introduced in the reactor with the fuel to avoid smoke escaping through the feeding system. The feeding screw frequency is adjusted to obtain a fuel feed rate of about 3 kg/h. The electric heating of the bed is switched off. The bed temperature is adjusted by the electric preheating of the fluidisation air.

Table 3.1: Fluidisation parameters

Reactor geometry			
diameter	D	0.19	m
volume of bed material	V	7	ℓ
height of fixed bed	H	0.25	m
height of fluidised bed	H_L	0.28	m
volumetric flow rate at a point	V_{flow}	14	Nm^3/h
pressure of the gas	p	0.95	bar
bed material		quartz sand	
particle sizes		0.7-1.2	mm
diameter of bed particle	d_p	$9.5 \cdot 10^{-4}$	m
surface-volume diameter	d_{sv}	$8.3 \cdot 10^{-4}$	m
particle form factor	ψ	0.86	-
volume mean diameter	d_v	$9.6 \cdot 10^{-4}$	m
particle density	ρ_p	2680	kg/m^3
porosity	ε	0.39	-
fluidisation porosity	ε_L	0.5	-
bulk density	ρ_b	1500	kg/m^3

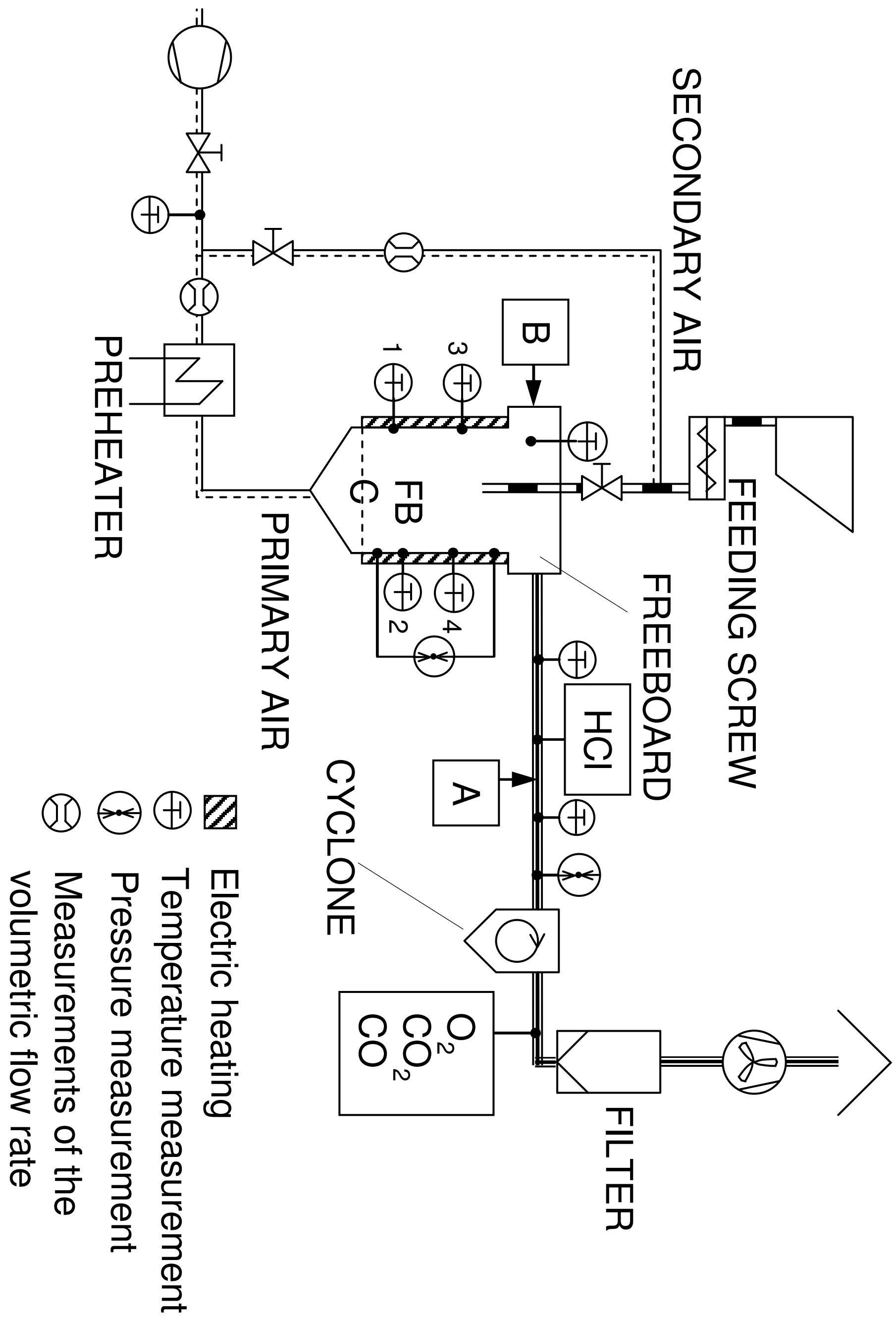

Figure 3.3: Fluidised bed reactor

3.2 Fuels

Biomass is defined within the framework of this research work as organic matter from plants or animals used to produce energy [68]. There is a wide range of materials and substances that can be included in this definition. Accordingly, a wide range of technologies have been developed to generate energy from them. Their combustion is the most important and most established technology. Biomass that can be used as fuel in combustion systems can be divided into four main categories: wood from forestry, agricultural residues, energy crops and the biodegradable fraction of household or industrial waste. In this work tests were carried out with fuels from all these categories. In the following the fuels used are described.

Spruce wood pellets: Wood is a traditional fuel. Wood pellets (WP) are usually made of compressed sawdust, a by-product of forestry and the wood industry. Nowadays the composition and main characteristics of wood pellets are regulated by national standards. For the tests considered here wood pellets according to DIN 51731 were used. This means pellets of 4 to 10 mm of diameter and up to 50 mm length. Their calorific values vary between 17.5 and 19.5 MJ/kg, the water content is lower than 12 wt.% and the ash content lower than 1.5 wt.%.

The composition of the wood pellets is included in Table 3.2 and Table 3.3. Compared to other biomasses, wood has a low alkali and chlorine content so that the corrosion and agglomeration risk during its combustion is low.

Rye and wheat straw pellets: In Germany the energy that could be extracted annually from straw is estimated at about 130 PJ [69]. This is approximately 1% of Germany’s primary energy demand in 2009 [70].

Like every natural fuel, straw is very heterogeneous: plant species differ widely in composition (in particular water and ash content), depending also on associated crops and soils [71]. Charges of winter rye and wheat straw pellets (RSP and WSP respectively) were supplied by the Thüringer Zentrum nachwachsender Rohstoffe (Thuringian Centre for Renewable Resources) of the Thüringer Landesanstalt für Landwirtschaft Dornburg (Thuringian State Institute of Agriculture in Dornburg)[72]. These charges were especially prepared for research purposes. The cultivation and fertilisation of the straw was controlled throughout the lifetime of the plant as was the pelleting process. The pellets produced from these charges were assumed to have a more homogeneous composition than commercially available straw pellets.

Table 3.2 and Table 3.3 show their composition. Both types of straw show a much higher alkali (Na, Ca and K) and chlorine content than wood. The proportion of Ca is similar in both straws, while Na, K and Cl values are much higher for rye straw pellets. As reported in [73], high K values are usually associated with high Cl values. Straw pellets also have a higher Si and Al content than wood.

Cl- and S-doped wood pellets: Figure 3.4 shows the Cl and S content of a wide variety of biomasses [74]. Energy crops are characterised by a high sulphur content. The sulphation of chlorides generates chlorine-rich gas near the tube walls. The sulphur content of a fuel is therefore also a relevant parameter in order to predict its corrosion behaviour. Some sources propose the use of the molar S/Cl ratio as a corrosivity indicator [75]: the lower this value, the higher the corrosion tendency. The molar S/Cl ratio in natural fuels can vary between approximately 0.01 and 10. The use of this ratio as a corrosivity indicator only makes sense with chlorine-rich fuels as it could also be very low for fuels with a low chlorine and sulphur content which have a low corrosion potential.

Natural fuels with different S and Cl content also show significant variations in the concentration of other relevant components like alkalis, ash and water. It is therefore difficult to draw scientific conclusions from the comparison of their corrosion behaviour. One possibility to overcome this difficulty is to use controlled crops whose cultivation has been monitored. This option was chosen for the straw pellets described above. An alternative is to dope standard wood pellets. For the study of the influence of S and Cl on the corrosion behaviour of the fuels this option was favoured.

As an additive for Cl doping ammonium chloride (NH_4Cl) was used. Metal chlorides like NaCl and $CaCl_2$ could affect the corrosion mechanisms. Ammonium chloride dissociates during combustion into NH_3 and HCl and NH_3 is supposed to leave the reactor with the flue gas without influencing the corrosion reactions [66]. The additive used for the S doping was methionine, a sulphur containing amino acid (CH3-S-CH2-CH2-CH(NH_2)-COOH). The weakly bound sulphur in the organic methionine molecules is quickly released during the combustion. Charges of spruce sawdust (base material for the wood pellets) was mixed with different doping solutions, then dried and pelletised. The S and Cl content of the resulting doped wood pellets is included in Table 3.2 and Table 3.3. One charge with low S/Cl ratio (WP+S/Cl 0.02), one charge with medium S/Cl ratio (WP+S/Cl 0.8) and one charge with high S/Cl ratio (WP+S/Cl 1.5) were prepared. Figure 3.4 compares their S and Cl content with that of other biomasses.

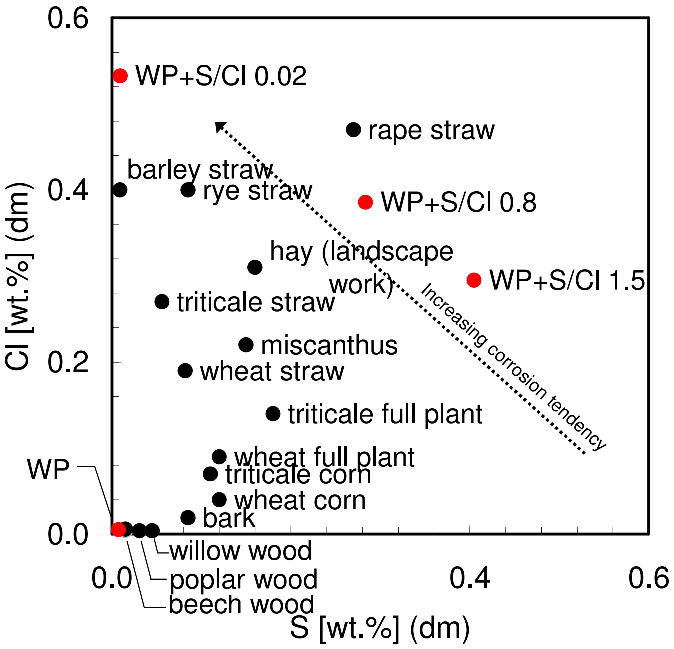

Figure 3.4: S and Cl content for different biomasses dm = dry matter; red point = fuel used in this work (adapted from [74])

$ZnCl_2$-doped wood pellets: Especially in Northern Europe recovered wood waste (RWW) has increased in importance as a regenerative fuel in the last years. This contributes to increasing the share of regenerative fuels in the total energy production as well as reducing the amount of waste for landfill. RWW includes all kinds of wooden material that becomes available when a wooden product reaches the end of its use. These materials can be divided into four categories: untreated wood, surface-treated wood, industrial preservative-treated wood and different types of building boards such as plywood and chipwood [76]. In the case of waste and demolition wood not only alkali and chlorine but also other chemical species can be involved in the high-temperature corrosion processes. Especially Zn and Pb chlorides seem to play an important role. Zinc and lead are found in their highest concentration in surface-treated wood present in RWW and originate mainly from white pigments [76].

Spruce wood pellets were doped with a $ZnCl_2$ solution. The fuel preparation was carried out by the Process Chemistry Centre of the Åbo Akademi University and described in detail in [77]. Two different concentrations were used. The solid zinc chloride was dissolved in deionized water and sprayed carefully onto the fuel using a common sprinkler. After doping, the pellets were dried and then packed and stored in sealed barrels. Table 3.3 shows the Zn and Cl content of each charge (WP0.1% and WP0.5%). The Zn content in the different pellets corresponds to mean and high Zn content in demolition wood [78].

Table 3.2: Fuel composition, part 1 (C, N, H, O, H2O and Ash)

FUEL	C [wt.%] (dm)	N [wt.%] (dm)	H [wt.%] (dm)	O [wt.%] (dm)	H_2O [wt.%] (dm)	Ash [wt.%] (dm)
WSP	46.5	0.6	5.8	41.8	10.0	5.2
RSP	44.9	1.1	5.8	41.1	6.3	6.7
WP	49.7	0.2	5.7	44.4	6.5	0.3
WP0.1%	49.7	0.2	5.7	44.4	8.3	0.3
WP0.5%	49.7	0.2	5.7	44.4	9.0	0.3
WP+S/Cl 1.5	50.0	0.5	5.7	43.4	6.3	0.3
WP+S/Cl 0.8	50.2	0.5	5.7	43.3	6.5	0.3
WP+S/Cl 0.02	50.0	0.4	5.7	43.9	5.6	0.3

WP: wood pellets; RSP: rye straw pellets; WSP: wheat straw pellets; WPxx%: $ZnCl_2$-doped wood pellets; WP+S/Cl xx: Cl- and S-doped wood pellets

Testing of solid fuels in accordance with DIN 51701, 51718, 51719

Table 3.3: Fuel composition, part 2

FUEL	S [wt.%] (dm)	Cl [wt.%] (dm)	K [wt.%] (dm)	Ca [wt.%] (dm)	Si [wt.%] (dm)	Na [mg/kg] (dm)	Zn [mg/kg] (dm)	Al [mg/kg] (dm)	S/Cl molar
WSP	0.08	0.04	0.55	0.34	1.51	156	9	378	2.21
RSP	0.10	0.26	1.21	0.41	1.46	261	14	1430	0.43
WP	0.01	0.01	0.01	0.07	0.01	10	19	10	1.51
WP0.1%	0.01	0.05	0.01	0.07	0.01	10	883	10	0.16
WP0.5%	0.01	0.15	0.01	0.07	0.01	10	2385	10	0.05
WP+S/Cl 1.5	0.40	0.30	0.01	0.07	0.01	10	19	10	1.52
WP+S/Cl 0.8	0.28	0.39	0.01	0.07	0.01	10	19	10	0.81
WP+S/Cl 0.02	0.01	0.53	0.01	0.07	0.01	10	19	10	0.02

WP: wood pellets; RSP: rye straw pellets; WSP: wheat straw pellets; WPxx%: $ZnCl_2$-doped wood pellets; WP+S/Cl xx: Cl- and S-doped wood pellets

Testing of solid fuels in accordance with DIN 51727, 51732, 22022

K and Na contents determined by Atomic Absorption Spectroscopy

3.3 Flue gas analysis

The flue gas composition in the fluidised bed reactor was determined by means of thermodynamic equilibrium calculations (using Fact Sage software) and measured online during the experiments. O_2 and CO were measured with a standard gas analysis device. For the measurement of HCl wet chemical analysis (according to DIN EN 1911 [79]) and an FTIR spectrometer were used.

For the HCl measurements with the FTIR spectrometer a small amount of flue gas (~0.2 Nm^3/h) was extracted at position A in Figure 3.3. To this end an electrically heated sampling Inconel® tube was used. The function of this tube was to cool down the sampled gas to the maximal operating temperature of the gas processing components (filters, FTIR measuring cell, etc.) downstream of the sampling point. These components have a maximum operating temperature of about 200 °C. Downstream of the Inconel® tube the gas was channelled through the sample gas probe. This sample gas probe was equipped with a sintered stainless steel filter (pore size 0.5 µm) in order to remove solid particles from the gas. Stainless steel has proved to be more suitable for this application than other materials. The main advantage compared to ceramic filters is that the stainless steel ones are less fragile and can be cleaned in an ultrasonic bath. Downstream of the sample gas probe a second filter was employed to protect the spectrometer in case of a failure of the first filter. All the components from the sample gas probe to the spectrometer measuring cell were electrically heated to 180 °C in order to avoid condensation. Downstream of the spectrometer a condensation trap collected the condensed compounds. The gas flow was regulated by a membrane pump located at the end of the gas path. Figure 3.5 shows the measuring set-up. In addition to the described sample path there is a nitrogen path. The nitrogen has two functions: (1) to purge the path of the optical beam inside the spectrometer; (2) to purge the measuring cell for obtaining background spectra.

Finally in zone A of Figure 3.5 the set-up for the wet chemical measurements according to the DIN EN 1911 standard can be seen.

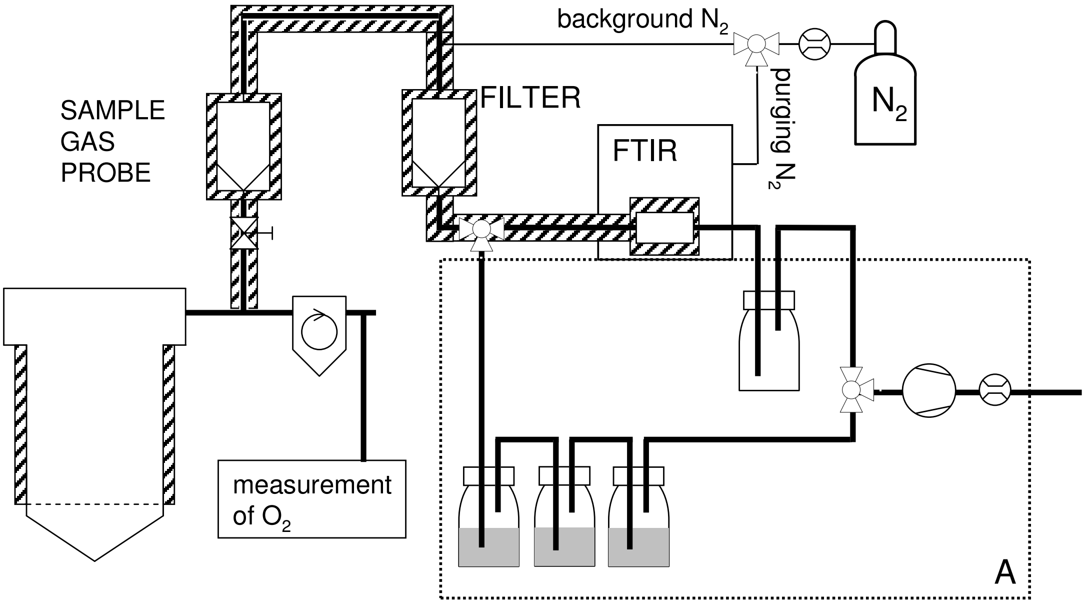

Figure 3.5: FTIR set-up for the HCl measurements

3.4 Experimental programme

In this work small-scale short-term tests with two of the corrosion measuring techniques described in 2.1.3 were carried out: two techniques from the metal loss category (the metallographic analysis of a corrosion probe and an alternative metal loss technique based on the measurement of iron losses in order to shorten the duration of the tests) and one technique from the electrochemical category (the measurement of linear polarisation resistance (LPR)). The duration of the tests varied between 8 and 30 hours. Different tube and flue gas temperatures were tested. Finally metallographic and LPR measurements were also carried out in a power plant. Table 3.4 gives an overview of the corrosion tests performed. The detailed test conditions are given in each chapter.

Table 3.4: Overview of corrosion tests

Technique	Fuel	$T_{\text{flue gas}}$ [°C]	T_{tube} [°C]	Sample material	Exposure time [h]	Chapter
Small-scale tests						
Metallography	doped wood pellets and wood pellets	750	450-550	Steel	8 and 28	4
Iron loss	doped wood pellets and wood pellets	750	400-600	Iron	1 and 3	5
LPR	doped wood pellets and wood pellets	750	430	Steel	8 and 28	6
Power plant tests						
Metallography	waste	850 and 650	380	Steel	500 and 1200	8
LPR	waste	850 and 650	380	Steel	500 and 1200	8

The agglomeration tests are summarised in Table 3.5. Combustion runs of around 8 hours were carried out with three different fuels for the same fluidised bed temperature. The agglomeration behaviour was studied on the basis of bed sample analysis in the laboratory. The detailed conditions of these tests are given in Chapter 7.

Table 3.5: Overview of agglomeration tests

fuel	Duration of the test [h]	Tbed
RSP	~8	800 °C
WSP	~8	800 °C
WP	~8 x 3	800 °C

4 Metallographic tests

The metallographic analysis of the corroded material is one of the standard methods to investigate corrosion mechanisms. The work reported in the literature can be divided into three categories: (1) analysis of original superheater tubes that have been removed from the boiler (exposure time > 8000 h), (2) analysis of corrosion probes exposed to the flue gases of a power plant (exposure time ~ 1000 h) and (3) analysis of probes exposed to a controlled atmosphere in a laboratory furnace (exposure time ~100 to 1000 h). In each case the tubes or probes are cut transversely and their cross section is investigated under a microscope. The analysis of the structure and composition of the scale formed on the sample supplies information on the chemical species involved in the corrosion mechanism.

During this series of measurements metallographic analysis of probes with short exposure times was carried out. These experiments were carried out together with the Process Chemistry Centre of the Åbo Akademi University in Finland. Rings of different materials were exposed for 8 hours to the flue gases of the small-scale facility described in 3.1. They were then analysed using scanning electron microscopy (SEM), back-scattered electron (BSE) microscopy and electron-dispersive X-ray spectroscopy (EDX).

The exposure time of 8 h is much shorter than that of the probes used in the literature mentioned above (~1000 h). The aim of the tests was to evaluate how much useful information could be obtained from metallographic analysis after such a short exposure time. The following questions were addressed:

- Is an exposure time of 8 hours long enough to properly observe the scale formed on the probe’s rings under the microscope? Are the results reproducible?
- Are the corrosion products on the probe’s rings similar to the ones obtained in real power plants?
- Can the metallographic analysis of the rings supply information on their corrosion rate?

These and other questions will be answered by the results of this series of measurements.

4.1 Corrosion probe

The corrosion probe used was developed by Åbo Akademi University [80] and is shown in Figure 4.1. It consists of a cylindrical head (diameter: 37 mm) with two distinct rings (width: 20 mm) that are exposed to the flue gases. These rings can easily be removed from the probe and analysed by means of SEM, BSE and EDX techniques. The probe is cooled to the temperature of interest with pressurised air (6 bar). One thermocouple is inserted in each ring; the first one is used to monitor the ring temperature, the second one for the proportional-integral-derivative (PID) controller of the cooling unit. The probe was introduced in the freeboard of the reactor at position B in Figure 3.3. The probe's rings were cleaned in ethanol using an ultrasound bath according to the VDI 3955 standard [81] before exposure.

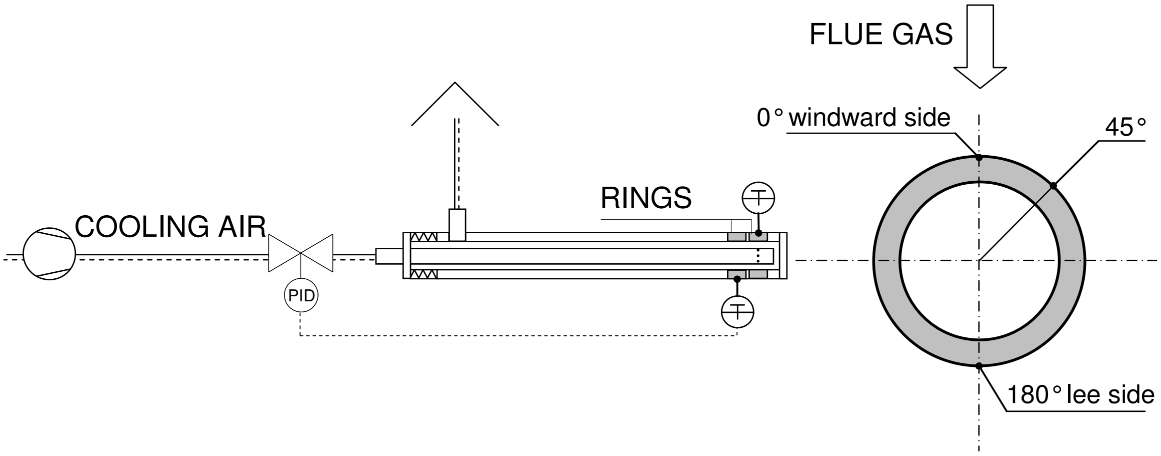

Figure 4.1: Corrosion probe for the metallographic analysis [80]

4.2 Test parameters

The fuels used for these tests were regular wood pellets (WP) and wood pellets doped with $ZnCl_2$ (WP0.1% and WP0.5%). The fuels were already described in section 3.2. The flue gas temperature at the probe's position is approximately 750 °C. Three different probe temperatures were tested: 450, 500 and 550 °C

Table 4.1: Steel composition of the corrosion probe's rings tested (16Mo3 is relevant for section 6) Source: [76]

Element [wt.%]	10CrMo9-10 material no. 1.7380	Sanicro 28 material no. 1.4563	16Mo3 material no. 1.5415
Fe	95-97	31-41	98-96
Cr	2-2.5	26-28	0.7-1.15
Mo	0.9-1.1	3-4	0.4-0.6
Mn	0-0.6	0-2.5	0.4-0.9
Si	0-0.5	0-1	0.35
Ni	-	29.5-32.5	-
C	0-0.15	0-0.03	0.08-0.18
P	0-0.03	0-0.03	0.025
S	0-0.03	0-0.03	0.01
N			0.012

Figure 4.2 shows the location of the corrosion probes in the Flingern corrosion diagram. For every test a different material was used for each ring: a standard low alloy steel 10CrMo9-10 for one and the austenitic steel Sanicro 28 (S28) for the other. The detailed steel composition is shown in Table 4.1. Table 4.2 shows the test matrix.

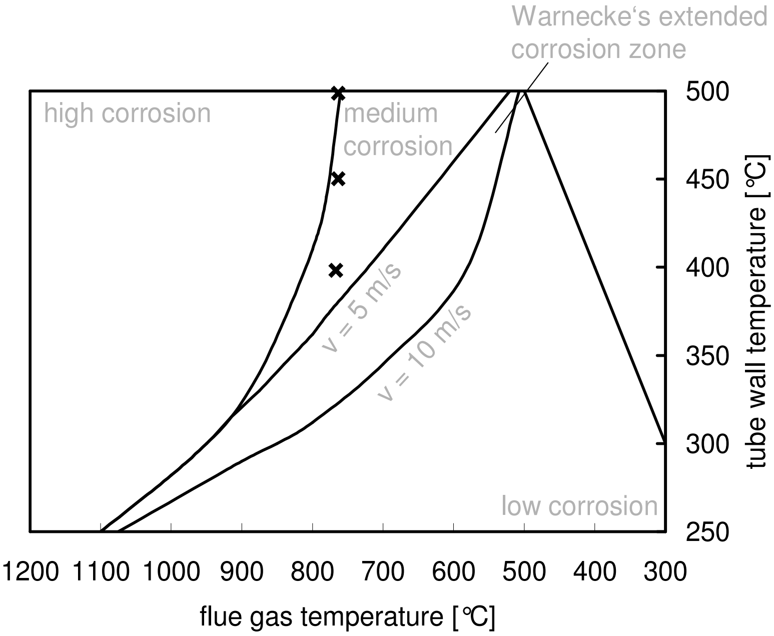

Figure 4.2: Position of metallographic probes in the Flingern corrosion diagram [16]

Table 4.2: Test matrix for the metallographic tests

Run #	Fuel	T_{probe} [°C]	Ring material	Exposure time [h]
1	WP0.5%	550	10CrMo9-10	8
1	WP0.5%	550	S28	8
2	WP0.5%	550	10CrMo9-10	8
2	WP0.5%	550	S28	8
3	WP0.5%	500	10CrMo9-10	8
3	WP0.5%	500	S28	8
4	WP0.5%	450	10CrMo9-10	8
4	WP0.5%	450	S28	8
5	WP0.1%	450	10CrMo9-10	28
5	WP0.1%	450	S28	28
6	WP	550	10CrMo9-10	8
6	WP	550	S28	8
7	WP	500	10CrMo9-10	8
7	WP	500	S28	8
8	WP	450	10CrMo9-10	8
8	WP	450	S28	8

4.3 Results

4.3.1 SEM, BSE and EDX analysis

SEM/BSE and EDX-mapping of each ring were taken at the three different positions (0°, 45° and 180°) as shown in Figure 4.1. The analyses were carried out by the Process Chemistry Centre of the Åbo Akademi University. A detailed description of the methodology can be found in [77]. The metal surface (in white) is located at the bottom of the micrograph. The different grey layers are the scale formed on the ring. The remaining black region is the epoxy matrix in which the rings were embedded for the microscope analysis.

10CrMo9-10 Rings

In all the experiments the SEM/BSE and EDX images of all three positions on the 10CrMo9-10 rings show three main areas:

1) The outer surface of the ring
2) A layer of brittle appearance. In some pictures this layer is directly in contact with the metal surface and in others it is fractured into several layers, sometimes even separated from the metal surface. The thickness of this layer varies from 3 to 70 μm. The EDX-mapping shows that its main components are Fe and O so that it is assumed to consist mainly of iron oxide.
3) Particulates on the aforementioned layer. Some have the appearance of crystals. The diameter of the constituent particles varies from 1 to 10 μm. Their composition is determined by EDX-mapping of the whole zone. The main components are K, Cl, S, Zn and O so that the presence of KCl, K_2SO_4 and ZnO may be assumed. There is a well-defined chloride layer (Figure 4.3) while Zn-containing particulates look like small crystals (Figure 4.4). The relative amounts of the different components depend on the experimental parameters and the position on the ring.

Examples of SEM/BSE micrographs and EDX maps of the 10CrMo9-10 ring labelled according to the main component of the particulate layer are included in Figure 4.3.

Sanicro 28 rings

No significant oxide layer was found on the Sanicro 28 rings in any of the experiments performed. The microscope images showed that the metal surface was covered by deposits rich in K, Cl, Zn and S, as shown in Figure 4.4.

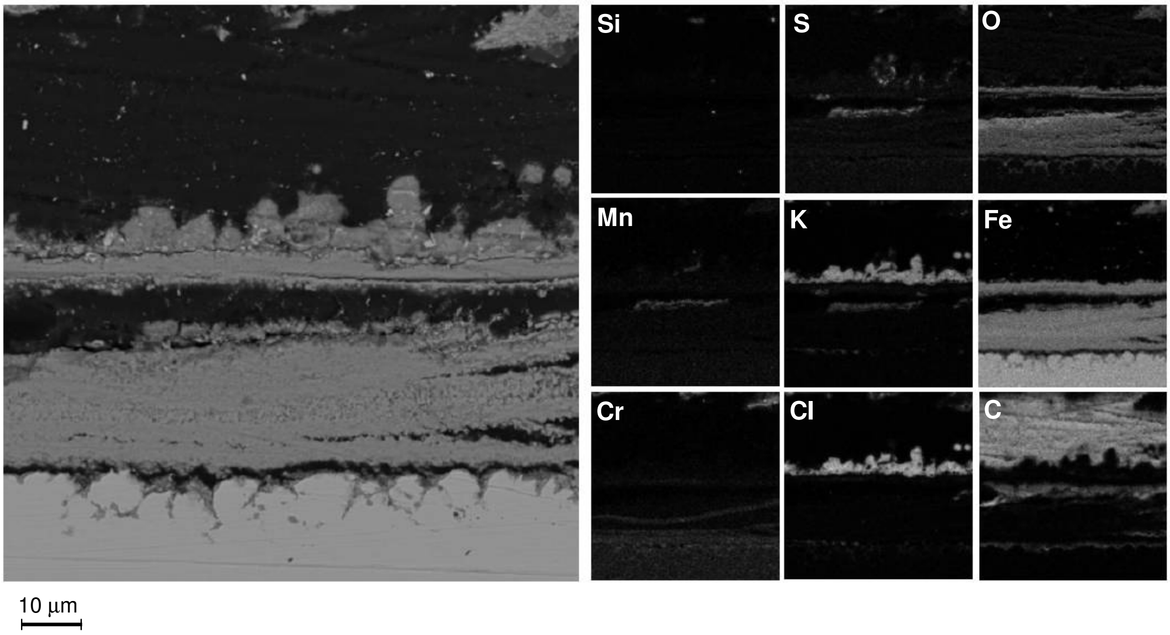

Figure 4.3: SEM/BSE image and EDX maps of the probe's rings: material: 10CrMo9-10; position: 180°; run: 2.

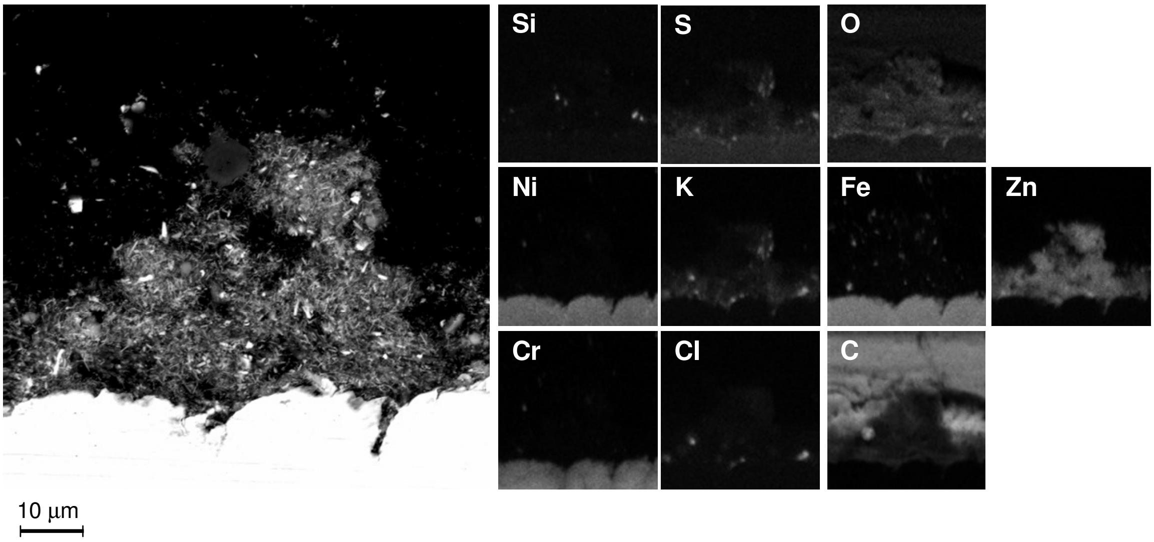

Figure 4.4: SEM/BSE image and EDX maps of the probe's rings: material: Sanicro 28; position: 45°; run: 2.

Images prepared by the Process Chemistry Centre of the Åbo Akademi University

4.3.2 Oxide layer thickness

The thickness of the oxide layer is used as indicator of the corrosion progress although in some cases it may not be proportional to the average corrosion rate (for instance if the oxide layer splits off the probe during exposure time or probe preparation) [23]. As already mentioned, corrosion was observed for all the 10CrMo9-10 rings while S28 rings remained intact during all the experiments. Figure 4.5 shows the average thickness of the oxide layer measured on the 10CrMo9-10 rings. The error bars are calculated based on the standard deviation of the measured thickness. It can be observed that the oxide layer is, as expected, thicker after the experiments with higher probe temperatures and higher $ZnCl_2$ content in the fuel (WP0.5%). A maximum thickness of about 70 µm was obtained with WP0.5% at a probe temperature of 550 °C. In terms of reproducibility the repetition of the test led to a maximum thickness of about 40 µm.

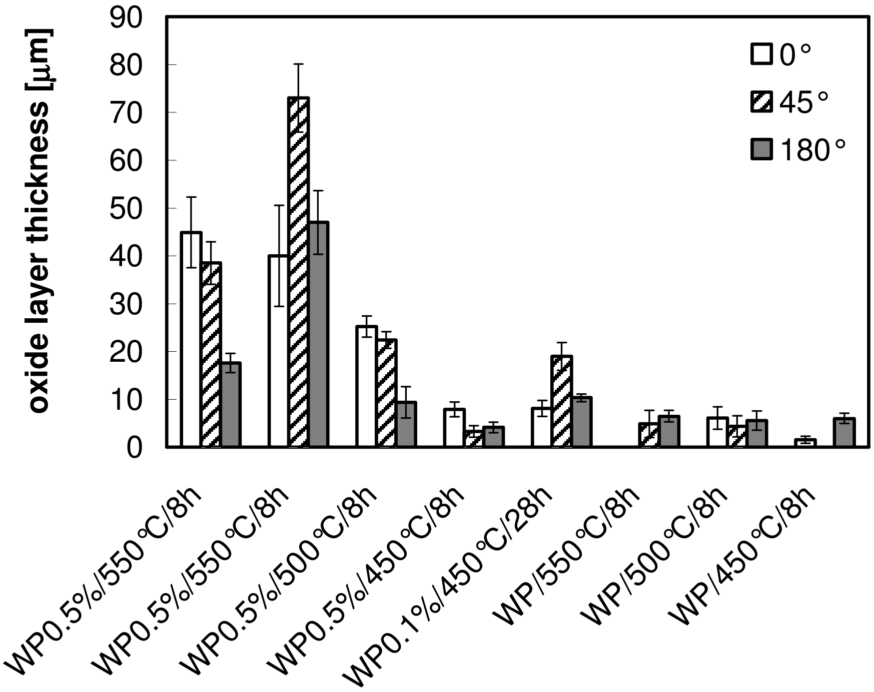

Figure 4.5: Oxide layer thickness for 10CrMo9-10 rings (positions 0, 45 and 180° as described in Figure 4.1)

The measured oxide layer thickness varies strongly with respect to position on the ring. After the experiments with highly corrosive fuels, the lowest thickness of the oxide layer is always found at the 180° position (in the other experiments the average thickness was not enough for any significant variation to be noticed).

4.3.3 Metal loss

The small metal losses obtained during these short tests are difficult to measure even by the metallographic analysis of the rings. Table 4.3 shows the measured losses in wall thickness. Although Sanicro rings do not show any sign of corrosion in the micrographs, the measured thickness losses are similar to those of 10CrMo9-10, see Table 4.3. It must be considered that in this case the diameter variations due to the exposure of the materials to high temperatures could be more significant than the metal losses due to corrosion. This could explain the results obtained.

Table 4.3: Calculated metal losses

Run #	ring material	wall thickness loss [µm]	oxide layer thickness [µm]
1	10CrMo9-10	15	34
2	10CrMo9-10	7.5	53
3	10CrMo9-10	5	19
1	S28	30	0
2	S28	10	0
3	S28	12.5	0

4.4 Discussion

The results from the metallographic analysis do however provide a good basis for the comparison of the small-scale tests with those performed in real plants and other research facilities. The structure of the scale described in section 4.3 will be compared with that observed by other research groups. In the work of Bankiewicz *et al.* [76] conditions similar to that of the combustion reactor used in this work were reproduced in a laboratory oven with a controlled atmosphere. Metal probes of 10CrMo9-10 and Sanicro 28 were covered with $ZnCl_2$ salts and exposed to high temperatures and a synthetic atmosphere for 168 hours. The morphology of the corrosion products obtained is similar to that observed in this work. The results of the small-scale tests confirm that the assumptions (simplifications) made in the laboratory were justified. Similar structures were also obtained in the laboratory tests of van Lith *et al.* [82].

In the work of Davidsson *et al.* [83] a corrosion probe (with a surface temperature of 500 °C) was exposed to the flue gases of a circulating fluidised bed (CFB) boiler for one hour. The fuels used were a mixture of wood chips and wood pellets with additional HCl(aq) or SO_2(g). After one hour of exposure a thin oxide layer of between 50 and 100 nm thickness was found, the outer part of which was rich in potassium. The very thin oxide layers were measured by Auger Electron Spectroscopy (AES) of the rings. Although Davidsson's work cannot be compared quantitatively with the results presented here, both observed a similar morphology of the corroded surfaces. The main difference is the absence of chlorine on Davidsson's probe.

Jensen *et al.* [31] investigated the scale accumulated on probes, which were exposed to the flue gases of biomass-fired boilers for 1000 h. In this work the structure obtained consists of a first oxide layer (~1000 μm), followed by a KCl-rich layer (~1000 μm) and finally a mixed layer containing mainly K, S, Cl and O. The oxide layer and the KCl-rich layer could also be observed on the probes in this work, though they were not as thick as on Jensen's probes. However, no mixed layer on top of the chloride layer was found in this work. The exposure time may have been too short for a measurable amount of deposits to accumulate on the probe. In the work of Davidsson no significant deposit layer was found either.

Examples of scale formed on probes exposed to the flue gases of EfW plants can be found in the work of Waldmann [21]. Oxides and a matrix of K, Ca, S, Cl and O similar to that described by Jensen *et al.* are also found in the outer part of the scale in Waldmann's work. In the inner part (close to the metal surface) there is a chlorine-rich layer. In some plants a sulphur-rich layer is found on top of the chlorine layer. Waldmann reports that this layer can be already observed after very short exposure times. In the probes used in this work for the metallographic tests, no chlorine layer was detected.

4.5 Summary

The metallographic tests showed that oxide layers of some micrometres thickness were obtained after 8 hours of exposure to the combustion gases of the small-scale facility. On the 10CrMo9-10 rings oxide layers of between 3 and 70 µm were obtained. A good correlation between the oxide layer thickness and the $ZnCl_2$ content of the fuel was established: the higher the $ZnCl_2$ content in the fuel, the thicker the oxide layer obtained. However the reproducibility of the oxide layer thicknes was limited, the repetition of the same tests showed thickness differences in the order of magnitude of about 30 µm. On the Sanicro 28 rings no significant oxide layer was observed. The corrosion products on the rings could be studied very accurately (in terms of morphology, composition, etc.). Even after such a short exposure time useful information could be obtained concerning the corrosion mechanisms. However, a quantitative analysis of the corrosion rate was not possible. These tests have shown how problematic the short-term measurement of corrosion rates (in terms of oxide layer growth) is when using standard equipment. Even with the highly doped fuels (containing $ZnCl_2$) and low alloy steels (10CrMo9-10), the metal losses obtained after such a short exposure time could not be quantified properly.

In this study only the quantification of the corrosion rate (metal loss and oxide layer thickness) was taken into account. The role of $ZnCl_2$ on high-temperature corrosion has been investigated in detail in the PhD Thesis of Bankiewicz "High temperature corrosion of steam tube materials exposed to zinc and salt mixtures" and reported in a further publication [77].

5 Iron loss tests

As was shown in chapter 4 the metallographic analysis of probes used in short-term tests is inadequate for the measurement of small metal losses. Although the structure of the corrosion products could be analysed accurately, no significant thickness loss of the rings could be measured. Table 5.1 shows typical metal losses for high, medium and low corrosion rates of high-temperature steels in superheaters of biomass and EfW power plants. In the simplified case of a constant corrosion rate, the expected loss in thickness for an exposure time of 8 hours is also included. Even with metallographic techniques the measurement of such small losses under the conditions in small-scale combustion reactors is subject to significant errors, as discussed in chapter 4.

Table 5.1: Typical metal losses in a power plant

	mm/a	µm/h	µm/8h
High corrosion	5	0.625	5
Medium corrosion	0.5	0.0625	0.5
Low corrosion	0.05	0.00625	0.05

The approach of the method proposed in this section is the use of pure iron instead of steel in order to obtain greater metal losses, which are easier to measure after short exposure times. Whether or not the quantitative results of iron loss test (electrolytic) can be used to infer the corresponding values for steel should be subject to further investigations. The aim of this work is to evaluate the suitability of this method for the qualitative comparison of different combustion parameters like fuel or flue gas temperature during short-term tests that can be performed within one day (t < 8 hours). The first measurements of this kind were performed in the work of Ottmann [66]. Fe losses of some micrometres were measured (they are included and commented later in this chapter). In this work the process was optimised, further measurements were carried out and the results were evaluated.

5.1 Measuring set-up

The probe is a heat pipe cooled to the temperature of interest. This heat pipe simulates a superheater in a power plant with temperatures between 400 °C and 600 °C. A heat pipe is a sealed tube filled with a working fluid. A picture of one of the heat pipes used for this work is shown in Figure 5.1. The tube material is Inconel© 600, a nickel- and chromium-based steel alloy used for high-temperature applications. One part of the tube is heated; this part is called the evaporator (right-hand side of the heat pipe in Figure 5.1). The evaporator is introduced in the reactor and exposed to the hot flue gas. The working fluid inside the tube evaporates in this part and flows to the colder part of the tube, located outside the reactor (left-hand side of the heat pipe in Figure 5.1). This part is cooled down with pressurised air so that the working fluid condenses. The temperature reached by cooling is the boiling point of the working fluid at the pressure inside the tube [84]. In this case the working fluid is caesium (Cs p_{at} ~ 1 bar: T_{sat} ~ 675 °C [84]). The temperature of the heat pipe is measured by means of a thermocouple inserted in it.

Figure 5.1: Heat pipe used as a corrosion probe for the iron loss tests

The main advantage of the use of heat pipes for this application is the constant temperature along its whole length due to the saturated state of the working fluid inside the tube. This is a similar situation to that of the real superheater tubes. In probes cooled with pressurised air like the ones used in the other chapters, temperature gradients along the tube may affect the corrosion rates measured.

The set-up for these tests can be seen in Figure 5.2. It consists of two heat pipes (d = 12 mm, l = 75 mm) and three dummy tubes along the flue gas path. The dummy tubes are responsible for a uniform distribution of the flue gas around the heat pipes as well as for obtaining a flue gas velocity of around 10 m/s. According to [16] and [85] corrosion is influenced by flue gas velocity: the higher the flue gas velocity, the higher the corrosion risk. The set-up is installed at position A in Figure 3.3. Two thermocouples measure the flue gas temperature before and after the heat pipes.

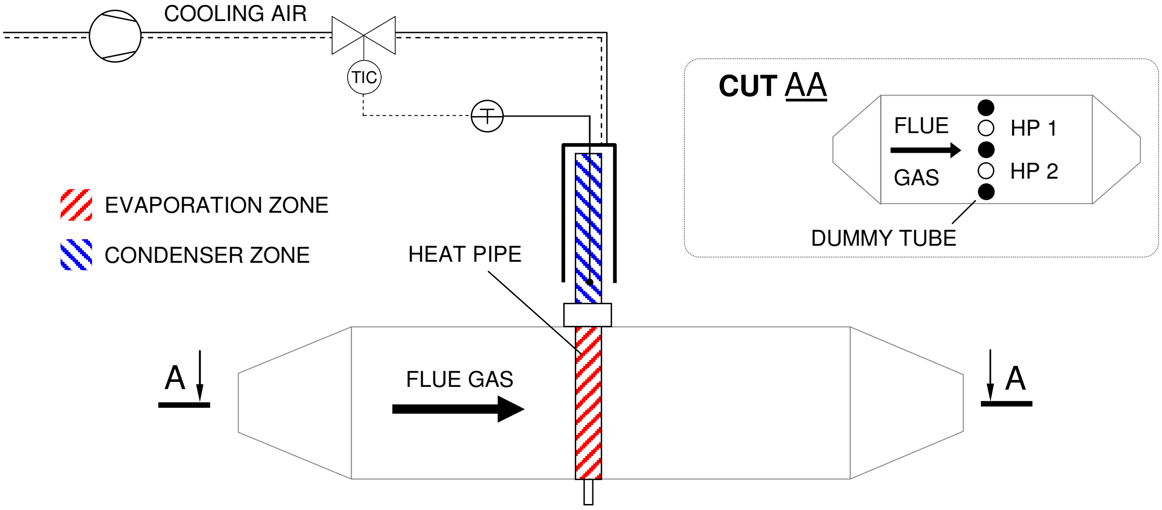

Figure 5.2: Heat pipe set-up for the iron loss tests

5.2 Measuring procedure

The evaporator surface on the heat pipe (the surface that is going to be introduced in the reactor) is electrochemically coated with an iron layer and the thickness of the iron layer is measured before and after the exposure to the flue gases. The corrosion rate is expressed in terms of iron thickness loss of the heat pipes.

In Ottmann's work [66] different ways to measure the iron thickness were evaluated and X-ray fluorescence (XRF) spectroscopy was favoured. This technique measures the fluorescence of the material. If a copper layer is deposited before the iron layer, the thickness of the iron layer can be inferred from the differences in the intensity of copper and iron XRF spectra obtained. Copper has an XRF spectrum very different to that of iron, which enables one to measure very small changes in iron layer thickness. The iron layer thickness is measured before and after combustion at five points: two points are located on the windward side (0°), two points on the lee side (180°) and one point on the lateral side

(90°). The positions are shown in Figure 5.3. Each measurement is repeated three times at each measuring point.

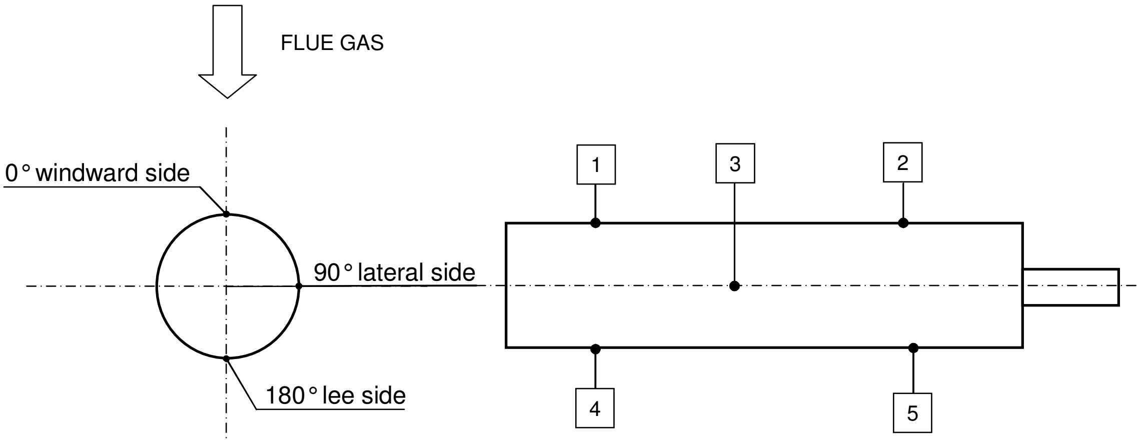

Figure 5.3: Position of the measuring points on the heat pipe

The heat pipes are exposed to the flue gases from the beginning of the combustion. First they are cooled to about 20 °C. Once equilibrium conditions are reached in the reactor the cooling of the heat pipes is reduced until each heat pipe reaches the temperature of interest. The heat pipes are exposed to the combustion flue gases at this constant temperature for one hour (this duration will be referred to as test time). The facility is then switched off and once it has cooled down the heat pipes are removed. Corrosion products are removed from the heat pipes' surfaces by pickling according to [81]. After oxide removal the iron layer thickness is measured again at the same five points and the iron loss is then calculated. Figure 5.4 schematically summarises the measuring procedure.

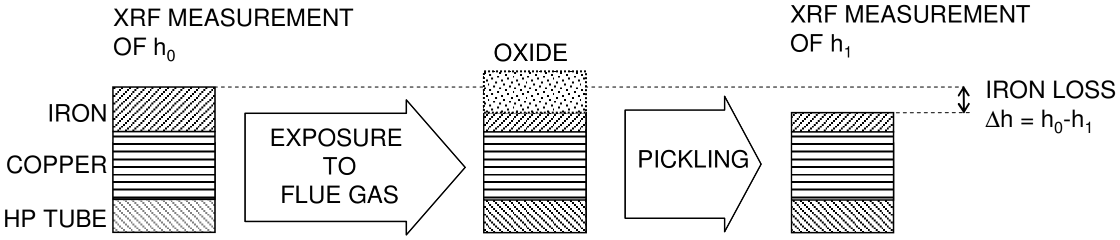

Figure 5.4: Iron loss measuring procedure

5.2.1 Electrochemical coating

Iron coating has important industrial applications such as the manufacture of printing plates [86]. In this work the probes were coated with iron at in-house laboratories. Several laboratory studies were carried out to further optimise the electrochemical coating procedure used in previous work [66]. During these tests the treatment of the surface prior to coating proved to play an important role in the quality of the iron layer. Cleaning, chemical degreasing, neutralising and activating the surface before coating turned out to be imperative for obtaining a smooth and non-porous iron layer. After cleaning, the heat pipe was electrochemically degreased using an alkali salt solution and a stainless steel anode. Then the heat pipe was immersed in a 10% hydrochloric acid solution in order to neutralise and activate its surface for coating. Degreasing, neutralising and the activation of the heat pipe's surface were performed in the laboratories of the Max Planck Institute of Plasma Physics in Garching, where the X-ray measurements took place, too.

Various standard electrolytes are proposed in the literature for iron coating, such as ferrous chloride, ferrous sulphate and ferrous fluoroborate solutions [86]. Out of all of these, the ferrous sulphate electrolyte has yielded the best laboratory results. The electrochemical parameters selected for the coating are summarised in Table 5.2. A new solution was prepared for each heat pipe since experiments showed that impurities strongly affected the quality of the deposited layer. After coating the heat pipe was cleaned and polished.

Table 5.2: Parameters for electrochemical coating

Solution	Anode material	pH	T [°C]	i [A/dm^2]	t [min]
250 g/ℓ $FeSO_4 \cdot 7H_2O$ 42 g/ℓ $FeCl_2 \cdot 4H_2O$ 20 g/ℓ NH_4Cl	ARMCO (Fe 99.8-99.9%)	2.5-3	40-43	11	20 min

5.2.2 Oxide removal

The removal of the oxide layer can be mechanical (e.g. polishing, ultrasound) or chemical (pickling) [23]. In previous work [66], the oxide layer turned out to be very difficult to remove mechanically from the heat pipe’s surface and therefore the chemical approach was decided upon for this work. The oxide layer was easier to remove by pickling. Different commercially available pickling solutions were tested and finally a phosphoric acid solution was selected (SurTec471). In [23] a further list of appropriate pickling solutions for different steels can be found.

5.3 Test parameters

The test matrix is displayed in Table 5.3. Flue gas and probe temperatures were selected on the basis of the Flingern corrosion diagram (see Figure 2.1). The selected flue gas temperature for the tests is 750 °C. The tube temperatures chosen for the tests range from 400 °C to 500 °C.

Table 5.3: Iron loss test matrix

Run #	Fuel	T_{HP1} [°C]	T_{HP2} [°C]
1	WP	400	400
2	WP	450	500
3	WP+S/Cl 1.5	450	500
4	WP+S/Cl 0.8	400	450
5	WP+S/Cl 0.02	400	450
6	WP+S/Cl 0.02	500	500

These temperatures are indicated in the Flingern corrosion diagram in Figure 5.5.

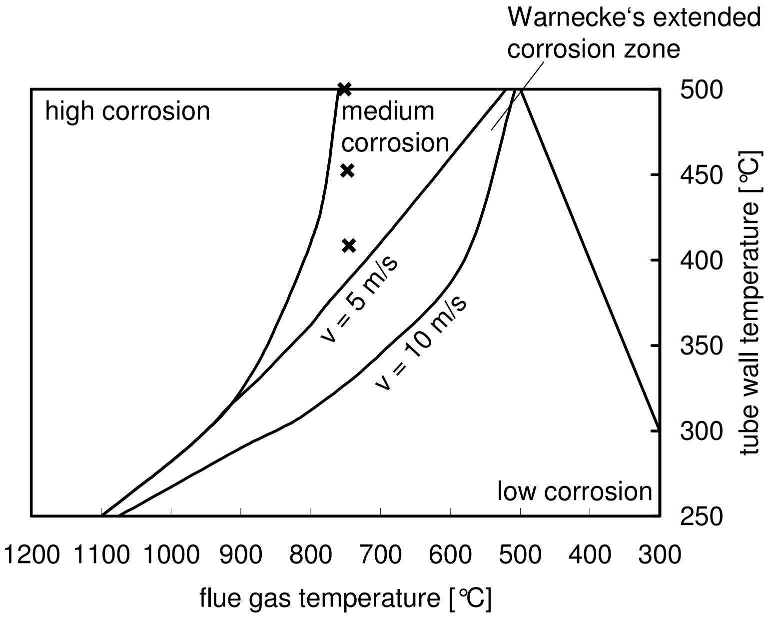

Figure 5.5: Position of the iron loss probes in the Flingern corrosion diagram

As can be seen in the diagram, they are located in the area between high and low corrosion zones. The fuels used were S- and Cl-doped wood pellets (see section 3.2).

5.4 Results

Significant iron losses could be measured with all the fuels after one hour of exposure. The measured iron losses are included in Table 5.4.

They vary between 1.7 µm/h for WP and 25 µm/h for WP+S/Cl 0.02. The highest metal losses obtained with WP+S/Cl 0.02 are even slightly above the limit of thickness losses measurable with the XRF device. During this test the iron layer was completely corroded and no iron could be detected on the surface of the pipe after its exposure to the flue gas. According to Figure 3.4 this fuel's chlorine content corresponds to the highest value expected in natural biomasses and it has a very low S/Cl ratio. Taking this as the worst-case scenario, the exposure of the heat pipes to flue gases for one hour is sufficient to compare the corrosive influence of biomass fuels.

The obtained iron losses are generally higher than the ones reported in previous work, where maximum values for WP with a S/Cl ratio of 0.02 were about 15 µm/h. This fact could be attributed to the optimisation of the oxide layer removal. Remains of iron-containing oxides on the tube surface increase the iron thickness inferred from the XRF measurements after the experiments and thus reduce the calculated iron loss. The pickling procedure has proved to be much more effective and appropriate for the removal of the oxide layer than mechanical polishing.

Table 5.4: Measured iron losses ($T_{flue\ gas}$ = 750 °C)

fuel	T_{tube} [°C]	iron loss rate [µm/h]
WP	400	2.1
WP	400	1.7
WP	450	2.4
WP	500	2.3
WP+S/Cl 0.02	450	19.0
WP+S/Cl 0.02	500	20.1
WP+S/Cl 0.02	400	16.4
WP+S/Cl 0.02	500	25.0
WP+S/Cl 0.8	400	9.0
WP+S/Cl 0.8	500	12.5
WP+S/Cl 1.5	400	6.1
WP+S/Cl 1.5	500	7.0

5.4.1 Error margins for the XRF measurements

The first source of error is associated with the measuring procedure itself. The accuracy of the X-ray fluorescence spectroscopy device determines the thickness loss to within ±0.01 µm, so this error can be neglected. At every point the measurement is repeated three times before the combustion experiment and three times afterwards. The mean value and the standard deviation for every point are calculated according to equations (2) and (4) in the DIN 1319 standard [87].

$$\overline{h} = \frac{1}{3}\sum_{j=1}^{3} h_j \qquad \text{Eq. 1}$$

$$\delta h_{point} = \frac{\sigma}{\sqrt{n}} = \sqrt{\frac{1}{n(n-1)}\sum_{j=1}^{3}(h_j - \overline{h})^2} \qquad \text{Eq. 2}$$

The iron thickness loss for a certain point is calculated as follows:

$$\Delta h = \overline{h}_0 - \overline{h}_1 \pm \sqrt{\delta h_0^2 + \delta h_1^2}\ , \qquad \text{Eq. 3}$$

where h_i is the iron layer thickness, $\overline{h}$ is the average iron layer thickness, n the number of measurements and σ the standard deviation. The subscript indices 0 and 1 correspond to the measurements before and after exposure respectively. Due to the physical impossibility of measuring at exactly the same position before and after the tests and due to the difficulty of quantifying this error the maximal deviation obtained will be considered the worst-case scenario for all the measured values. The maximal deviation of an individual measured thickness δh_{max} has a value of ±0.6 µm. From that value the maximal deviation of the calculated iron thickness loss at each point can be estimated according to Eq. 2 and has a value of ±0.8 µm.

The second source of error is associated with the reproducibility tests. Several combustion tests were performed under exactly the same conditions. Table 5.4 shows the tests and the values obtained. Considering the deviations calculated at every point with Eq. 2 a total maximal deviation of ± 3.3 µm is obtained.

Finally the oxide removal by pickling adds some additional error since a small part of the pure iron is also removed chemically with the oxide layer. This error was quantified in the first experiments in the laboratory and has a maximal value of about 1 µm. This means the iron loss could be overestimated by 1 µm.

To summarise, a total maximal deviation (+3.3, -4.3) µm is assumed as a worst-case scenario for every measurement. Measurement values range from 0 to 20 µm, which means the maximal deviation is approximately one fifth of the total measuring range. This high deviation is one of the main limitations of this measuring procedure.

5.4.2 Variations of the measured corrosion rate with respect to position on the corrosion probe

Although the literature often reports a different behaviour of iron corrosion on the windward and lee sides of the corrosion probes, this effect could not be detected during these tests.

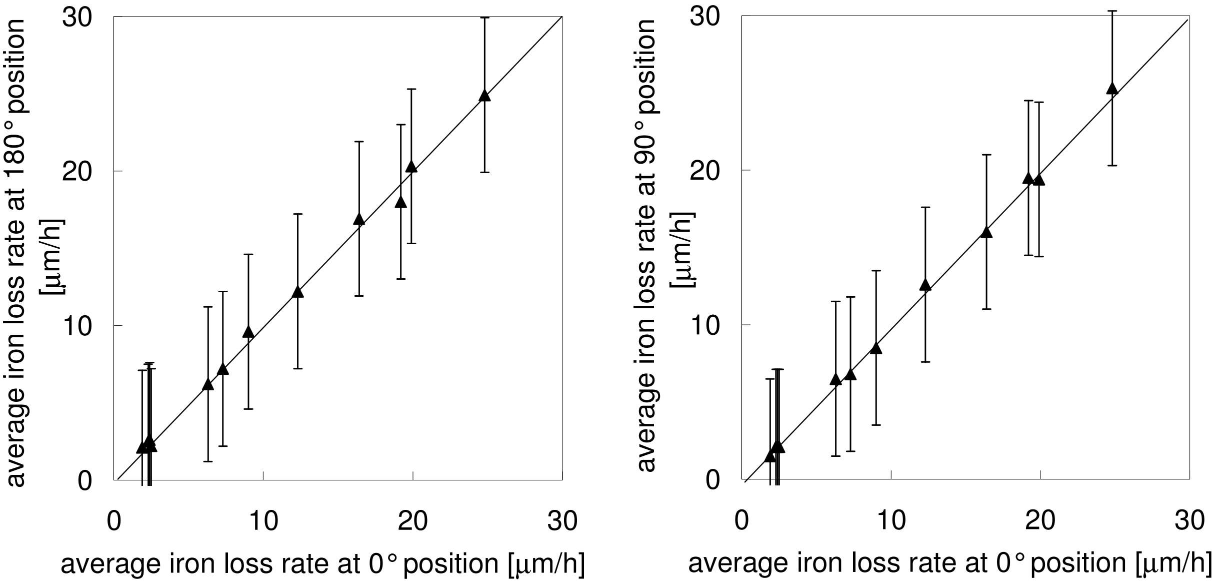

Figure 5.6: Comparison of the iron loss measurements on the windward (0°), lee (180°) and lateral (90°) sides of the probe

As can be seen in Figure 5.6 the comparison of the mean thickness losses for windward, lee and lateral sides shows no significant correlation. Perhaps the uncertainty of the measurements is too large to measure the differences or the tests are too short to discern this behaviour. In any case the results of the metallographic measurements described in Section 4.3.2 did show a clear correlation between corrosion rate and position on the probe. Reliable conclusions can only be drawn after longer tests, such as those lasting around 1000 h described in the literature.

5.4.3 Influence of fuel type and tube temperature

Figure 5.7 shows the thickness loss as function of the S/Cl ratio.

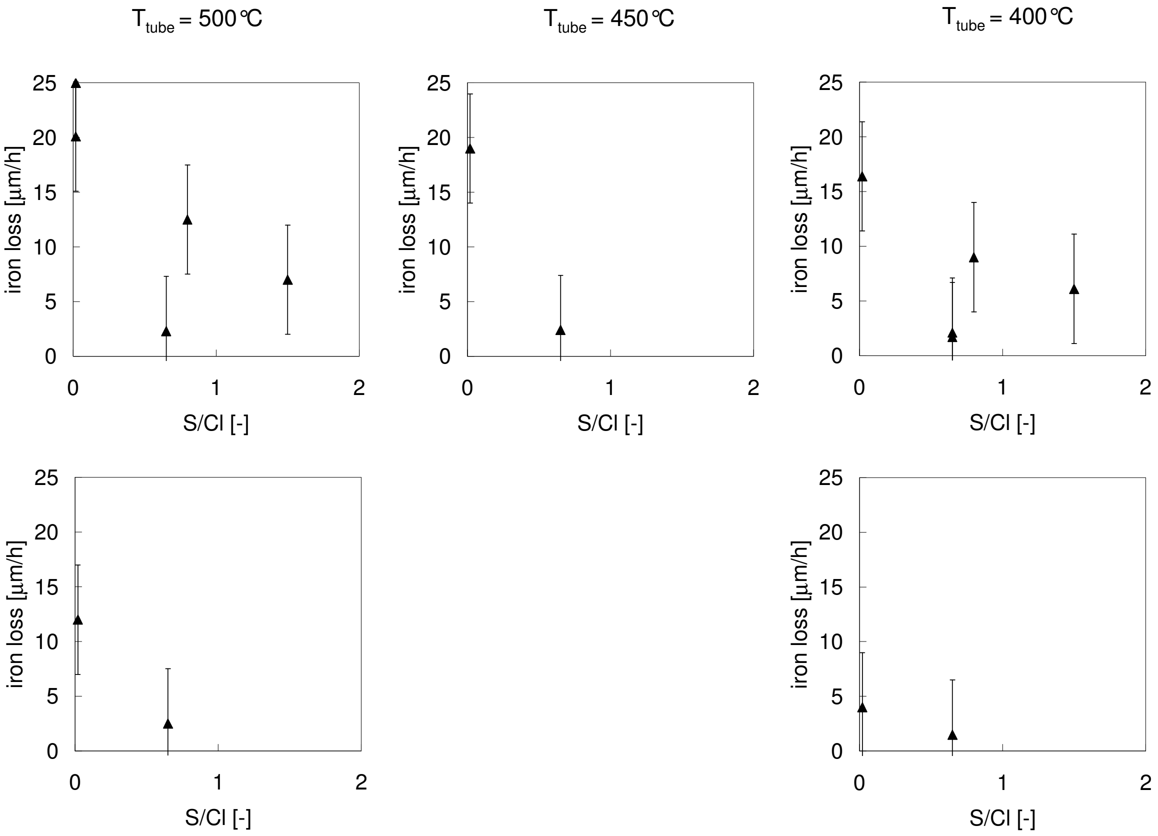

Figure 5.7: Measured iron losses as a function of the S/Cl ratio for different tube temperatures (top); Measured iron losses in Ottmann [66] (bottom)

These results are compared with those from previous work, where the same tendency was observed: the lower the S/Cl ratio, the higher the metal loss measured. An exception is wood, whose S/Cl ratio is relatively high due to a very low chlorine content.

Figure 5.8 shows the thickness loss as function of the Cl content in the fuel. It can be observed that the iron loss increases with the chlorine content as expected. Although the S/Cl ratio for wood is relatively high, its chlorine content is very low and so are the iron losses for this fuel. In this series of measurements fuels with high chlorine contents had also the lowest S/Cl ratios. It would be interesting to further investigate the corrosion behaviour of fuels with high chlorine levels and high S/Cl ratios in order to observe the influence of the sulphur on the corrosion mechanism. Also different bed additives having an influence on the S/Cl ratio could be tested.

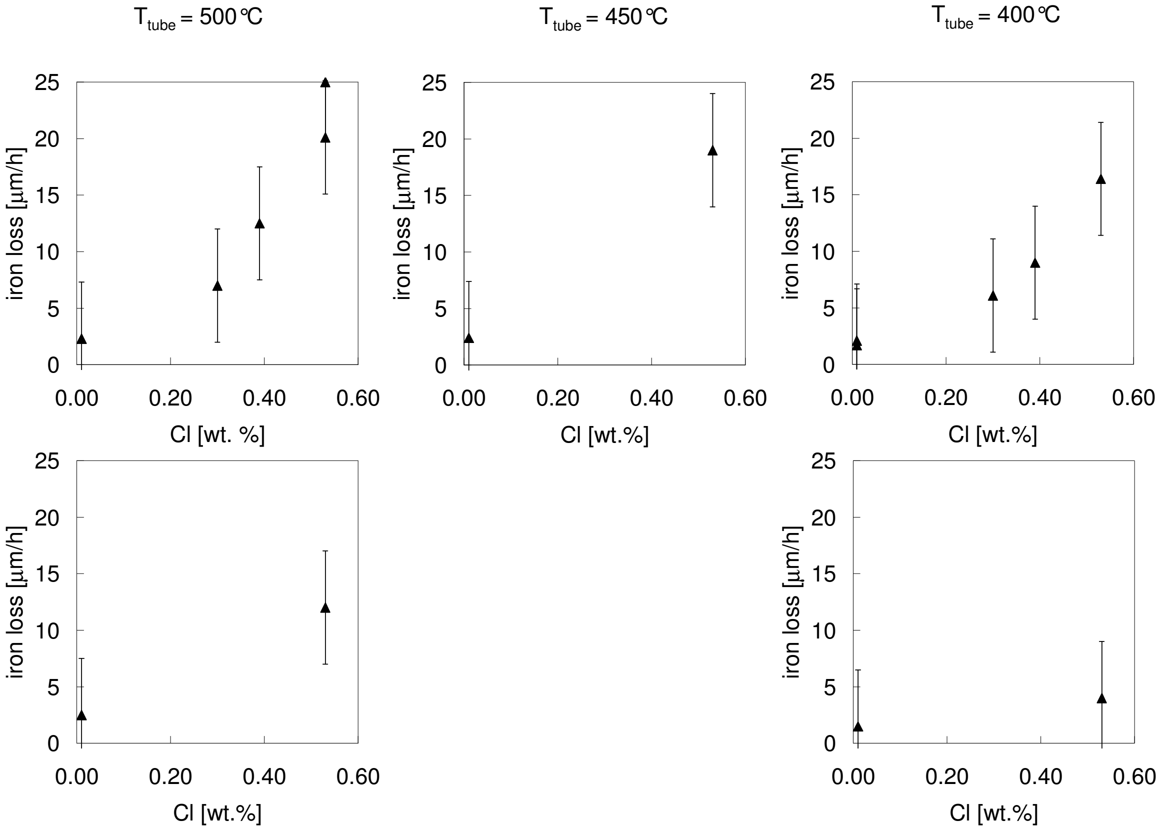

Figure 5.8: Measured iron losses as a function of the Cl content for different tube temperatures (top); Measured iron losses in Ottmann [66] (bottom)

However, it must be remarked that in these figures the standard deviation often has the same order of magnitude as the measured iron loss values or the differences in these values between different fuels. For different S/Cl ratios the error bars around the measured iron loss values can even overlap, so there is considerable uncertainty concerning the correlation observed.

Figure 5.9 (top) shows the dependence of iron losses on the tube temperature. For WP+S/Cl 0.02 the metal loss increased sharply between 400 and 500 °C tube temperature: the higher the S/Cl ratio, the lower the influence of the tube temperature on the measured iron losses. For WP the metal loss was almost constant over the whole temperature range investigated. Similar effects were already measured in previous research [66], see

Figure 5.9 (bottom). The overlapping error bars reveal the limitations of this method of measuring corrosion rates.

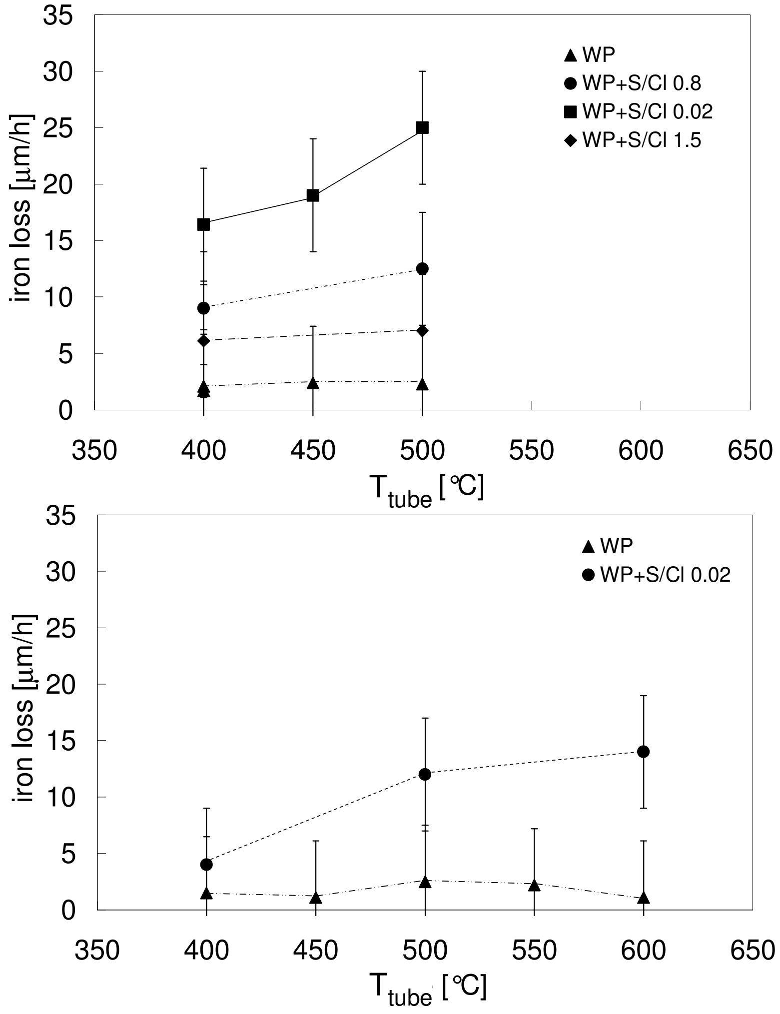

Figure 5.9: Measured iron losses as a function of the tube temperature for different fuels (top); Measured iron losses in Ottmann [74] (bottom)

The iron loss rates measured vary from 1 to 25 µm/h, i.e. around 5 to 200 mm/year. These values will be compared with metal loss rates reported in the literature. Several researchers have investigated metal losses on real superheater tubes after a relatively long exposure to the flue gases. In the field of waste combustion Krause reports metal losses for carbon steel and Alloy 825 exposed to flue gases for 80 to 800 h in a EfW plant [26]. The metal loss rates measured are around 10 to 100 mm/year for carbon steel and 0.01 to 25 mm/year for Alloy 825. Kawahara reports values of around 2 mm/year for Alloy 625 in the superheater tubes of a CFB waste boiler [25]. Andersson *et al.* also measured metal loss rates between

5 and 25 mm/year for a selection of Cr- and Ni- rich steels in a test coil inserted in a CFB waste boiler [88, 89]. In the work of Horn *et al.* the metal loss rates measured on 15Mo3 in different plants after several months of operation vary from 1 to 20 mm/year [20]. Figure 5.10 shows the metal losses reported in the literature and the iron losses obtained in this work.

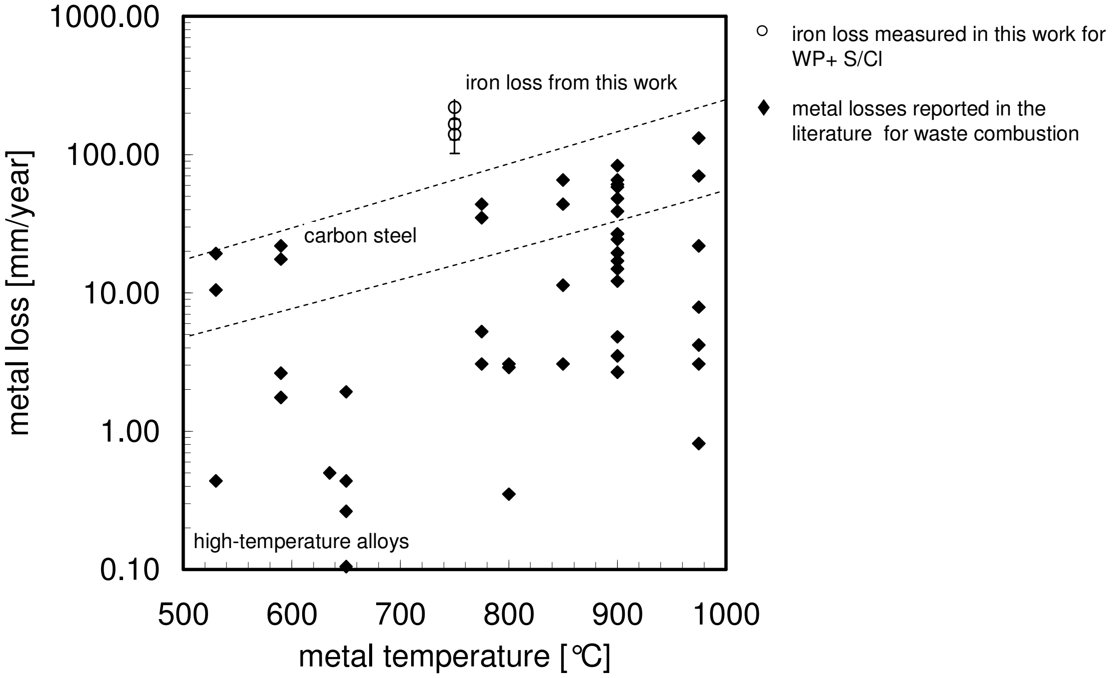

Figure 5.10: Comparison of iron losses with metal losses reported in the literature for waste combustion (adapted from [23, 26])

Only tube temperatures between 370 and 530 °C have been considered (the tube temperatures in this work vary between 400 and 500 °C). As expected, the metal losses increase with the flue gas temperature and are always lower for Cr- and Ni-rich steels than for carbon steel. The iron loss rates measured in this work are around one order of magnitude higher than those measured on carbon steel and two orders of magnitude higher than those measured on high-temperature alloys.

Using biomass fuels Hendersson *et al.* [90] measured loss rates of around 0.01 to 0.1 mm/year on high-temperature alloys in wood-fired boilers and Jensen *et al.* reports slightly higher values for straw combustion [31]. Figure 5.11 compares the literature values with the values from this work. The iron losses are also around one order of magnitude higher than the values reported in the literature.

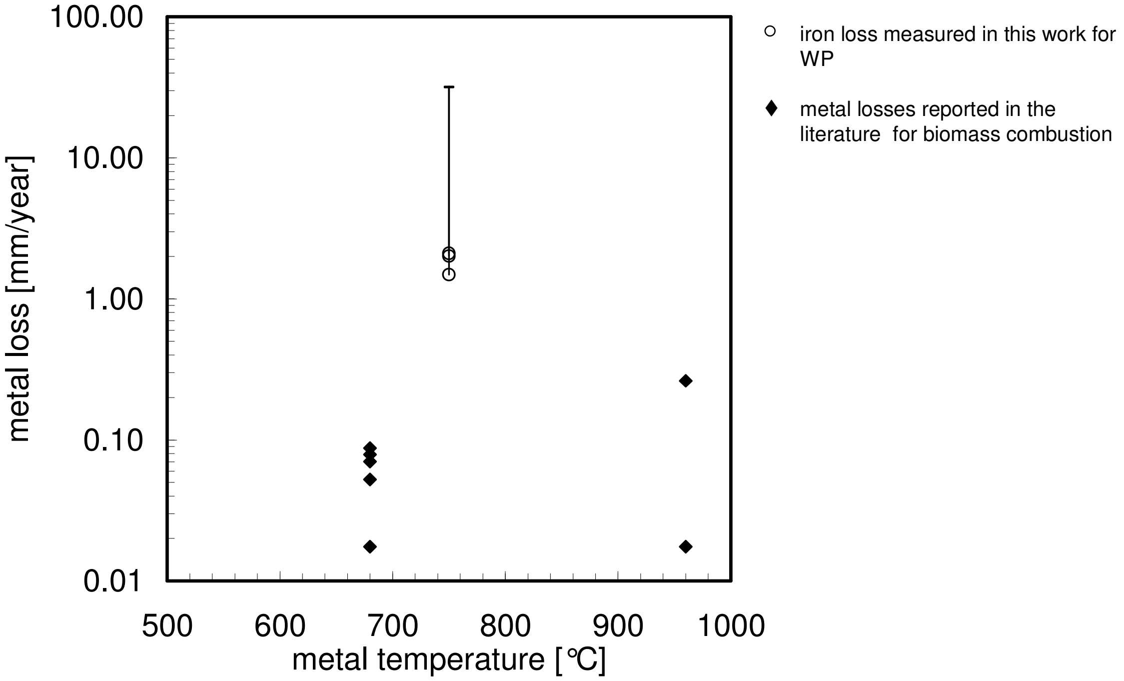

Figure 5.11: Comparison of iron losses (red) with metal losses reported in the literature for biomass combustion (black) (adapted from [90])

The calculation of the previous metal loss rates has been based on the assumption that the corrosion rates are constant over the whole exposure time. This strong simplification enables one to compare the results from tests with different exposure times. For a more precise calculation of the metal loss rates the corrosion kinetics explained in section 2.1.2 must be taken into account.

The main drawback of the measurements performed in this chapter is the high uncertainty of the measured thickness losses in comparison to the measuring range. The calculated error bars are around 8 µm wide. This is in the same order of magnitude as the iron losses measured and approximately one third of the available measuring range. Longer tests (~ 8 h) could yield higher corrosion rates so as to render this error negligible, but this option cannot be considered since the maximum thickness that can be measured by the X-ray spectrometry equipment used here is limited to 25 µm (supplier specifications vary from 20 to 40 µm). In Figure 5.12, where iron loss rates are plotted against temperature, two distinct zones can be identified: the first indicates high corrosion potential, in the same order of magnitude as the corrosion observed during the combustion of straw at temperatures between 400 and 500 °C; the second indicates low corrosion potential, in the same order of magnitude as the corrosion observed during the combustion of wood at temperatures between 400 and 500 °C. Due to the calculated measuring uncertainties, points lying in between these zones cannot be classified.

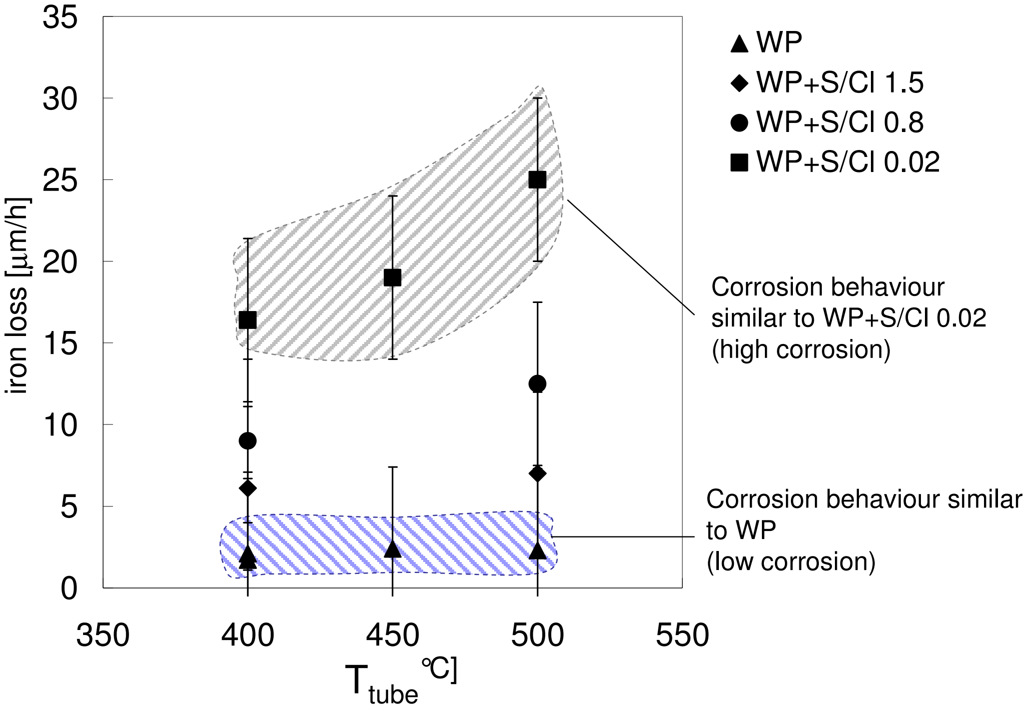

Figure 5.12: Zones of high and low corrosion for the iron loss tests

This classification scheme provides a rough estimate of the corrosion potential of certain fuels and combustion parameters.

The iron losses measured varied between 1 and 25 µm, whereby the upper limit was imposed by the maximum measurable range of the XRF device. Although other commercially available devices can measure iron losses of up to 40 µm, this is still the main limitation of this measuring technique. Two alternative options are considered:

- Use of an air-cooled probe instead of a heat pipe: the use of a heat pipe as a probe has the advantage of a constant temperature along the whole probe surface, as mentioned earlier. However if a normal air-cooled copper tube is used instead, the decrease in thickness of the iron coating could be measured by cutting the tube and observing the cross section under a microscope. The main advantage of this approach is that a more extensive measuring range could be investigated, so the error margins would be less significant. In this case the upper limit of the measuring range would be the thickness of the electrochemical coating. Above a certain thickness the required quality and uniformity of the iron layer could not be guaranteed.

- Use of iron tubes instead of iron coatings. The use of iron (ARMCO) tubes would avoid the electrochemical coating and could also be considered. This option however would be yield less accuracy in the case of small thickness losses. As described in chapter 4, small thickness losses (< 5 µm) are not easy to measure by metallographic analysis in a massive iron (or steel) cross section.

5.5 Summary

The iron loss measuring technique was proposed as an alternative to conventional corrosion measuring techniques. The main idea was the use of iron instead of steel in order to obtain high and therefore easily measurable metal losses within short periods of time. These experiments have confirmed that the iron losses obtained are higher than the metal losses observed in the metallographic tests.

The method has a very limited accuracy and measuring range. The calculated error bars are around 8 µm wide. This is in the same order of magnitude as the iron losses measured and approximately one third of the available measuring range. This fact restricts its applicability to situations where fast, cheap and first-hand information on corrosion behaviour is needed. This work has shown that this relatively simple measuring technique could enable one to classify fuels and combustion conditions as “highly corrosive” or “less corrosive” after short-term measurements (duration < 8 hours). This information could serve as a rough guide to the corrosive influence of certain combinations of parameters, thus helping to reduce the size of test matrices for more accurate and expensive tests by rendering the investigation of irrelevant factors unnecessary.

6 LPR Measurements

In the past few years, electrochemical corrosion monitoring techniques have experienced a rapid development towards high-temperature application in power plants. An overview of the main electrochemical techniques available was given in section 2.1.3. The main advantage of these techniques is that they can be applied online, i.e. during plant operation, and that they supply qualitative and quantitative information on the corrosion process. Future developments of online corrosion monitoring in power plants will allow (1) a better understanding of the corrosion process and the main factors that influence it, (2) improved plant operation due to counteractive measures against corrosion and (3) saving costs by means of shortened and better foreseen operational interruptions of the plant for maintenance purposes.

The linear polarisation resistance (LPR) sensor developed by the Institute for Experimental Physics I and II of the Augsburg University [21] is one of the few sensors that has proved suitable for long-term online measurements in power plants fired with biogenic solid fuels. Series of measurements of some months have been performed successfully in several EfW plants [21].

The aim of the work presented in this section was to evaluate the use of this monitoring technique for short-term tests in a small-scale facility. The LPR sensor was exposed to the flue gases of a small fluidised bed reactor for periods of between 3 and 30 hours.

6.1 Measuring principle

Polarisation measurements are applied extensively in the field of electrochemistry for the characterisation of electrochemical systems, that is, systems in which electrochemical reactions are involved. Electrochemical reactions are defined as chemical reactions whose main driving force is the exchange of electrical charges and whose behaviour can be explained in terms of electrical laws. In this case the measurement of the potential or current in an electrochemical system supplies useful information for the study of the reaction taking place in it (chemical species involved, reaction kinetics, etc.).

A detailed description of how the sensor works can be found in [21]. In the following, only a short introduction to the measuring principle of polarisation measurements is given. The aim is to provide the fundamentals necessary for the interpretation of the results in the final section.

6.1.1 Equilibrium conditions

The main electrochemical parameters will be explained on the basis of a very simple electrochemical system. The simplest electrochemical system is a substance in a solution of its own ions. According to electrochemical laws there is a continuous transfer of charges between the substance and the solution according to the equation $Z^+ + e^- \rightleftharpoons Z$. In one region the substance predominantly loses cations Z^+ that go into solution: $Z \rightarrow Z^+ + e^-$. This region is called the *anode*, the reaction in this direction is oxidation and its rate corresponds to the *anodic current* i_a. In another region the substance predominantly accepts cations from the solution: $Z^+ + e^- \rightarrow Z$. This part is called the *cathode*, the reaction in this direction is reduction and its rate corresponds to the *cathodic current* i_c. The solution (called the *electrolyte* in this context) is the component that closes the circuit, allowing the electrical charges to move between the anodic and cathodic regions. In equilibrium, both reactions have the same rate, that is, cathodic and anodic currents have the same value and opposite direction. The value of the cathodic and anodic current under steady-state conditions is called the *exchange current* i_o. According to this definition $i_a = -i_c = i_o$. The *external current i,* defined as the sum of cathodic and anodic currents, is therefore zero and cannot be measured: $i = i_c + i_a = 0$. In this state the material immersed in the solution attains a certain electric potential called its *free potential* E_o.

Corrosion is a chemical reaction of electrochemical nature [91]. The basic elements of the electrochemical system described above have their counterparts in a corroding metal (for example Fe) exposed to a chlorine-rich atmosphere. In this system the metal ions (Fe^{2+} and Fe^{3+}) leave the anode and do not return to the metal. This is the reason for the metal loss observed. Some electrochemical mechanisms for the complete corrosion process are proposed in [21]. According to the literature chlorine plays the most important role, as explained in section 2.1.1.

The *corrosion rate r* of the metal is proportional to the anodic current i_a of such a system, that is, the combined electric charge of all the iron cations leaving the metal per unit time. As already mentioned, anodic and cathodic currents have the same absolute value (the exchange current i_o) when the system is in equilibrium. In the literature i_o is therefore often called *corrosion current*. In this state the metal reaches a certain electric potential called its *free corrosion potential* E_o. The corrosion parameters described are represented in Figure 6.1

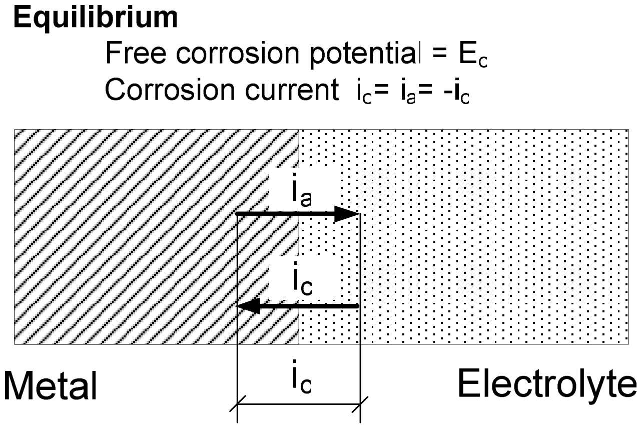

Figure 6.1: Corrosion parameters under equilibrium conditions

6.1.2 Polarisation

The aim of the polarisation measurements is to determine E_o and i_o in order to characterise the electrochemical system. At equilibrium conditions however, i_o is very difficult to measure. As already explained, the sum of cathodic and anodic currents in a system in equilibrium is zero and so no external current can be measured ($i = i_c + i_a = 0$). One of the standard solutions to this predicament is to polarise the system. For polarisation measurements an external DC voltage is applied between the metal and the electrolyte. The circuit is closed and the resulting current (or voltage) measured. The difference between the electric potential of the metal in this state and the free corrosion potential is called polarisation[1]. The metal-electrolyte system can be modelled by the idealised circuit shown in Figure 6.2, where U and I are the measured external voltage and current.

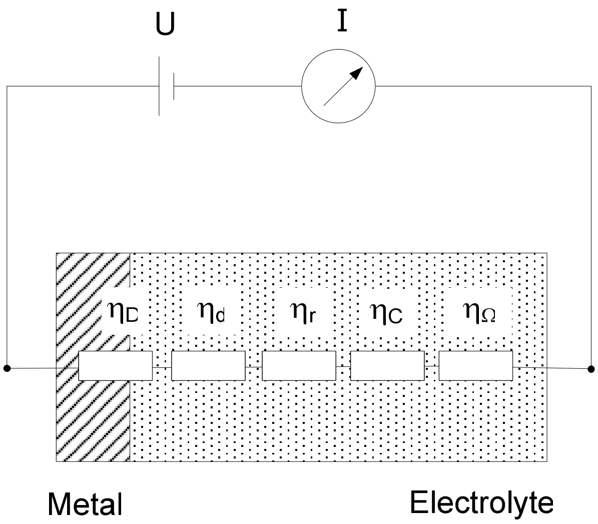

Figure 6.2: Types of polarisation

If the circuit is closed, five different kinds of polarisation (η) can arise, each of which is described in the following:

1. Charge transfer polarisation η_D: As explained in the previous section, the exchange of electrical charges between electrode and electrolyte gives rise to a voltage between them. An electric charge passing from one part of the system to another experiences a potential change called charge transfer polarisation. The Butler-Volmer equation (Eq. 4) gives the relationship between the current measured and the charge transfer polarisation.

$$i = i_c + i_a = i_o \left[\exp\left(\frac{\alpha z F}{RT} \eta_D \right) - \exp\left(- \frac{(1-\alpha) z F}{RT} \eta_D \right) \right] \qquad \text{Eq. 4}$$

---

[1] a note on the difference between polarisation and overvoltage: According to Vetter [92] overvoltage is the difference between the potential of an electrode supporting an electric current and the equilibrium potential if only one electrode reaction takes place. If two or more reactions take place at the electrode this difference is called polarisation.

Here α is the symmetry factor, z the number of electrons involved in the electrode reaction, F the Faraday constant, R the universal gas constant and T the absolute temperature of the electrode. The total current is the sum of the cathodic and anodic currents already defined in the previous section. Figure 6.3 shows the hypothetical anodic, cathodic and the resulting external current in the corroding metal surrounded by a chlorine-rich environment as a function of the voltage applied between electrode and electrolyte. For positive polarisations the anodic reaction will be accelerated, the anodic current will increase and the cathodic current will decrease – and vice versa for negative polarisations.

Because anodic and cathodic currents out of equilibrium have different values a net resulting current can be measured as can be seen in Figure 6.3. For high polarisations ($|\eta_D| >> RT/(zF)$) the charge transfer polarisation may be approximated by

$$\eta_D = \beta \cdot \log \frac{i}{i_o}, \qquad \text{Eq. 5}$$

where β is a coefficient of proportionality (see [93]). According to [48], the dependence of the external current on polarisation for low polarisations ($|\eta_D| << RT/(zF)$) can be approximated by equation Eq. 6.

$$i = \frac{zF}{RT} \cdot i_o \cdot \eta_D \qquad \text{Eq. 6}$$

$$\boxed{\eta_D = \frac{RT}{zFi_o} \cdot i \cdot} \qquad \text{Eq. 7}$$

The charge transfer resistance R_D can be defined as

$$R_D = \frac{1}{A}\left(\frac{d\eta_D}{di}\right)_{i=0} = \frac{RT}{zFA}\frac{1}{i_o} \quad [\Omega], \qquad \text{Eq. 8}$$

where A is the electrode's active surface area and i as well as i_0 refer to the current densities corresponding to the currents defined above. In the following, i and i_0 will be used for current densities unless otherwise stated.

2. Diffusion polarisation η_d: This form of polarisation arises when the transport of chemical species for the electrochemical reaction is slower than the reaction rate so that the reactant species cannot reach the surface fast enough and product species cannot leave the surface fast enough to uphold the initial reaction rate. According to [91] diffusion polarisation can be calculated as

$$\boxed{\eta_d = \frac{RT}{zF}\sum_j \nu_j \ln\left(1 - \frac{i}{i_{max}}\right)} \qquad \text{Eq. 9}$$

Where i_{max} is the maximum external current that is asymptotically approached when the transport of reactants and products gets much faster than the electrochemical reaction and ν_i are the chemical activities of the different species involved.

3. Reaction polarisation η_r: If the availability of cations and anions for the electrochemical reaction depends on other chemical reactions with different kinetics to the electrochemical reaction an additional potential drop is observed. This potential drop is called reaction polarisation and is defined as:

$$\boxed{\eta_r = \frac{RT}{zF}\sum_j \nu_j \ln\left(\frac{a_j}{\bar{a}}\right)} \qquad \text{Eq. 10}$$

Where a_j are the reaction activities of the species involved.

In the literature, the sum of diffusion and reaction polarisation is usually called concentration polarisation.

4. Crystallisation polarisation η_c: This type of polarisation is defined as the change in potential that results from reaction products adsorbed on the metal's surface entering the electrode's crystal lattice or being released from it. The kinetics of crystallisation may be handled like a chemical reaction (according to [94]) and therefore its dependence on the current may be described in the same terms as the reaction polarisation described above:

$$\boxed{\eta_c = -\frac{RT}{zF}\ln\frac{a_{m_j}}{\bar{a}_m}},$$ Eq. 11

where a_{m_j} are the crystallisation activities of the species involved and $\bar{a}_m$ is the average crystallisation activity.

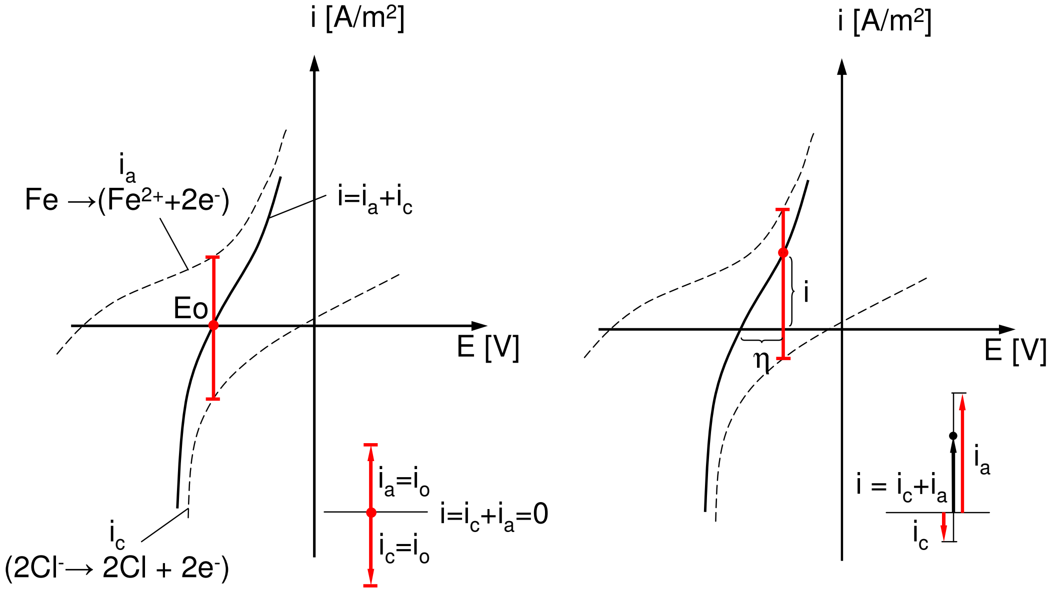

Figure 6.3: Example of anodic, cathodic and resulting current as a function of the charge transfer polarisation

5. Polarisation due to the electrolyte's ohmic resistance η_Ω: The resistance of the electrolyte R_Ω is a function of its conductivity for ions and electrons. If the current is very strong or the conductivity is too low, a significant potential drop in the electrolyte can result. In the experiments described below, this effect influences the polarisation resistance measurements and cannot be neglected.

$$\boxed{\eta_\Omega = R_\Omega \cdot I}$$ Eq. 12

For low polarisations and small currents, all but one of these types of polarisation become insignificant and so to good approximation the charge transfer polarisation is equal to the total polarisation (see [48]).

$$\eta\big|_{i\rightarrow 0} = \eta_D + \eta_d + \eta_r + \eta_c + \eta_\Omega = \eta_D = \frac{RT}{zFi_o}\cdot i$$

$$\boxed{\frac{d\eta}{di} = \frac{RT}{zFi_o}}$$ Eq. 13

Eq. 13 shows that under these conditions there is a linear relationship between the voltage applied and the resulting current. The slope of the applied voltage as a function of the net current is the charge transfer resistance and is inversely proportional to the corrosion current i_o. Based on this result, current-potential curves have been used widely in order to study the corrosion of materials in different areas of research.

As in [21], the signal from the LPR sensor will be expressed in terms of linear polarisation conductance (LPC) in the following. The polarisation conductance is defined as the inverse of the polarisation resistance, that is, the slope of the current vs. potential curve. For low polarisations and according to the equations mentioned above, this variable is directly proportional to the corrosion current i_o in the electrochemical system under consideration. The next equation described this proportionality in terms of the external current I and the current density i_0 corresponding to the corrosion current.

$$G \equiv \text{Polarisation conductance}$$

$$G = \left(\frac{dI}{d\eta}\right)_{i\rightarrow 0} = \frac{zFA}{RT} i_o \quad \left[\frac{1}{\Omega}\right] = \left[\frac{A}{V}\right]$$ Eq. 14

The corrosion rate r defined as loss in metal thickness per unit time is calculated according to equation Eq. 15 (here i_0 is a current density):

$$r \equiv \frac{dh}{dt} = \frac{i_o M}{zF\rho} = G\cdot\frac{RTM}{(zF)^2 A\rho} = G\cdot b\left[\frac{m}{s}\right]$$ Eq. 15

$$b \equiv \frac{RTM}{(zF)^2 A\rho} \quad \left[\frac{Vm}{As}\right]$$ Eq. 16

$$h(t) = \int_{t=0}^{t=t_{ex}} G\cdot b\,dt$$ Eq. 17

Here M is the molar mass of the material, ρ is its density, R the universal gas constant, F the Faraday constant, z the number of electrons involved, T the absolute temperature, A the active surface area for this reaction and h the metal's loss in thickness. b is the so called calibration factor and has a theoretical value of $5 \cdot 10^{-10}$ Vm/(As) for an electrode of pure iron with an active surface area of 20 cm^2. In practice the calibration factor for an experiment is calculated from the metal loss of the electrode.

6.1.3 Polarisation measurements

A typical set-up for the experimental study of metal corrosion in liquid solutions by measuring polarisation is shown in Figure 6.4

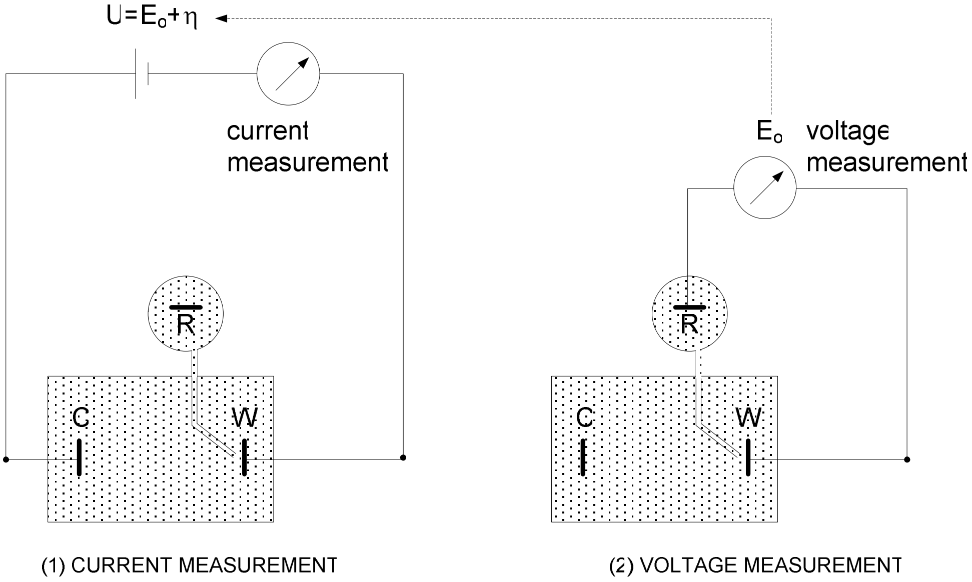

Figure 6.4: Circuitry for the measurement of current-voltage plots (potentiostatic)

If an external voltage is applied directly the set-up is called potentiostatic. If a high voltage is applied to the system in series with a strong resistor so as to keep a close-to-constant current, the set-up is called galvanostatic. In the following only the potentiostatic set-up will be described since it is the most widely used and the only one required for this work. Figure 6.4 shows the three electrodes used: the working electrode consisting of the corroding metal (W), the counter electrode (C) and the reference electrode (R). The external current I and the free corrosion potential E_o cannot be measured simultaneously.

As already explained the external current can only be measured once the system is polarised, whereas the free corrosion potential can only be measured with the system in equilibrium (see 6.1.2). Therefore the measurement is divided into two steps: first the system is polarised for a certain period of time to measure I (between W and C), then the polarisation is discontinued until the system reaches its equilibrium and E_o can be measured (as the potential difference between W and R).

In Figure 6.4 the circuit on the left represents the set-up during polarisation. An external voltage U is applied on the metal of study between the working and counter electrodes. Then the external current I is measured. The circuit on the right of Figure 6.4 shows the set-up for the measurement of the free corrosion potential. The power supply is switched off and the free corrosion potential E_o is measured once equilibrium has settled in. The applied voltage during polarisation is calculated as $U = E_o + \eta$, where η is the polarisation of interest for the measurement. Figure 6.5 shows schematically the measuring procedure for obtaining one point G_j of the LPC signal:

If a voltage U_1 is applied to the system, this system is polarised by a certain value η_1 and the resulting current I_1 is measured. Then polarisation is interrupted and the system returns to its equilibrium, upon which the free corrosion potential $E_{o,2}$ is measured. The system is polarised again, this time applying a new polarisation η_2. The resulting voltage of the system is $U_2 = E_{o,2} + \eta_2$. The new external current I_2 is then measured. Polarisation is interrupted and the system returns to equilibrium. $E_{o,3}$ is measured. The system is polarised applying $U_3 = E_{o,3} + \eta_3$ and so on. The points $P_1(U_1,I_1)$, $P_2(U_2, I_2)$ and $P_3(U_3, I_3)$ are displayed in a U-I diagram. The slope of the curve thus obtained is the first value of the LPC signal. The duration of polarisation and equilibrium periods, the number of points P_i and the polarisation are inputs of the measuring process. The larger the number of points P_i and the wider the polarisation limits ($+h_2$,$-h_3$) are, the easier it is to accurately determine the slope of the curve. Maximum and minimum polarisations are however limited by the stipulation $|\eta_D| << RT/(zF)$ as mentioned in Eq. 6, so that a linear dependence of I on U can be assumed. This procedure is repeated for each value G_j of the LPC signal. Using the calibration factor b the LPC signal G vs. t is transformed into a corrosion signal r vs. t (t = exposure time).

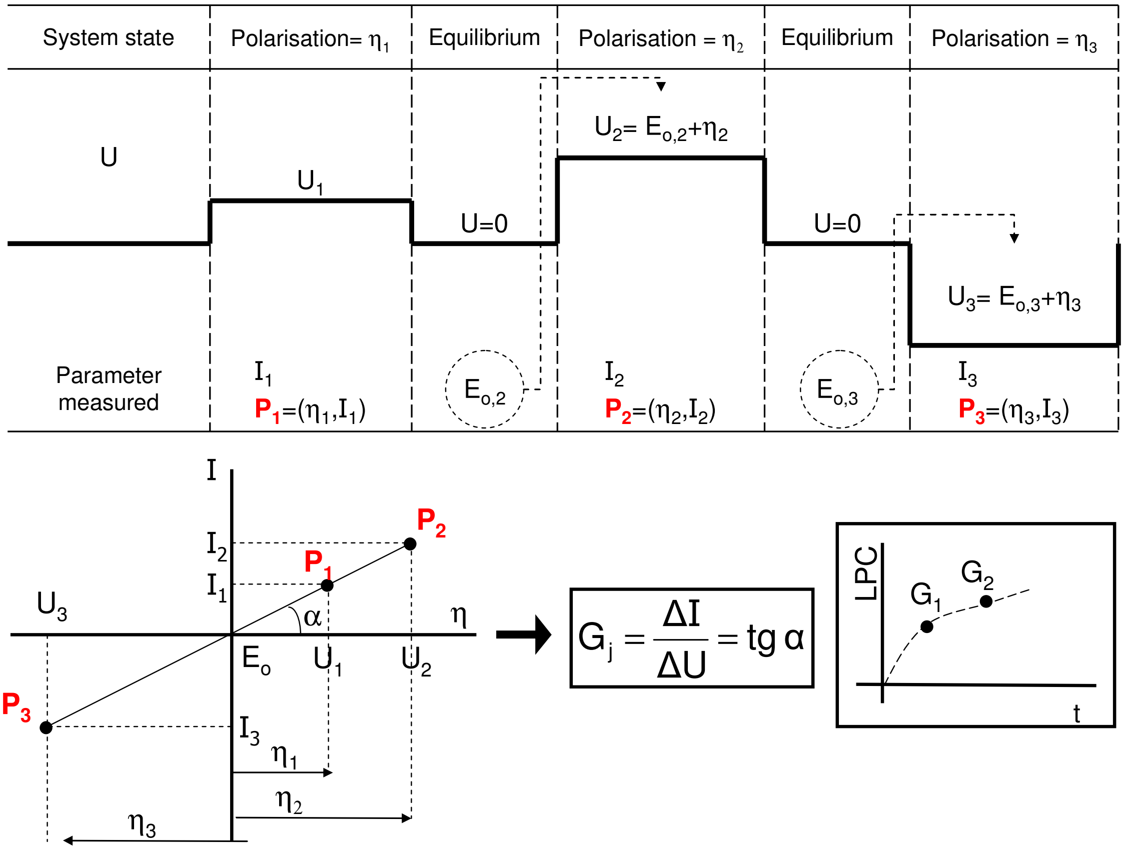

Figure 6.5: Measuring procedure for the LPR measurements

6.1.4 Ohmic resistance of the electrolyte

In the following section an ideal power plant, in which the flue gases provide constant corrosion conditions shall be considered. If the electrodes of the LPR sensor are exposed to these flue gases, the corrosion signal predicted by the corrosion kinetics described in section 2.1.2 is shown in Figure 6.6. In the beginning the corrosion reaction is not inhibited and metal loss per unit time is high. Later the corrosion products and/or particle fouling on the electrodes inhibit the corrosion reaction so that the corrosion rate decreases. Once the corrosion process on the electrode reaches equilibrium the corrosion rate becomes constant. The corrosion signal obtained experimentally in previous series of measurements with the LPR sensor is also shown in Figure 6.6.

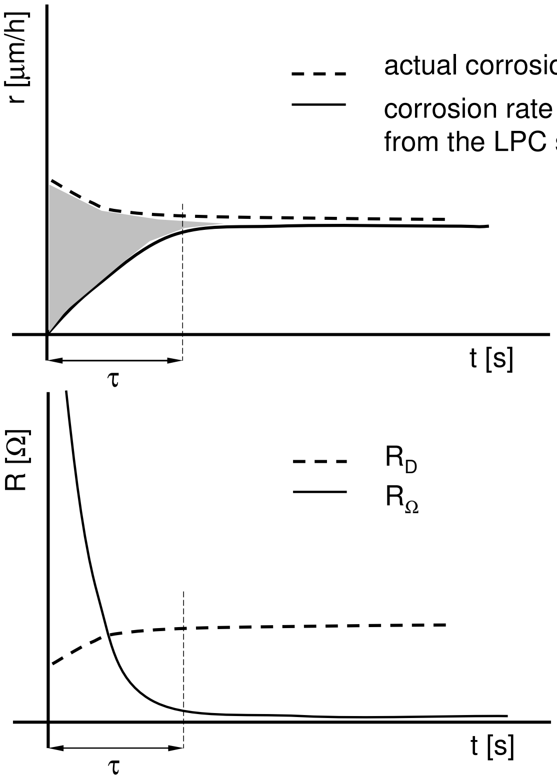

Figure 6.6: Comparison of the actual corrosion rate with the corrosion rate inferred from the LPC signal

The LPC signal always starts at zero and increases gradually to a constant value after a certain period of time. τ is defined as the time required for the LPR sensor to produce a signal corresponding to the actual corrosion rate (within a small error margin). It can be observed that for short times ($t < \tau$) the behaviour of the measured corrosion signal does not agree with theoretical predictions and the LPC signal is assumed to underestimate the actual corrosion rate. In this work it is postulated that the main cause for this underestimation is the electrolyte's ohmic resistance already described in section 6.1.2.

During polarisation measurements in liquid solutions it is the mobility of ions that enables the exchange of charges (positive or negative) between the anodic and cathodic zones, thus closing the electric circuit. The high conductivity of the liquid solution means that the ohmic potential drop through the electrolyte, called electrolyte resistance, is much lower than the polarisation measured and can be neglected. In the case of the high-temperature corrosion sensor used here, the electrodes (rings) are not submerged in a liquid solution but exposed to a flow of flue gas with a very low conductivity. The electrical circuit is closed by the layer of corrosion products on the rings. An external current can only be measured if this layer is thick enough. For $t = 0$ no corrosion products are present and the resistance of the electrolyte is very high. Conditions are similar to those of an open circuit. After a certain exposure time τ some corrosion products have accumulated on the ring and the resistance of the electrolyte decreases. For the first stages of corrosion ($t < \tau$) the resistance of the electrolyte is responsible for a potential drop at least in the same order of magnitude as the polarisation measured or even much higher and therefore cannot be neglected.

In this work the short-term behaviour of the LPR sensor was studied. The following questions were addressed:

- Is it possible to measure a reasonable LPR signal during short-term combustion of biomass and doped biomass in a small-scale plant?
- What information does the LPR sensor supply on the corrosion progress during short-term tests? Can the influence of the electrolyte’s resistance be identified?
- Can the influence of different combustion parameters on corrosion be studied?
- How long is the time τ for these tests?

6.2 Linear polarisation resistance sensor

In the last decades sensors designed ad hoc have been developed for the measurement of high-temperature chlorine-induced corrosion of metals. In the following, the sensor developed and manufactured by Corrmoran GmbH [21, 95] and used exclusively in this work will be described.

The sensor consists of a cylindrical head ($d = 35$ mm) with four metal rings ($l = 10$ mm) electrically insulated from each other by means of ceramic rings inserted between them as shown in Figure 6.7. The metal rings form a four-electrode set-up with working, counter and reference electrode and an additional fourth electrode for mass loss measurements. This ring is weighed before and after the exposure in order to obtain the mass loss necessary for the calculation of the calibration factor b. This ring, the working electrode and the counter electrode are all made of the metal relevant for the study. The reference electrode is made of a high-temperature corrosion-resistant material, in this case Inconel© 625. The probe head is cooled with pressurised air. For power plant applications the container tube with a length of 2 to 3 metres is additionally cooled with water.

The free corrosion potential is measured between working and reference electrode. The external DC voltage U (potentiostatic approach) is applied between working and counter electrodes. U is varied gradually from $E_o - \eta$ to $E_o + \eta$ and from $E_o + \eta$ back to $E_o - \eta$. The resulting current I is measured. Assuming that in this case only one electrode reaction takes place, η is called polarisation. The polarisation conductance is calculated as the gradient of the curve I vs. η. Its units are milliampères per volt (mA/V). “LPC up” is the gradient of the curve from $E_o - \eta$ to $E_o + \eta$ and “LPC down” is the curve from $E_o + \eta$ to $E_o - \eta$. The LPC signal obtained assumes one “LPC up” value and one “LPC down” value alternately. As already mentioned, for low values of polarisation LPC values are proportional to the corrosion rate. The proportionality constant (called calibration factor) b is calculated from the weight loss of the fourth ring. Calibration factors measured over long measuring periods (~ 2 months) in different EfW plants with this sensor all have values around $1\cdot10^{-8}$ Vm/As [21, 96].

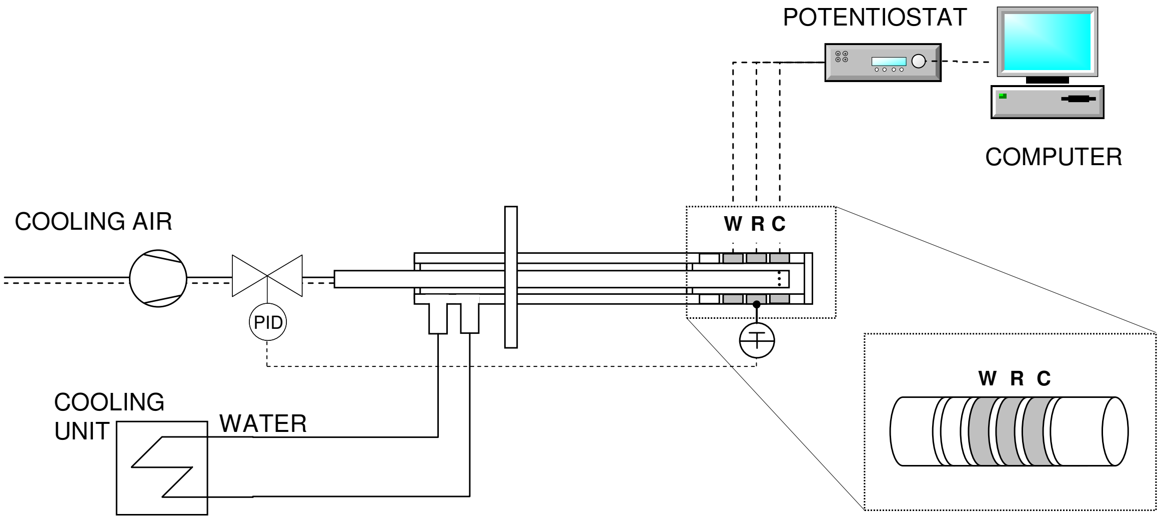

Figure 6.7: Measuring set-up for the LPR sensor

The measuring set-up used for the small-scale tests is sketched in Figure 6.7. The potentiostat fulfils the following tasks: (1) it measures the free corrosion potential between working and reference electrode, (2) it applies a polarisation η (±0.5 V) between working and counter electrode and (3) it measures the resulting current between working and counter electrode. A computer processes the values for polarisation and resulting current and calculates the polarisation conductance (in mA/V) which is proportional to the corrosion rate according to the theory explained in 6.1.2. Due to the small size of the facility used for these tests, the tube supporting the sensor head in power plant applications was omitted and only the sensor head (d = 35 mm, l ~ 100 mm) was used. The sensor was introduced in position B of the reactor (see Figure 3.3). Without the supporting tube no water cooling was needed. The sensor head was cooled with pressurised air and the temperature regulated by means of a PID controller. The temperature of the sensor selected for these tests was 430 °C. The temperature of the rings was measured by a thermocouple attached to the inner side of the reference ring. After exposure to the flue gases the sensor was disassembled and the rings were analysed in a laboratory.

6.3 Test parameters

The test matrix is shown in Table 6.1. The fuels used for these tests were rye straw, wood and $ZnCl_2$-doped wood pellets (WP0.1% and WP0.5%). The tube temperature was 430 °C and the flue gas temperature about 800 °C. Working and counter electrode rings were made of 16Mo3 steel (this is the new nomenclature according to DIN EN 10028-2 [97]; the material was formerly denoted 15Mo3 according to DIN 17155). This is a material commonly used in the superheaters of EfW plants. Its composition is detailed in Table 4.1.

Table 6.1: Test matrix for the LPR measurements

Run #	fuel	ring set	combustion time (h)	comments
1	RSP	1	7.2	
2	RSP	3	5.5*	
3	WP0.5%	4	8.3	
4	WP0.5%	4	7.7	deposits from previous run
5	WP0.5%	4	7.8	deposits from previous run
6	WP0.5%	4	8.6	deposits from previous run
7	WP	4	8.1	deposits from previous run
8	WP	4	8.3	deposits from previous run
9	RSP	4	4.5*	deposits from previous run
10	WP0.1%	2	30.5	

*defluidisation

6.4 Results

First series of measurements

During the first series of measurements, combustion tests with an exposure time of 8 hours were carried out and the LPC signal was measured. In order to obtain high corrosion rates, fuels with a high chlorine content were selected: straw pellets (RSP) and wood pellets doped with $ZnCl_2$ (WP0.5%). The rings were changed after every run so that the remaining corrosion products from one test do not affect the next one. The results of the first run (run 1) are shown in Figure 6.8. In this run RSP pellets were used as fuel. The graph of the LPC signal is similar to that shown in Figure 6.6 for $t < \tau$. The signal starts at zero and increases continuously to approximately 0.015 mA/V after 8 hours of exposure.

The test was repeated (run 2) with new rings and values in the same order of magnitude were obtained. Figure 6.9 shows the LPC signal measured during run 2. Again the signal increases continuously and reaches a value of about 0.010 mA/V after approximately 6 hours of exposure. It can be concluded that the LPC signals obtained in these tests are reproducible.

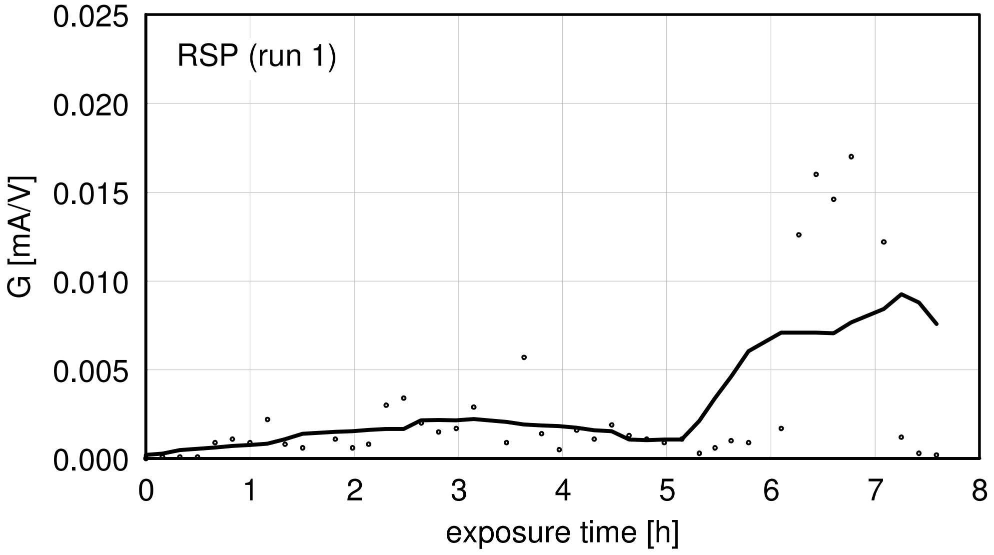

Figure 6.8: LPC signal in run 1 (fuel: RSP; T_{tube} = 430 °C; $T_{flue\ gas}$ ~ 750 °C)

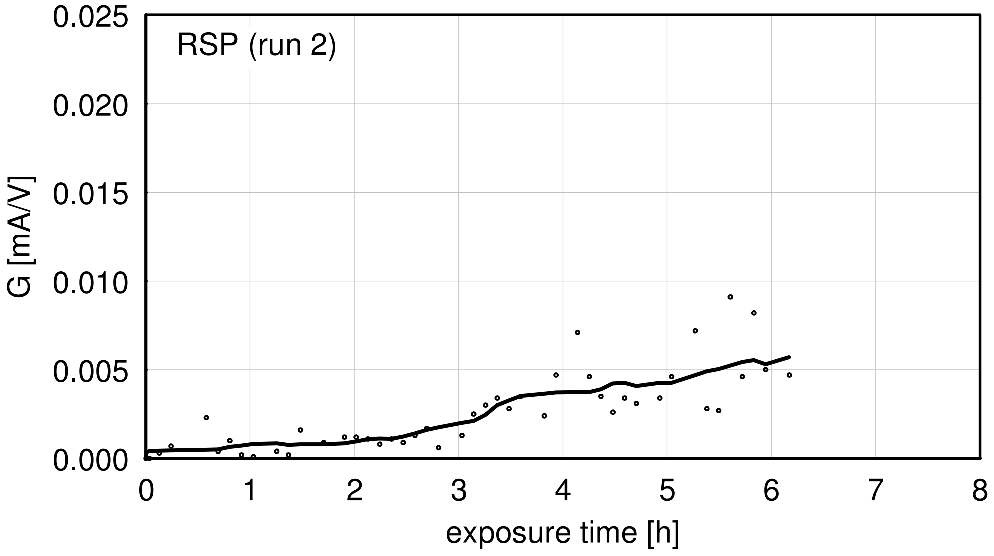

Figure 6.9: LPC signal in run 2 (fuel: RSP; T_{tube} = 430 °C; $T_{flue\ gas}$ ~ 750 °C)

It can be seen that the signals do not reach a stationary value within the 8 hours of exposure. They increase continuously until the end of the experiment. Steadily increasing values for G in the measured LPC signals may indicate that τ (the time that the signal needs to become stationary, see the definition in section 6.1.4) has not been reached.

According to this interpretation, 8 hours of exposure are not enough to measure the corrosion rate of the electrodes in this kind of test.

In run 3 the fuel was changed to WP0.5% (wood pellets doped with $ZnCl_2$). Figure 6.10 shows the LPC signal obtained. The graph and the final value of the signal are similar to those of run 1. G values start at zero and increase steadily up to 0.015 mA/V after 8 hours of exposure. This fuel has lower chlorine and alkali contents than RSP and therefore lower G values were expected.

For a better understanding of the results obtained, the LPC signals from these small-scale experiments are compared with those obtained in real power plants. A large number of LPC signals measured with the same sensor in different EfW plants are found in the work of Waldmann [21]. According to Waldmann the LPC signal typically reaches a stationary value around 5 mA/V in plants with low corrosion; in plants with high corrosion the LPC signal comes to rest at about 100 mA/V. The time for the signal to reach a stationary value is in the order of magnitude of some hundreds of hours (typically 1 week ≈ 150 h). This means that the slope of the curve during the non-stationary phase is about 0.03 - 0.6 mA/V per hour. The LPC values obtained in runs 1, 2 and 3 with an increase of 0.001 mA/V per hour are more than a hundred times smaller than the lowest value obtained in a power plant. It must be taken into account that stationary conditions have not been reached.

These low G values may be the result of a very high ohmic resistance R_Ω of the electrolyte. As already mentioned in section 6.1.4, R_Ω may have the same order of magnitude (or even higher) as R_D for $t < \tau$ and therefore could not be neglected in such a case. If R_Ω cannot be neglected, the LPC signal cannot be assumed to be proportional to the corrosion rate. This would explain why the signals in runs 1 and 3 are so similar although different corrosion rates are expected. During the 8 hours of exposure the corrosion products on the rings are insufficient to constitute a high-conductivity electrolyte. The linear polarisation resistance measured consists mainly of the electrolyte’s ohmic resistance. The higher the polarisation resistance is, the lower the LPC values ($G = 1/\text{resistance}$) are. This would explain the low LPC values obtained. This effect will be studied quantitatively in section 6.5.1.

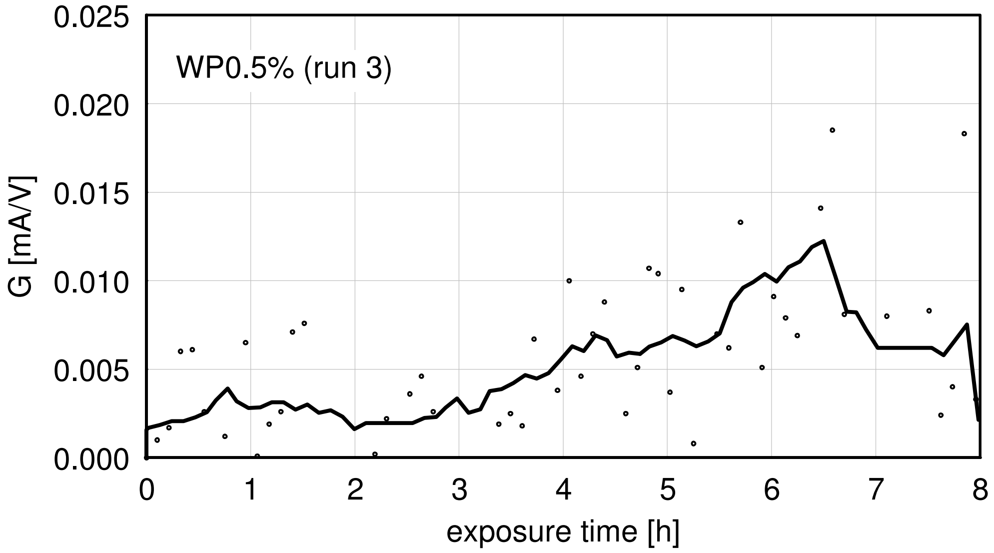

Figure 6.10: LPC signal in run 3 (fuel: WP0.5%; T_{tube} = 430 °C; $T_{flue\ gas}$ ~ 750 °C)

Second series of measurements

For the second series of measurements the exposure time was increased to about 30 hours. Two different approaches were tested. In the first one (runs 3 to 6) the same rings were exposed to the flue gases of the facility for 8 h per day for four consecutive days (total exposure time: 32 hours). The facility was shut down at night. The fuel used was wood doped with $ZnCl_2$ (WP0.5%). In the second approach the rings were exposed to the flue gases continuously for 30 hours (run 10). For availability reasons the fuel used in this test was WP0.1%. An exposure time of 30 hours implies a total test duration of at least 38 hours (preheating the facility takes about 3 hours cooling it down another 5 hours). The duration of such tests is limited by the fact that the reactor does not operate automatically and must be monitored continuously. For this reason 37 hours of uninterrupted operation come at a great cost in terms of personnel and equipment.

Figure 6.11 shows the results of the four consecutive runs carried out with WP0.5%. It is important to note the different scaling of the Y-axis compared to the previous figures. The shape of the LPC signal is similar to that in Figure 6.6 for $t < \tau$. No stationary value is reached. The LPC signal starts at zero and increases to a certain G value. For each new test the signal always starts at zero and increases to a new G value. The final G value at the end of each run is higher for each new test. It increases by circa 0.03 mA/V per day reaching a value of approximately 0.10 mA/V after 32 hours of exposure. This increase in the measured G values may indicate that the electrolyte layer is growing with each run, resulting in a decrease of the electrolyte's ohmic resistance. This gives rise to an increasing LPC signal.

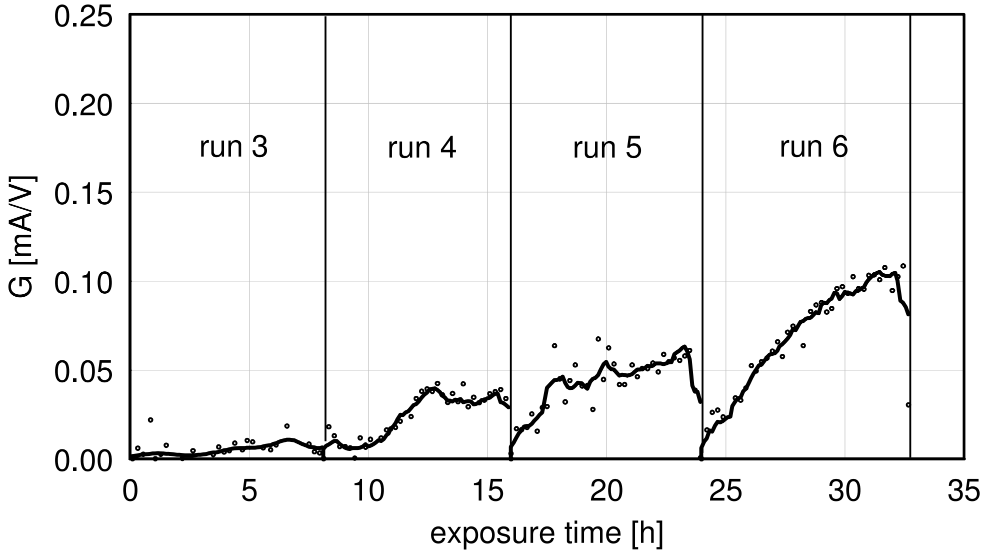

Figure 6.11: LPC signal in runs 3 to 6 (fuel: WP0.5%; T_{tube} = 430 °C; $T_{flue\ gas}$ ~ 750 °C)

Figure 6.12 shows one possible interpretation of the results according to section 6.1.4. In the figure a new characteristic time τ' is observed. At the beginning of each run the signal has a certain slope steeper than the slope at the beginning of the previous experiment. After a certain time (approximately 2 hours) the curve shows a reduced curvature and the slope follows the tendency observed at the end of the previous run. The interpretation of this behaviour goes beyond the scope of this work but could be relevant for a more detailed analysis of the sensor's operation.

In order to determine the corrosion rate of the electrode, further tests should be carried out until a stationary signal is reached. However, it must be taken into account that the exposure of the rings to the hot flue gases was interrupted at night for these tests. The influence of cooling down and heating up the rings between the runs is not known and could affect the corrosion rates measured.

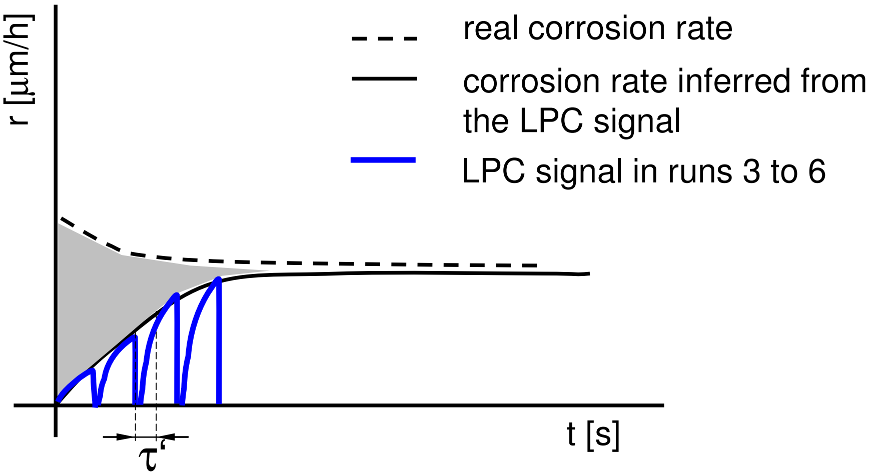

Figure 6.12: Interpretation of the LPC signal in runs 3 to 6

Figure 6.13 shows the LPC signal obtained during the uninterrupted test lasting 30 h (run 10). In this case the signal seems to reach a stationary value after the first 12 hours of exposure[2]. This may indicate that τ may have been reached and that the LPC value measured at the end of the tests may be proportional to the actual corrosion rate. Apparently the electrolyte has formed much more quickly in this run. If the LPC signal in this test is compared with those from the previous tests (Figure 6.8 to Figure 6.10) it can be seen that the values in this test are about one order of magnitude higher. A G value of 0.1 mA/V is already reached after 8 hours of exposure. The fuel used in this run has lower chlorine and alkali contents than the fuels used in the previous tests (see Table 3.3). Fuel composition can therefore not explain a faster formation of corrosion products. The electrolyte layer may be affected by parameters not considered during these tests (e.g. solid particles in the flue gas). In future measurements this behaviour should be investigated in more detail.

---

[2] The absence of data for the first 2 hours of exposure observed in this run is due to a technical problem with the potentiostat.

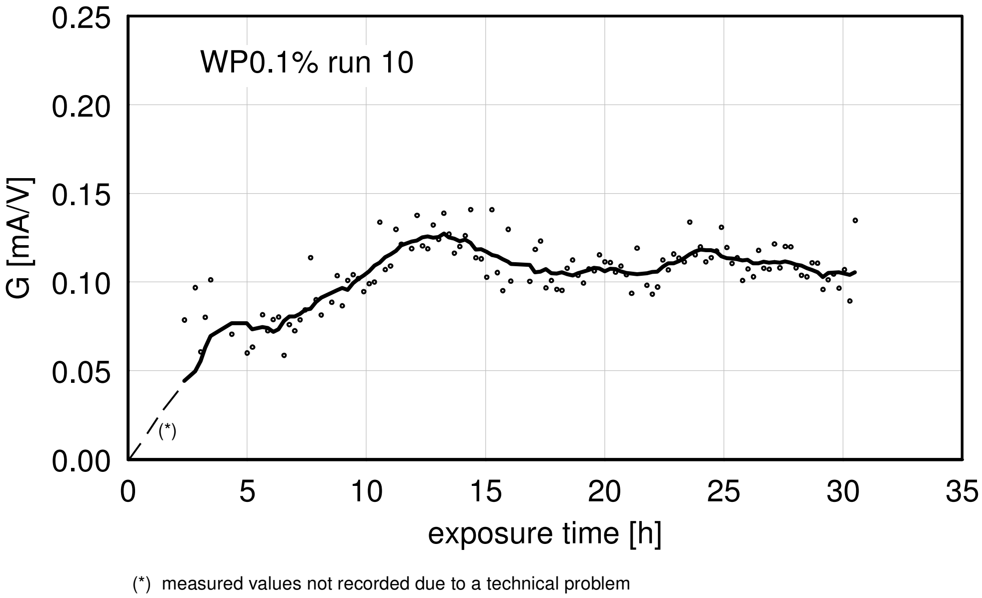

Figure 6.13: LPC signal in run 10 (fuel: WP0.1%; T_{fuel} = 430 °C; $T_{flue\ gas}$ ~ 750 °C)

6.4.1 Sensitivity of the LPC signal to the temperature of the flue gas

One of the most significant results of all these experiments is the fact that the LPC signal reacts very quickly to changes in the temperature of the flue gas. In all the experiments (without exception) the signal is zero during the preheating of the facility, starts to increase as soon as fuel feeding begins and drops sharply to zero once fuel feeding is stopped. Figure 6.14 shows the LPC signal in one of the runs to illustrate this.

As can be seen in Figure 6.14 no G values are displayed before and after combustion, although the measurement of the LPC signal was started long before the preheating of the facility and stopped long after the facility had cooled down. The missing values are due to the way the sensor is programmed. In order to save disk space during long series of measurements, the computer programme responsible for the calculation of G values only records values different from zero (the algorithm with which the computer calculates the G values from the measured values of I and U was already explained in section 6.1.3). Zero values are thus not recorded in the measurement files and are therefore not displayed. Accordingly (as can be seen in Figure 6.14) G values are only different from zero as long as combustion takes place in the reactor. This behaviour is also observed during the start-up of runs 4 to 6, in which the rings were already covered with deposits and corrosion products from previous experiments. The first non-zero value during facility start-up is recorded immediately after the combustion begins. The last non-zero value is recorded approximately 5 min after combustion ends. As explained in section 2.1.1 and as is usually the case for chemical reactions, temperature plays an important role in the rate of the corrosion reaction. The influence of temperature should therefore not be neglected.

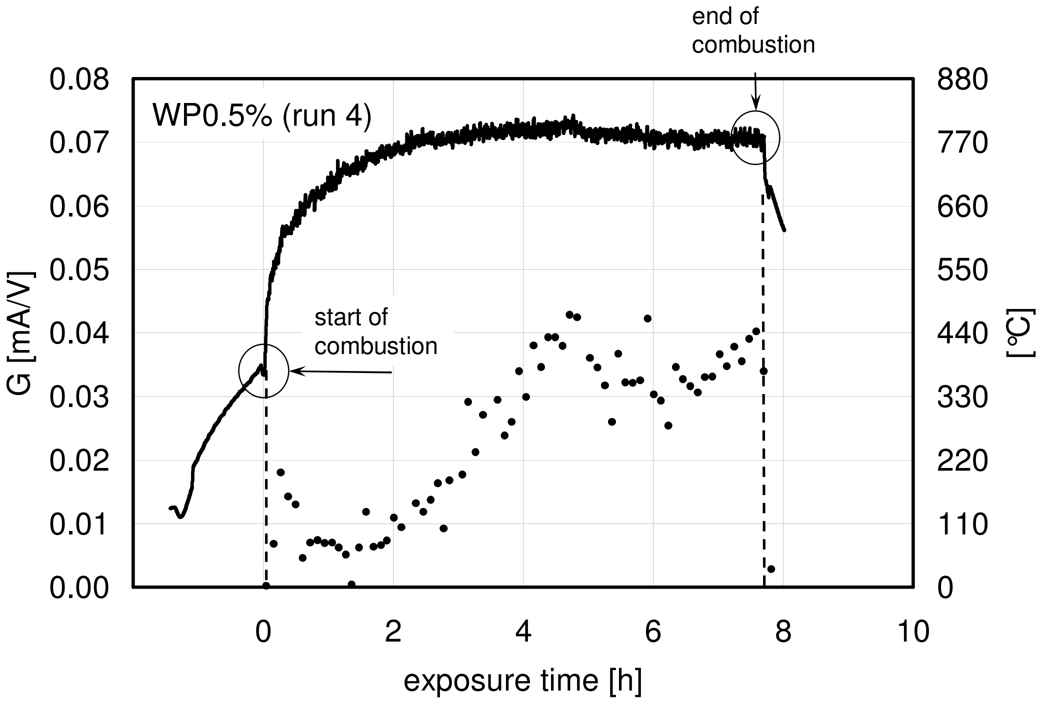

Figure 6.14: LPC signal vs. flue gas temperature

The presence or absence of corrosion products on the rings (new or reused ring) does not affect the observed behaviour. According to this it may be concluded that even if corrosive species already cover the electrode, the additional supply of corrosive species by the flue gas at a certain temperature are necessary for the corrosion reaction to continue. This result agrees well with the results presented in [98], in which it was demonstrated that the deposits and corrosion products alone are not able to sustain the corrosion reaction if the flow of flue gas is interrupted, even if the temperature of the environment is kept the same.

6.4.2 Sensitivity of the LPC signal to different fuels

During the third series of measurements the reaction of the LPC signal to different flue gas compositions was tested. Therefore three runs with fuels different to WP0.5% were carried out (runs 7 to 9). It was decided to use the same rings already covered with deposits and corrosion products from the previous 32-hour experiment for all these runs and to keep these rings in use until the end of run 9. As seen in the previous tests, the presence of a certain amount of electrolyte on the rings is crucial for the measurements to allow inference of corrosion rates. First a less corrosive flue gas was tested. During the first two runs wood pellets (WP) were burnt. Wood pellets have very low chlorine and alkali contents, so flue gas has a very low concentration of corrosive species. The LPC signal obtained during these runs can be seen in Figure 6.15 and Figure 6.16. The signal shows a very high peak during the first 4 hours and finally decreases to a constant value of about 0.1 mA/V.

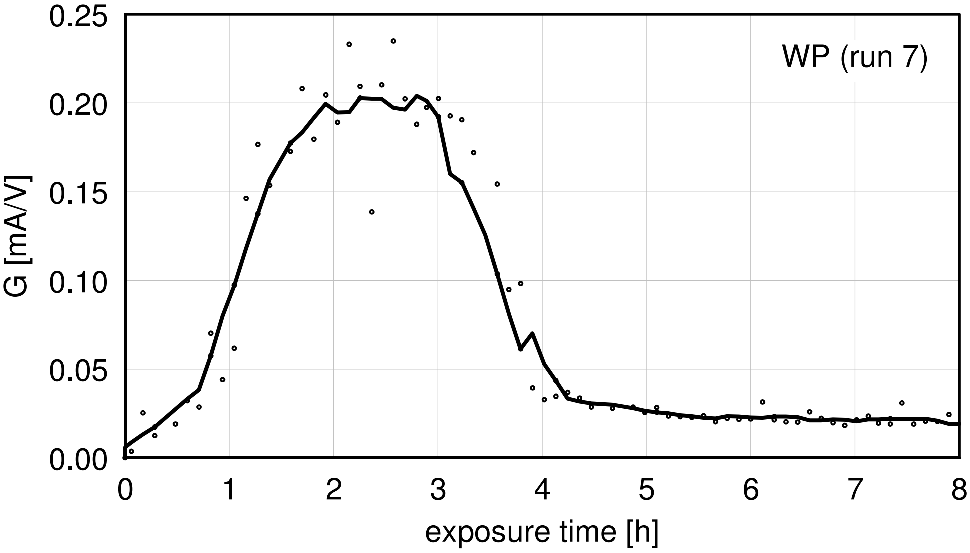

Figure 6.15: LPC signal in run 7 (fuel: WP; T_{tube} = 430 °C; $T_{flue\ gas}$ ~ 750 °C)

The repetition of the run yielded the same constant value, this time without a pronounced peak. Figure 6.16 shows the LPC signal obtained. Since the same stationary value of G is obtained, it can be assumed that stationary conditions have been reached and the last LPC signal is proportional to the corrosion rate of the electrodes. The constant value is about ten times lower than the 0.1 mA/V obtained after 32 hours of exposure to WP0.5% (see

Figure 6.11). This agrees well with the low corrosion rates expected due to the fuel composition.

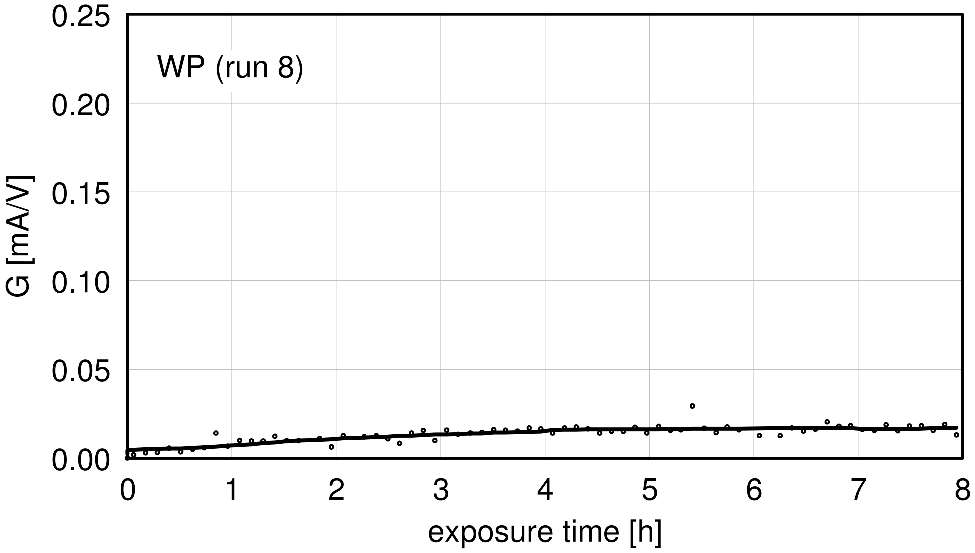

Figure 6.16: LPC signal in run 8 (fuel: WP; $T_{tube} = 430$ °C; $T_{flue\ gas} \sim 750$ °C)

The high peak obtained in the first run with wood pellets was not expected and was not observed in any other test. In order to make sense of it, the HCl measurement must be considered. The HCl concentration in the flue gas was measured online by means of a FTIR spectrometer. The HCl signal measured is shown in Figure 6.17 together with the LPC signal.

No HCl concentrations were measured during the first 4 hours of exposure. The HCl measurement started at t = 4.5 h and ended at t = 7.7 h. It can be seen that during this period the HCl content in the flue gas decreased from 40 to 10 ppmv (at 6% O_2). Since the Cl content in the WP is very low and the bed material had been changed before the test, it can be assumed that this high HCl content originates from the chlorides accumulated in parts of the reactor and/or in the layer of deposits and corrosion products formed on the rings during the previous tests. The test immediately preceding this one had been performed with a chlorine-rich fuel (WP0.5%). Using this fuel HCl values of about 80 ppmv were measured in the flue gas. This could explain the peak observed in the next LPC signal. The chlorides in the deposits and corrosion products are released when flue gas temperature reaches a certain value and they give rise to high G values. As explained in the previous section, chlorides from the deposits and corrosion products are not able to sustain the corrosion reaction. After a certain time, chlorides run out and the G values decrease to the value expected for the combustion of wood.

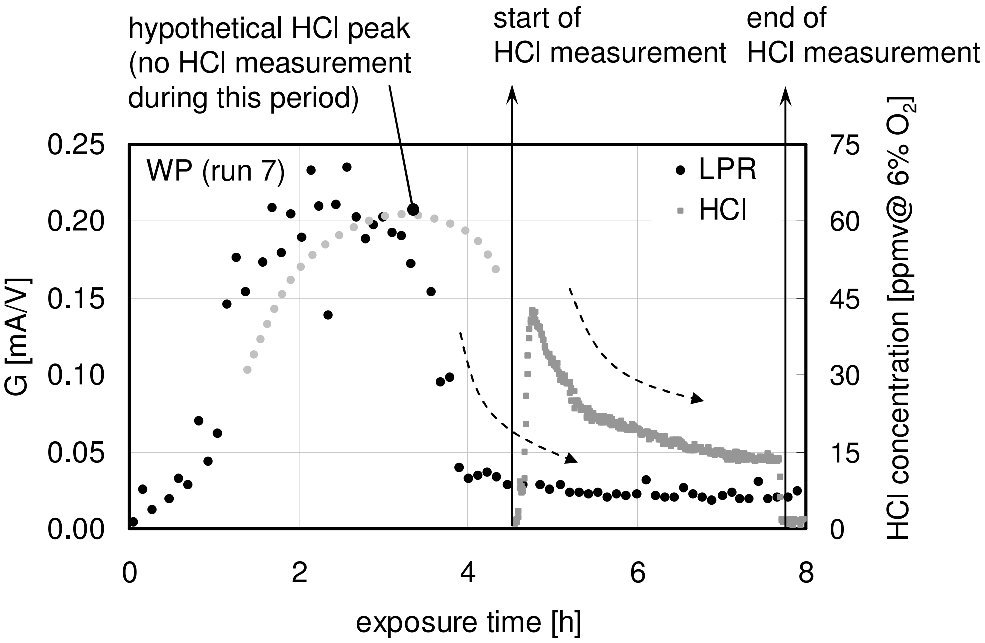

Figure 6.17: HCl in the flue gas and LPC signal in run 7 (fuel: WP; T_{tube} = 430 °C; $T_{flue\ gas}$ ~ 750 °C)

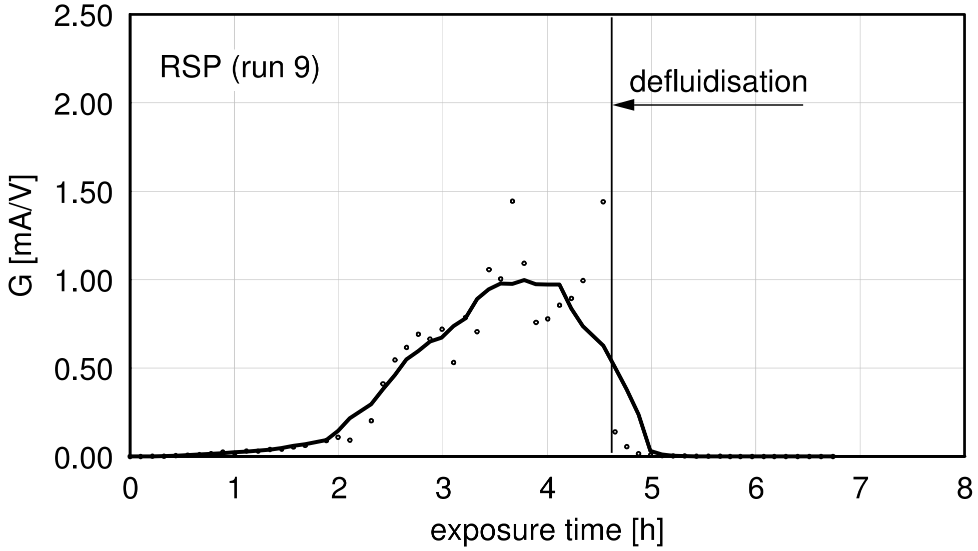

Figure 6.18: LPC signal in run 9 (fuel: RSP; T_{tube} = 430 °C; $T_{flue\ gas}$ ~ 750 °C)

After these two tests a run with a highly corrosive flue gas was carried out (run 9) using straw as fuel (RSP). Straw has the highest chlorine content of all the fuels available for this study. The LPC signal obtained is shown in Figure 6.18.

One should bear in mind the new scaling of the Y-axis. During this test G values of about 1.5 mA/V were obtained, more than hundred times higher than the values obtained for the same fuel during the first runs. As already explained, the electrolyte's ohmic resistance during the first tests may be too large to infer actual corrosion rates from the LPC signals. In this run the rings were already covered with an electrolyte layer from previous tests. The LPC signal for run 9 increases very sharply to values around 1.5 mA/V after only 4.5 hours of exposure. After this time the bed defluidised and the combustion had to be interrupted. The defluidisation of the bed was due to the agglomeration of the bed particles. Agglomeration will be studied in greater detail in a separate section.

6.4.3 Correlation of the LPC signal with metal loss

All the results of the LPR measurements so far have been presented in terms of conductance (G in mA/V) and not in terms of the corrosion rate (thickness loss/time). As explained in the previous sections, the LPC signals obtained do not always reach stationary values and are not always proportional to corrosion rates. The conversion of the G values into corrosion rates via Eq. 15 is therefore not always legitimate. It was therefore decided to work with the original values in mA/V for the comparison of the LPC signals.

For the conversion of these signals into corrosion rates the calibration factor b must be calculated using equation Eq. 17 in section 6.1.2. In practice the calibration factor is calculated as follows: The weight of the fourth ring is measured before and after exposure so that the thickness loss $\overline{h}$ for the given exposure time t_{ex} can be calculated. The LPC signal (G values) measured during this period of time is integrated from $t = 0$ to $t = t_{ex}$. The calibration factor b is then calculated according to equation Eq. 18:

$$b = \frac{\overline{h}}{\int_{t=0}^{t=t_{ex}} G\,dt} \quad \left[\frac{Vm}{As}\right] \qquad \text{Eq. 18}$$

As shown in section 4.3, the mass loss of the rings is very small and the weight loss measurements are subject to great uncertainties in this kind of test. Hence accurate calibration factors cannot be calculated.

Just to give a rough idea of the order of magnitude of the corrosion signal measured in this work an average calibration factor is used (b =10^{-8} Vm/As, $\sigma = 3.5\cdot10^{-9}$). It is the mean value of numerous calibration factors calculated by Haider *et al.* [96] for different EfW plants. It must be taken into account that the actual calibration factor for this test facility may differ substantially from the calibration factors calculated for EfW plants. Using the calibration factor the LPC signals can be converted into a corrosion rate r according to Eq. 19 (see Eq. 15 above):

$$r = G \cdot b \left[\frac{m}{s}\right] \qquad \text{Eq. 19}$$

In the field of high-temperature chlorine-induced corrosion of superheater tubes, the units [µm/h] and [mm/a] are more commonly used. Figure 6.19 gives an overview of the corrosion signals in the different corrosive environments studied in this section (runs 3 to 9).

In this figure it can be seen that the estimated corrosion rate depends on the presence or absence of corrosive species in the flue gas. The LPC signal used for the estimation of the corrosion rate was measured during the four consecutive tests with wood pellets doped with $ZnCl_2$ (WP0.5%), the two tests with wood (WP) and the test with straw (RSP). The figure shows the correlation. The individual LPC signals have already been explained in the previous sections. Stationary conditions only have been reached during the wood tests (after an exposure of about 40 hours). Before this time the corrosion rate is underestimated and therefore not considered here. The calculated corrosion rate for the wood tests is around 0.005 mm/a, for the straw tests 0.5 mm/a.

If the corrosion rate is integrated over the exposure time the metal loss of the rings is obtained. Figure 6.20 shows the metal loss calculated from the corrosion rate according to Eq. 17. The dashed lines represent the uncertainty of the measured values. It has to be taken into account that this diagram is just an estimation of the metal losses based on an average calibration factor. The aim is to estimate the order of magnitude of the metal losses predicted by the LPC signal. According to this diagram the thickness loss of the rings at the end of the total exposure time is estimated to be about 0.05 to 0.25 µm. Such small thickness losses explain the difficulties encountered during the metallographic tests.

The metal loss is more or less constant during the combustion of wood, since hardly any corrosion takes place. During the combustion of straw the metal loss increases sharply. The constant value at the end of the exposure time has to do with the reduction of the LPC signal due to the defluidisation of the bed.

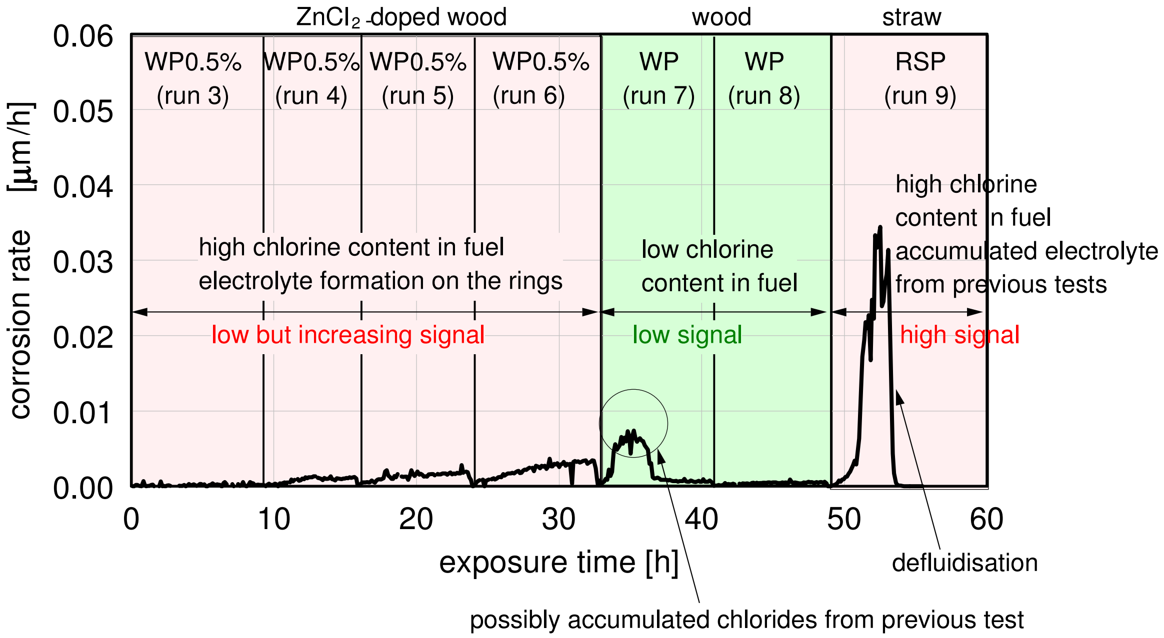

Figure 6.19: Influence of the fuel's chlorine content on the estimated corrosion rate (T_{tube} = 430 °C; $T_{flue\ gas}$ ~ 750 °C)

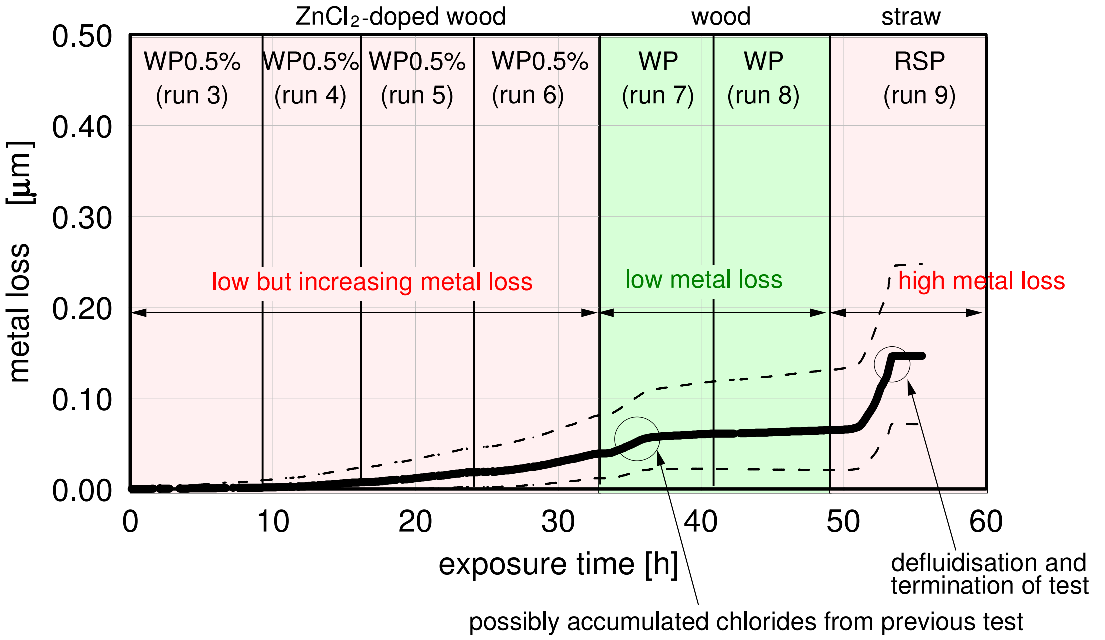

Figure 6.20: Influence of the fuel's chlorine content on the estimated metal loss (T_{tube} = 430 °C; $T_{flue\ gas}$ ~ 750 °C)

6.4.4 Error margins for the LPR measurements

The uncertainty for these measurements is calculated according to the DIN 1319 [87] standard. The uncertainty of the measurements has three sources:

- The first one is related to the reproducibility of the experiments. In Figure 6.8 and Figure 6.9 LPC signals for two experiments carried out under the same conditions are shown. An empirical estimate of the uncertainty of around 0.01 mA/V can be extracted by comparing these figures.
- Additionally, the G values show a certain spread. Assuming stationary conditions have been reached in run 10 from t = 16 h until t = 32 h, the standard deviation for the measured values amounts to $\sigma = 0.01$ mA/V.
- Thirdly, there is an uncertainty in the calibration factor used. In this case the calibration factor could not be measured accurately and so a mean value was used. The spread of the calibration factors obtained in different facilities (reported in [96]) will be considered later. The mean value is 10^{-8} Vm/As and the standard deviation is around $3.5 \cdot 10^{-9}$ Vm/As.

6.4.5 Metallographic analysis of the LPR sensor's working electrode

After the first and last run (run 1 and run 10) the working electrode of the LPR sensor was analysed in the laboratory by means of SEM and EDX-Mapping. The analyses were carried out by the Institute for Experimental Physics I and II of the Augsburg University. In the first run the fuel used was straw (RSP) and the ring was exposed to the flue gases for approximately 7 hours. In the last run the fuel was doped wood (WP0.1%) and the sensor was exposed for 30 hours. The results are shown in Figure 6.21 and Figure 6.22.

The scale formed on the ring was similar in both runs. On the windward side the outer part of the scale consisted of Cl mixed with K after run 1 and with K and Ca after run 10. The thickness of this layer was around 50 µm after run 1 and 200 µm after run 10, which also left some traces of sulphur mixed with the alkali chlorides. This may indicate sulphation of the deposited chlorides. On the lee side of the rings after run 10 no well-defined layers could be observed. The scale found is a mixture of alkalis, chlorine, sulphur and oxides lacking any discernable structure. Its thickness is about 300 µm.

6.4.5.1 Comparison of the LPR probe with the metallographic corrosion probe

The series of measurements with the LPR sensor and the measurements with the metallographic corrosion probe were carried out simultaneously in the same fluidised bed reactor. The corrosion probe for the metallographic analysis was introduced at position B in Figure 3.3 and the LPR sensor at position A. Figure 6.23 and Figure 6.24 compare the SEM micrographs of the metallographic corrosion probe and the micrographs of the LPR sensor's working electrode after the same run. The scale formed on the LPR sensor's ring is much thicker than that formed on the rings of the metallographic corrosion probe. Judging by these observed differences, it can be concluded that the different position of the probes may play an important role in the formation of the scale on the rings and thus influence the corrosion rates measured. Due to their different position the probes are exposed to the flue gas at different velocities. The flue gas velocity in the freeboard (position B) is much lower than in the flue gas pipe (position A) due to the difference in cross section.

The comparison of the scale on the two probes must also take into account that the temperature of the LPR sensor is 20 °C lower than that of the metallographic probe (metallographic probe: 450 °C; LPR sensor: 430 °C). As explained in section 2.1.1, the tube temperature also has a strong influence on the condensation of the alkali chlorides on the rings.

Finally it is important to remark that the rings of metallographic corrosion probe and LPR sensor are made of slightly different materials (metallographic probe: 10CrMo9-10; LPR sensor: 15Mo3). Hence caution is called for when comparing their corrosion behaviour.

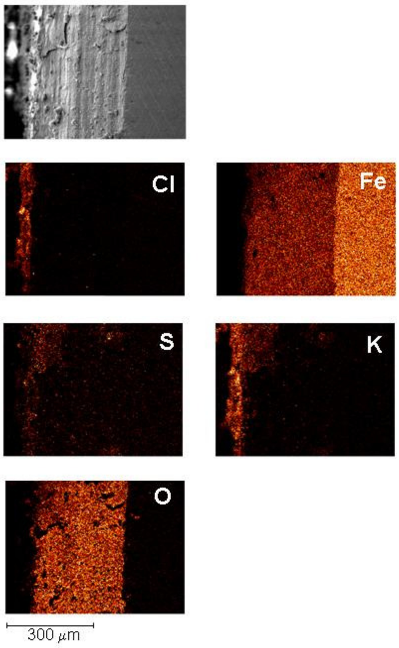

Figure 6.21: SEM and EDX analysis of the rings after run 1 (fuel: RSP; T_{tube} = 430 °C; $T_{flue\ gas}$ ~ 750 °C; exposure time = 7.2h)

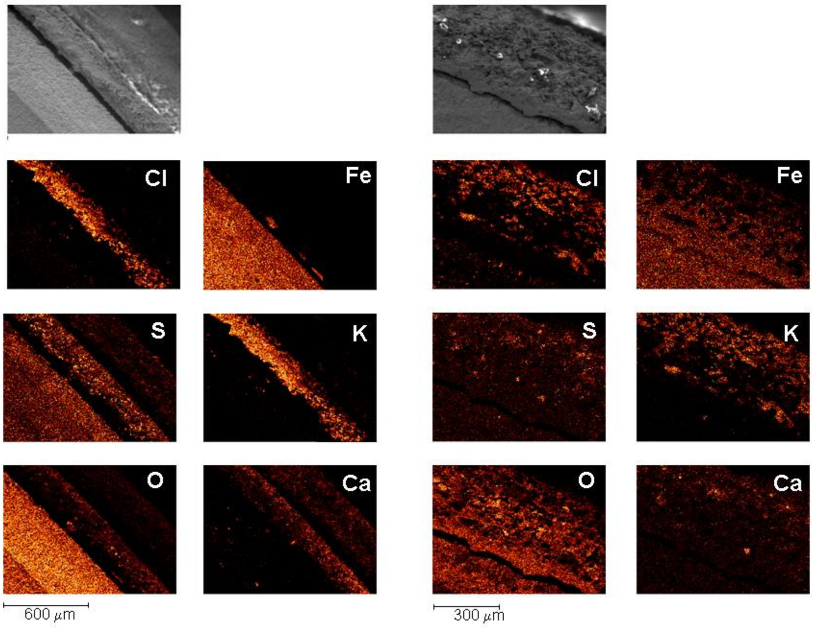

Figure 6.22: SEM and EDX analysis of the rings after run 10 (fuel: WP0.1%; T_{tube} = 430 °C; $T_{flue\ gas}$ ~ 750 °C; exposure time = 30.5h; windward side (left) and lee side (right))

Images prepared by the Institute for Experimental Physics I and II (Augsburg University)

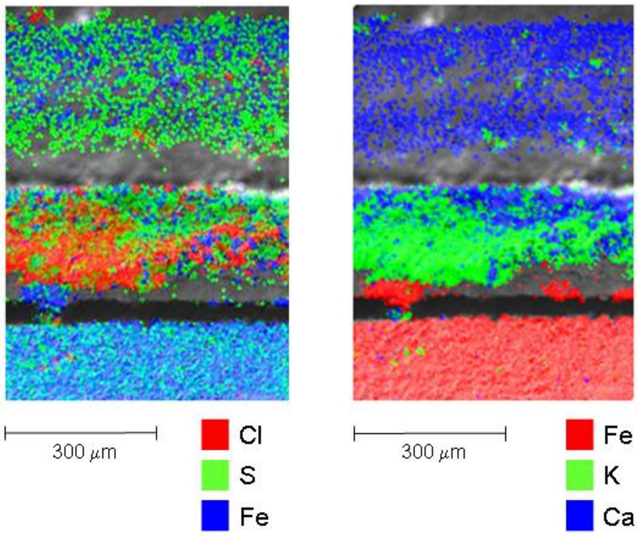

Figure 6.23: EDX pictures of the rings after run 10 of the LPR series of measurements (fuel: WP0.1%; T_{tube} = 430 °C; $T_{flue\ gas}$ ~ 750 °C; exposure time = 30.5 h; ring material 15Mo3)

Image prepared by the Institute for Experimental Physics I and II (Augsburg University)

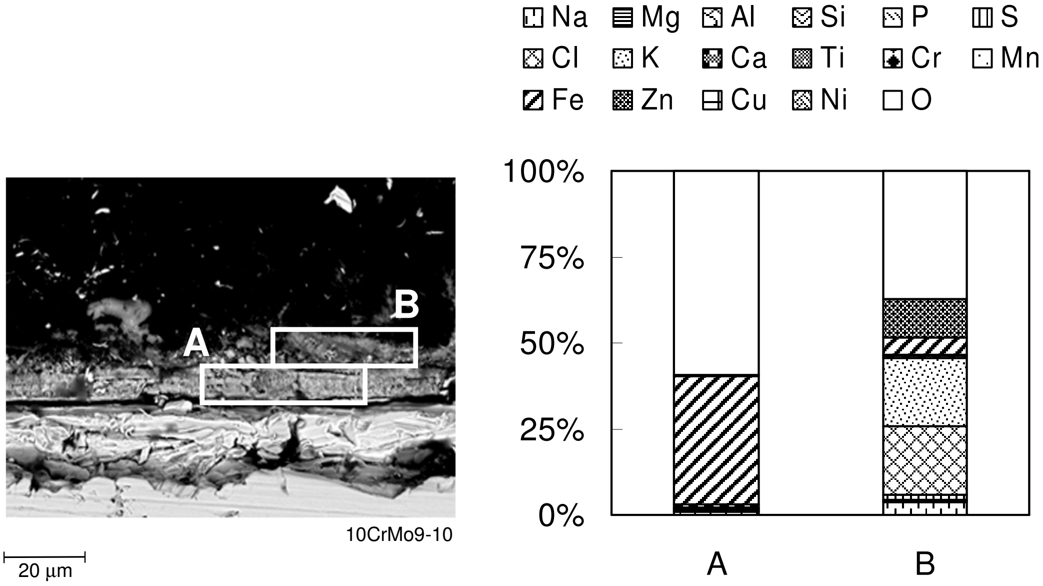

Figure 6.24: SEM picture and composition of the rings (determined by EDX) after run 5 of the metallographic measurements (fuel: WP0.1%; T_{tube} = 450 °C; $T_{flue\ gas}$ ~ 750 °C; exposure time: 8 h; ring material: 10CrMo9-10)

Image prepared by the Process Chemistry Centre of the Åbo Akademi University

6.5 Theoretical evaluation of the results

Reproducible LPC signals were measured during the short-term experiments in the small-scale facility. However, it was observed that an exposure time of 8 hours was not enough for the signal to reach a stationary value. This effect was already mentioned in section 6.1.4 and is attributed to a too high ohmic resistance of the electrolyte in this work.

In the following, a theoretical approach to the interpretation of such low corrosion rates and the constant increase of the measured signal is presented. The LPR sensor and its environment can be modelled by the electric circuit shown in Figure 6.25.

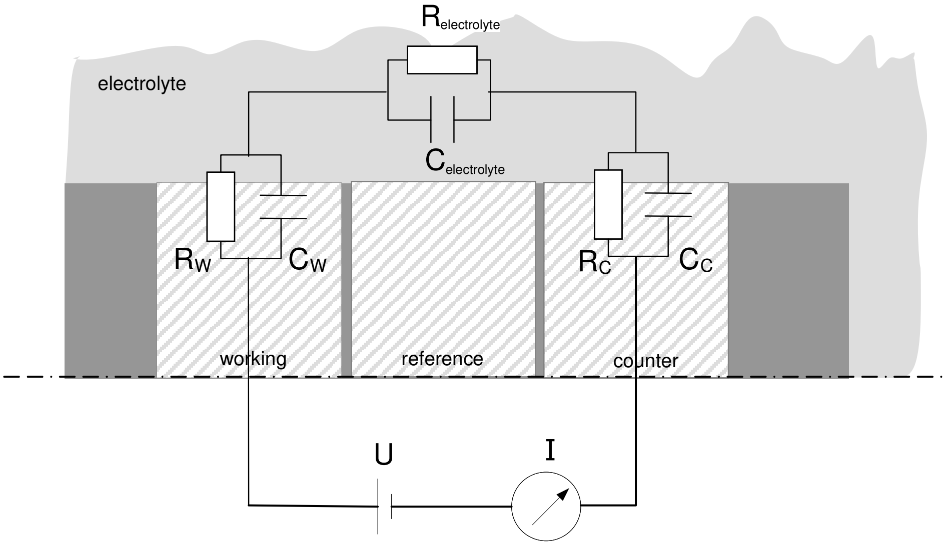

Figure 6.25: Circuit diagram of the LPR sensor's set-up

If the electrolyte's ohmic resistance is not neglected the induced polarisation is divided into three potential drops: the potential drop through the corroding working electrode (η_W), the potential drop through the electrolyte (η_{el}) and the potential drop through the corroding counter electrode (η_C).

$$\eta = \eta_W + \eta_{el} + \eta_C \qquad \text{Eq. 20}$$

Each corroding electrode may be represented by an ohmic resistor R_j connected in parallel with a capacitor C_j (j = W or C; W = working electrode, C = counter electrode). Capacitors have been included to model the oscillatory processes observed in Figure 6.12. In this figure a characteristic time τ' was identified. At this time the slope of the LPC signal flattens to a slope less than or equal to that at the end of the previous run. Figure 6.26 shows the measured free corrosion potential E_o for these runs.

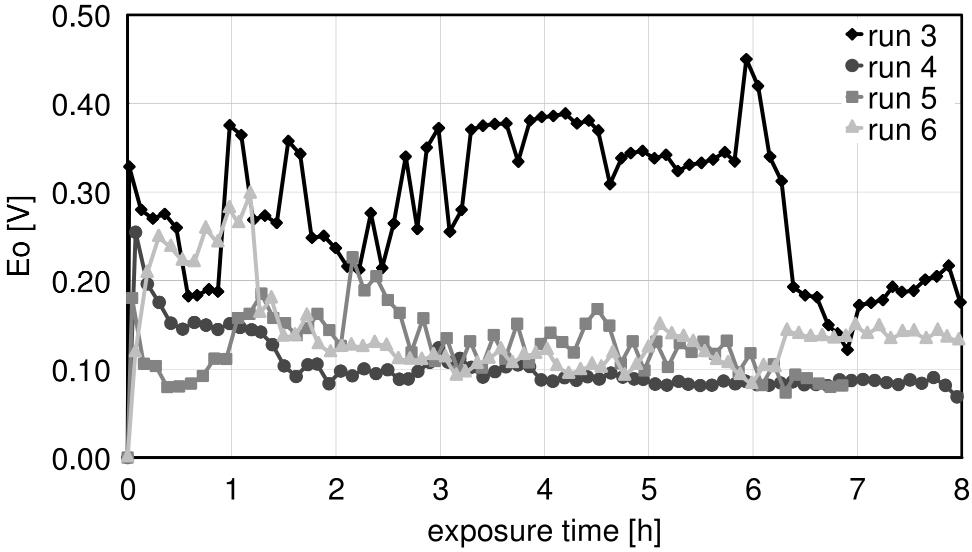

Figure 6.26: Free corrosion potential (E_o) in runs 3 to 6

The free corrosion potential of the re-used rings (in runs 4 to 9) reaches a more or less stationary value after a certain exposure time. This time coincides with τ', when the LPC signal changes its slope. Although no physical interpretation of this behaviour is known, it could be theoretically modelled by an hypothetical capacitor according to Eq. 21, whereby the capacitance would be only relevant for t < τ'. For t > τ' $dU/dt = 0$ and the capacitance could be neglected (the capacitor would be then considered an electrical insulator and its branch of the circuit diagram in Figure 6.25 would play no role in the calculations).

$$C_j = \frac{I - I_o}{dU/dt} \qquad \text{Eq. 21}$$

As explained in 6.1.2, the potential drop through the corroding electrodes at low polarisations is called charge transfer polarisation and is calculated according to Eq. 6:

$$R_W = R_C = \frac{k}{i_o} \qquad \text{Eq. 22}$$

where $k = \frac{RT}{zFA}$. If the electrode's temperature does not change, k has a constant value. Table 6.2 shows typical high, medium and low metal loss rates in power plants and the corresponding values of i_o and R_W calculated with the calibration factor already mentioned before: $1 \cdot 10^{-8}$ Vm/(As).

Table 6.2: R_w for typical corrosion rates ($b = 1 \cdot 10^{-8}$)

metal loss rate [mm/a]	i_o [A/m^2]	R_W ($b = 1 \cdot 10^{-8}$) [Ω]
0.005	0.004	~ 60000
0.05	0.044	~ 6000
0.5	0.4	~ 600
5	4	~ 60

For t > τ' the potential drop through the electrolyte is $\eta_{el} = R_{electrolyte} \cdot I$, where $R_{electrolyte}$ represents the ohmic resistance of the electrolyte. R_{total} is calculated as follows:

$$U = (R_W + R_{electrolyte} + R_C) \cdot I = (2 \cdot R_D + R_{electrolyte}) \cdot I = R_{total} \cdot I \qquad \text{Eq. 23}$$

$$\frac{dU}{dI} = R_{total} \qquad \text{Eq. 24}$$

Figure 6.27 shows the values of R_{total} derived by inverting the G signal from Figure 6.11. The measuring period consists of three different phases: A) 32 hours of exposure to the flue gases of a highly corrosive fuel (WP0.5%), B) 16 hours' exposure to the flue gases of a less corrosive fuel (WP) and C) 4.5 hours' exposure to the flue gases of a particularly corrosive fuel (RSP).

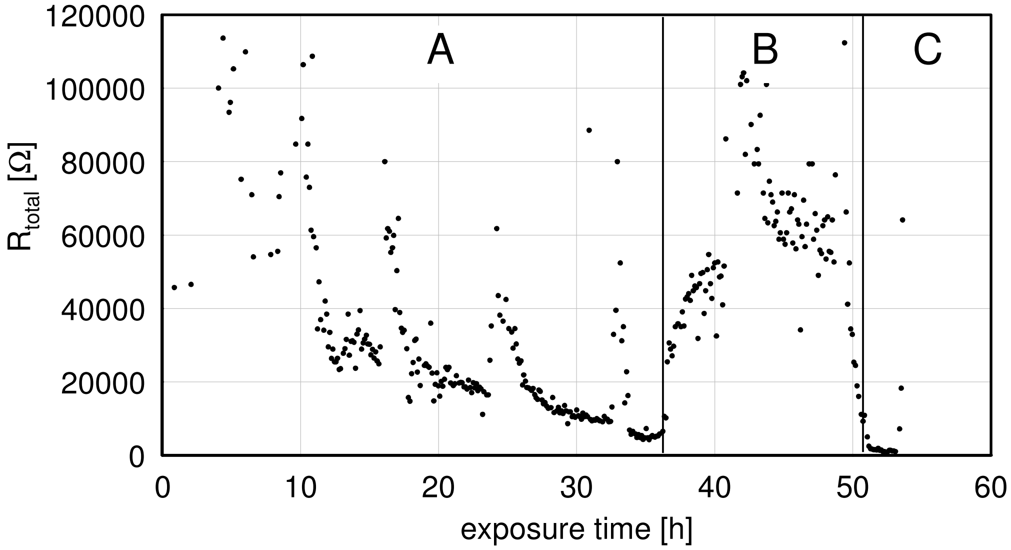

Figure 6.27: Polarisation resistance (R_{total}) in runs 3 to 9

R_{total} has very high values during the first hours of exposure and decreases to values around 5 kΩ during phase A after 32 hours of exposure. If short-term oscillations are neglected this decrease seems to follow a continuous tendency decreasing gradually after every experiment. This decrease of the resistance may be attributed to the formation of the electrolyte between the rings. As already explained, the electrolyte's resistance R_{Ω} is the main contributor to the total resistance measured during this phase while the charge transfer resistances at the electrodes R_W are all but negligible.

During phase B wood pellets are burnt so that the electrodes are exposed to a less corrosive flue gas. As can be seen in Figure 6.27, there is a great increase in the measured polarisation resistance to values around 60 kΩ. This increase may be due to an increase of the working electrode's resistance R_W caused by a lower corrosion current i_o. In Table 6.2 an R_W value of around 60 kΩ corresponds to a corrosion rate of about 0.005 mm/a, which is in the order of magnitude of the value expected for the combustion of wood. Thus the assumption that the increase in the polarisation resistance is due to the change in R_W appears plausible.

If the fuel is changed to straw as in phase C, the resistance decreases to values around 1 kΩ. Furthermore the slope of the polarisation resistance at the beginning of phase C seems to coincide with the slope at the end of phase A and follows roughly the same tendency observed in phase A. During phase C high corrosion rates and electrode resistances in the order of magnitude of 60 to 600 Ω are expected. The value of the measured polarisation resistance is close to these values. From these results it may be concluded that exposure times of at least 50 hours (~ 2 days) are necessary for the electrolyte's ohmic resistance to become negligible, so that the polarisation resistance can be considered inversely proportional to the corrosion rate.

6.5.1 Measurement of the electrolyte's ohmic resistance

In section 6.1.2 the different types of polarisation in a polarised electrochemical system were described. The total polarisation is calculated as follows:

$$\eta = \eta_D + \eta_d + \eta_r + \eta_c + \eta_\Omega \qquad \text{Eq. 25}$$

It was assumed (following [48]) that η_d, η_r and η_c are negligible for low polarisations. The polarisation resistances measured in this work have shown that for short exposure times, the ohmic resistance of the electrolyte cannot be neglected and the LPR signal is not inversely proportional to corrosion rate.

It can be concluded that the short-term measurement of corrosion rates by means of linear polarisation resistance requires the measurement of the ohmic resistance of the electrolyte.

In the following, one method for the measurement of the electrolyte's ohmic resistance is presented. The polarisations included in Eq. 25 were described in detail in section 6.1.2. Later the principle of linear polarisation measurements was shown to be based on an induced polarisation of the system. This polarisation must be low enough to guarantee a linear relationship between the charge transfer polarisation and the external current, see Eq. 26.

$$|\eta_D| << RT/(zF) \Rightarrow \boxed{\eta_D = \frac{RT}{zFi_o} \cdot i \cdot} \qquad \text{Eq. 26}$$

For high polarisations this linearity cannot be assumed. Equations Eq. 27 to Eq. 31 describe the behaviour of the different types of polarisation for high total polarisations.

Charge transfer polarisation:

$$i = i_c + i_a = i_o \left[\exp\left(\frac{\alpha z F}{RT} \eta_D \right) - \exp\left(-\frac{(1-\alpha) z F}{RT} \eta_D \right) \right],$$

$$\text{which yields } |\eta_D| >> RT/(zF) \Rightarrow \boxed{\eta_D = \beta \cdot \log \frac{i}{i_o}} \qquad \text{Eq. 27}$$

Diffusion polarisation:

$$\boxed{\eta_d = \frac{RT}{zF} \sum_j \nu_j \ln\left(1 - \frac{i}{i_{max}} \right)} \qquad \text{Eq. 28}$$

Reaction polarisation:

$$\boxed{\eta_r = \frac{RT}{zF} \sum_j \nu_j \ln\left(\frac{a_j}{\overline{a}} \right)} \qquad \text{Eq. 29}$$

Crystallisation polarisation:

$$\boxed{\eta_c = -\frac{RT}{zF} \ln \frac{a_{m_j}}{\overline{a}_m}} \qquad \text{Eq. 30}$$

Ohmic resistance of the electrolyte:

$$\boxed{\eta_\Omega = R_\Omega \cdot I} \qquad \text{Eq. 31}$$

These equations show that all the different types of polarisation depend logarithmically on the current, except for η_d and η_Ω. Assuming diffusion is not the constraining process ($i_{max} >> i$) η_d can be neglected (the formation of fast diffusion paths during high-temperature chlorine-induced corrosion was already explained in 2.1.1.1). For high polarisations the total polarisation and the resulting polarisation resistance can be then approximated as follows, using suitable constants A_j and B_j in Volts und 1/A respectively (i is the external current density, I the external current):

$$\eta = A_0 + \sum_{j=1}^{4} A_j \ln(B_j i) + R_\Omega \cdot I \qquad \text{Eq. 32}$$

$$R_{total} = \frac{dU}{dI} = \sum_{j=1}^{4} \frac{A_j B_j}{i} + R_\Omega \qquad \text{Eq. 33}$$

$$i \to \infty \Rightarrow R_{total} \cong R_\Omega , \qquad \text{Eq. 34}$$

whereby the coefficients A_j and B_j depend on the parameters explained in section 6.1.2. If the current is high enough the measured polarisation resistance can be assumed to be the electrolyte's ohmic resistance.

In order to take this into account, a third step could be included in the polarisation measurement loop of the potentiostat explained in 6.1.3: (1) low polarisation for the measurement of R_P, (2) measurement of the free corrosion potential E_o and (3) high polarisation for the measurement of R_Ω (= $R_{electrolyte}$). Using these values the corrosion rate r could be then calculated according to Eq. 35:

$$\frac{dU}{dI} = \frac{RT}{zFi_oA} + R_\Omega \Rightarrow \boxed{r = \frac{i_oM}{zF\rho} \left[\frac{m}{s}\right]} \qquad \text{Eq. 35}$$

The proposed third measurement would allow for the correction of the underestimation of corrosion rates during short-term measurements.

Apart from this approach the electrolyte's ohmic resistance can be measured by means of electrochemical impedance spectroscopy (EIS) techniques (see 2.1.3). A description of the measuring principle as well as results from some series of measurements can be found in the PhD Thesis of Maisch “Identifikation und Quantifizierung von Korrosionsrelevanten Parametern in Müllverbrennungsanlagen mittels Charakterisierung der deponierten Partikel und elektrochsmischer Online-Messungen” [22].

6.6 Summary

The short-term application of the LPR technique for the measurement of corrosion was investigated. LPC signals were obtained for combustion tests of 8 and 30 hours of duration with different fuels. Reproducible signals were obtained. The LPC values obtained were about two orders of magnitude lower than typical values obtained in real plants. The LPC signal depended strongly on the exposure of the sensor to flue gases. Even for the probes already covered with deposits from previous tests, the LPC signal was zero until combustion began. Additionally, a good correlation of the LPC signals with the presence or absence of corrosive species in the flue gas was observed.

The shape of the signals indicated that no stationary conditions were reached after 8 hours. Stationary conditions might be reached after an exposure time of at least 50 hours. Before that the corrosion rate is underestimated due to the fact that the electrolyte’s ohmic resistance cannot be neglected.

In this work a method of measuring the electrolyte’s ohmic resistance has been proposed that could help to correct the underestimation during the first 50 hours of the combustion tests. Corresponding algorithms for calculating corrosion rates more accurately using the measured electrolyte resistance were justified theoretically.

7 Agglomeration tests

Within the framework of this research the short-term agglomeration behaviour of straw was investigated. Rye straw pellets (RSP) and wheat straw pellets (WSP) were burnt in a small-scale fluidised bed reactor for 8 hours or until defluidisation occurred. Tests with wood pellets (WP) were also carried out for comparison. The fuels used are described in section 3.2 and their composition is given in Table 3.2 and Table 3.3. As explained in section 2.2.1 it is mainly Si, K and Ca that are responsible for the formation of low-melting eutectica and thus for agglomeration. The agglomeration tendency increases with the K content and decreases with the Ca content of the fuel. Compared with other biomasses rye and wheat straw pellets have a high and medium K content respectively while their Ca content is relatively low. Wood pellets are an example of a biomass with low K and low Ca content. Figure 7.1 compares the fuel ash composition after combustion of these three fuels.

The fuel ash referred to here is the ash obtained in the laboratory under the conditions specified in the DIN 51719 norm (see [99]). The composition of the fuel ash from the two types of straw is similar and they have a much higher SiO_2 and K_2O content than wood. On the other hand their CaO content is lower than that of wood. Quartz sand was used as bed material (grain diameter: 0.7-1.2 mm). For each test (with a different fuel) the bed material was renewed. After combustion the agglomerates formed as well as some ash samples from the reactor were analysed in the laboratory. Their composition was then compared with the composition of the fuel ashes (see details below).

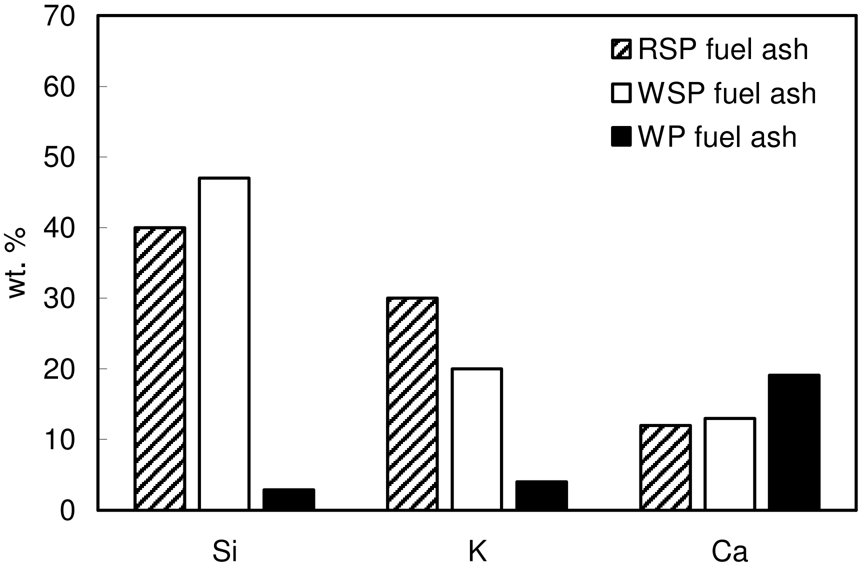

Figure 7.1: Fuel ash composition for rye straw pellets (RSP), wheat straw pellets (WSP) and wood pellets (WP)

7.1 Experimental procedure

The fluidised bed reactor used was described in section 3.1. The reactor was preheated electrically to a bed temperature of about 570 °C and then fuel feeding started. The fuel feeding rate and the fluidisation air flow were kept approximately constant (3 kg/h and 15 Nm^3/h respectively) for about 8 hours or until defluidisation occured. The temperature of the bed was controlled by the electric heating of the fluidisation air. The reactor temperatures, the pressure drop in the bed, air flow and flue gas composition were monitored and recorded continuously during the experiments. After 8 hours or if defluidisation occurred, fuel feeding and electric heating were switched off. Once the bed had cooled down, samples of agglomerates (if present) and ashes from the bed and the cyclone were carefully collected for EDX analysis in the laboratory. Table 7.1 gives an overview of the tests carried out and their main parameters.

Table 7.1: Test parameters for the agglomeration tests (T_{bed} = 800 °C)

Run#	fuel	combustion time [h]	defluidisation	agglomerates
1	RSP	6.2	yes	yes
2	WSP	7.2	no	yes
3	WP	8x 3 = 24	no	no

7.2 Results

In spite of the short duration of the tests agglomerates were found in the bed after every test that used straw as fuel. In the case of rye straw pellets, melting-induced and coating-induced agglomerates were found. For this fuel agglomeration led to defluidisation of the bed after only 6 hours of combustion. Figure 7.2 shows the appearance of the agglomerates found. The structure of the melting-induced agglomerates obtained here coincides to that reported by Lin *et al.* [52]: a fragile black ash core of about 10 mm has sand particles glued to it, see Figure 7.2 (left). The coating-induced agglomerates were white, of very irregular shape, less fragile and had a glassy surface (see Figure 7.2 (right)). Their size varied between 30 and 50 mm.

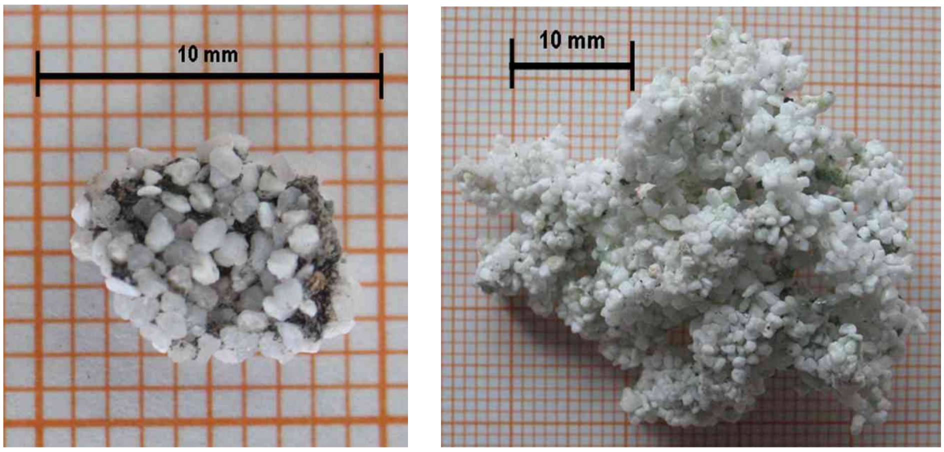

Figure 7.2: Agglomerates found during the agglomeration tests: melting-induced (left) and coating-induced (right)

Using wheat straw as fuel, no defluidisation occurred during combustion, but melting-induced agglomerates similar to the one shown in Figure 7.2 (left) were collected.

No agglomerates were found after the combustion of wood pellets, even after repeating the test three times with the same bed material.

The composition of the agglomerates found after rye straw combustion is shown in Figure 7.3.

The black core and the particulate surface of the melting-induced agglomerates have very similar Si, K and Ca contents to those of the fuel and fly ash (the latter is the ash which leaves the reactor with the flue gas and is caught in the cyclone). In some cases more K and a lower Ca content can be observed on the particulate surfaces. The melting-induced mechanism is assumed to be responsible for their formation. The composition of the fly ash is very similar to that of the fuel ashes obtained in the laboratory. In the case of coating-induced agglomerates their surfaces show a higher Si content than those of the ashes. The agglomerates were embedded in epoxy resin and cut for analysis. In the core of bed particles glued together in the agglomerate almost only Si is found.

After the combustion of wheat straw only melting-induced agglomerates were found. Their composition is shown in Figure 7.4. As in the case of rye straw agglomerates the composition of the black core is very similar to that of the fuel and fly ashes.

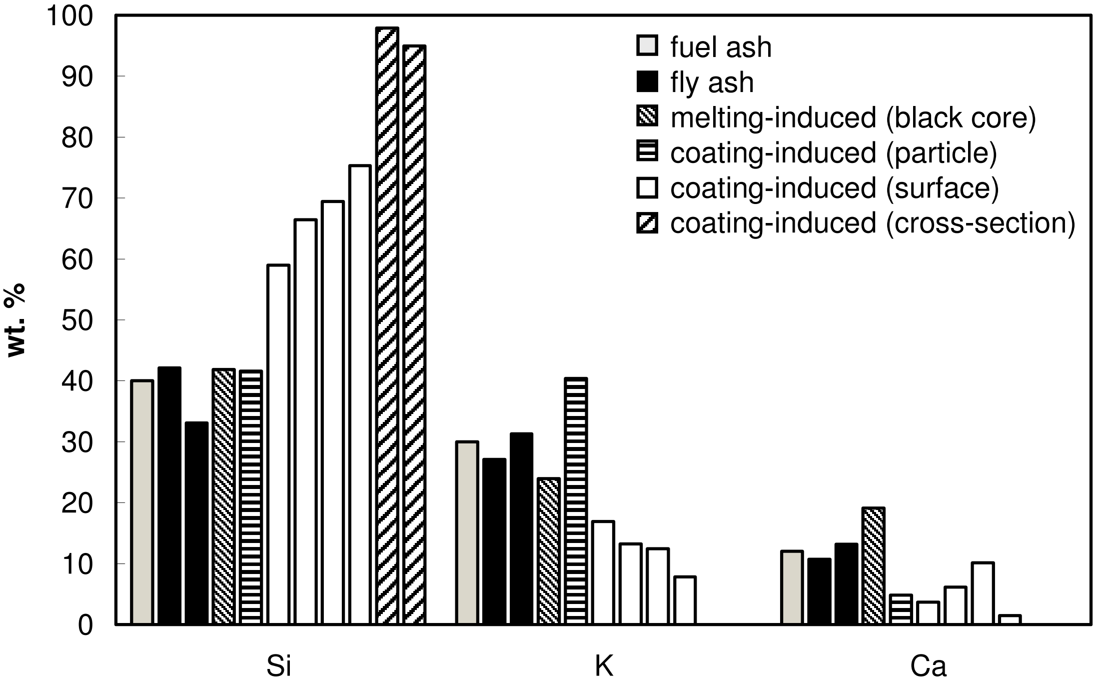

Figure 7.3: Si, K and Ca contents of the agglomerates obtained during the combustion of rye straw pellets (T_{bed} = 800 °C)

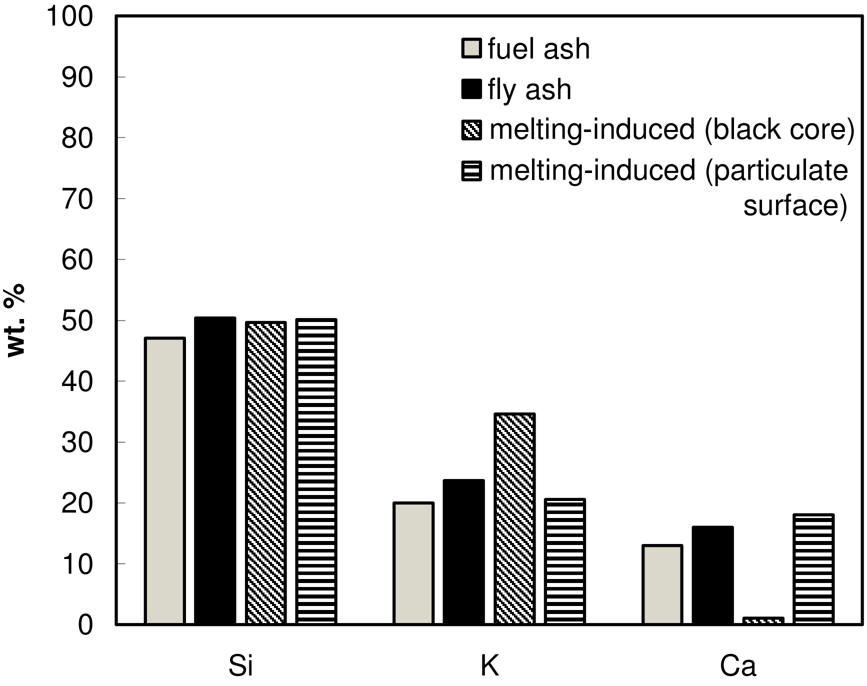

Figure 7.4: Si, K and Ca contents of the agglomerates obtained during the combustion of wheat straw pellets (T_{bed} = 800 °C)

7.3 Conclusions

The results shown in the previous section confirm the predictions based on the literature. Straw pellets with a higher K and lower Ca content than wood gave rise to a higher agglomeration tendency. Furthermore both types of agglomeration reported in the literature were observed after combustion of the fuel with the highest K content (RSP). Because of their greater size and higher tenacity, coating-induced agglomerates are supposed to be responsible for the defluidisation of the bed.

The composition of the ash and the agglomerates shown in Figure 7.3 and Figure 7.4 are presented in the liquidus projection of the SiO_2-CaO-K_2O ternary diagram in Figure 7.5. The relatively high K content and low Ca content of the fuel results in a low-melting ash. According to the diagram the expected melting temperature is around 720 °C, a temperature far below the bed temperature during the tests (800 °C). According to Öhman *et al.* [57], melting-induced agglomerates (called homogeneous agglomerates) are located in a zone of melting temperatures around 800 °C in the diagram and coating-induced (heterogeneous) agglomerates are found at around 720 °C. This is also the case for the agglomerates found in this research.

Although the composition of wheat straw ashes (black triangle in Figure 7.5 (bottom)) is closer to the composition of the coating-induced agglomerates (red circles in Figure 7.5 (top)) than that of rye straw ashes, no such agglomerates were formed during the combustion of WSP. This confirms that coating-induced mechanism described in 2.2.1. The formation of this kind of agglomerates requires an interaction between the potassium vapours in the flue gas and the silicium from the particles. This interaction may form a low-melting eutectic mixture which constitutes a layer that grows inwards toward the core particle as concluded by Brus *et al.* [58, 100] (see section 2.2.1). This layer glues the particles together firmly, such that large, hard agglomerates are formed.

It can be concluded that combustion tests of less than 8 hours of duration are sufficient for agglomerates to form in order to study the agglomeration behaviour of problematic fuels like straw. The agglomerates formed can be studied in the laboratory and the correlation between the combustion conditions, fuel composition and agglomeration tendency can be investigated.

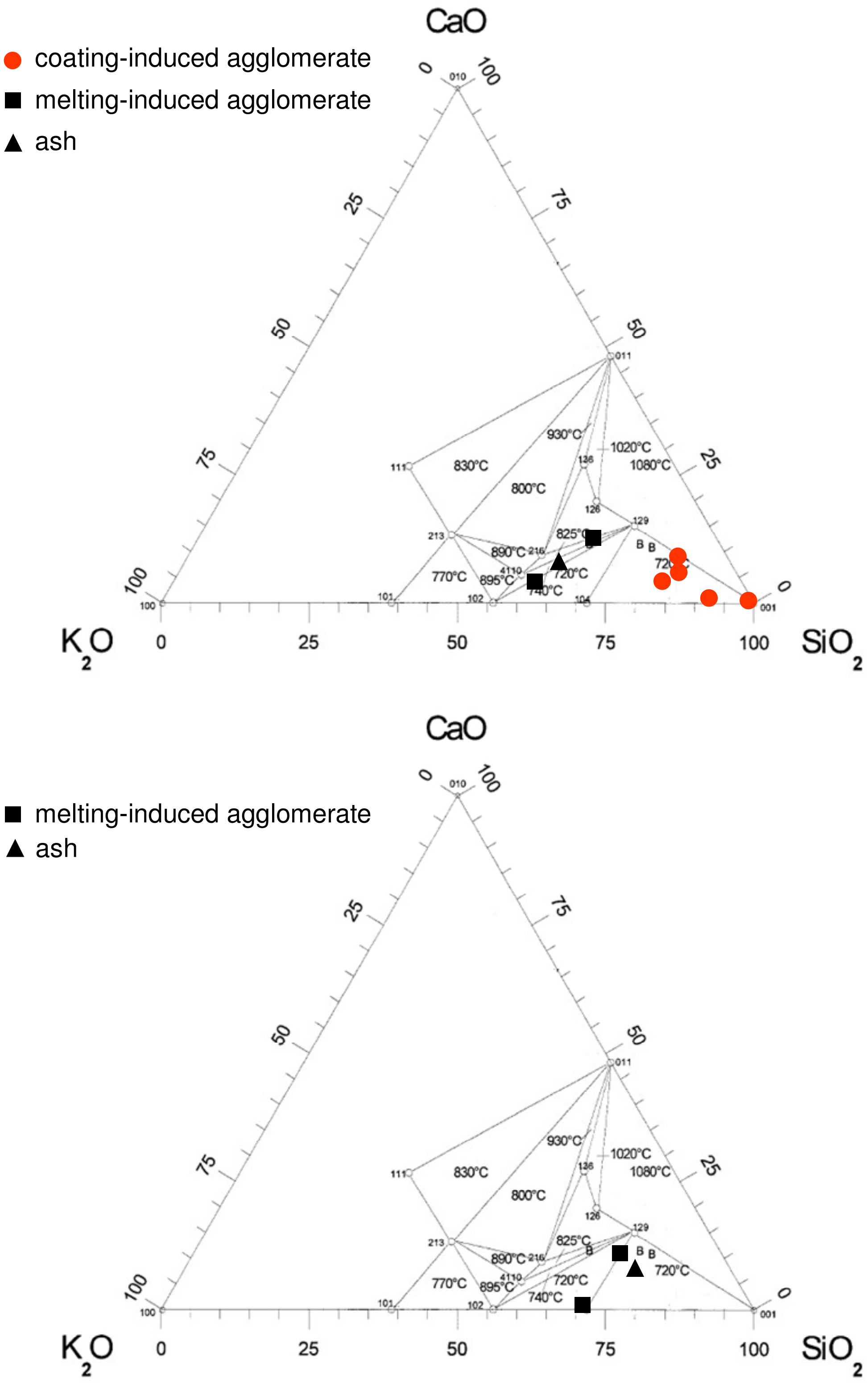

Figure 7.5: Location of the rye straw agglomerates (top) and wheat straw agglomerates (bottom) in the liquidus projection of the SiO_2-CaO-K_2O ternary diagram

8 Power plant tests

The tests described in the previous chapters were carried out in a small-scale facility. In the introduction the fact that small-scale tests are easier to control and yield more accurate results than tests in a commercial power plant was stated as their main advantage. Within the framework of this research additional LPR and metallographic measurements were carried out in an EfW plant together with the Institute for Experimental Physics I and II of the Augsburg University. The aim of these additional tests was to compare small-scale and power plant measurements from the point of view of feasibility as well as quality and quantity of the information obtained.

8.1 Description of the EfW plant

The EfW plant has a capacity of 180,000 tonnes per year with approximately 10% of the waste burnt being hospital waste[3]. Because of its high plastic content (mainly polyvinyl chloride PVC) this waste is expected to have a higher calorific value and a higher corrosion potential than standard waste. The combustion line on which the tests were carried out has a capacity of 15 t/h.

Live steam pressure and temperature are 42 bar and 380 °C respectively. The steam and flue gas paths are shown in Figure 8.1. The feedwater from the condenser is preheated in the economiser located in the fourth pass. The water flows from the economiser through

---

[3] Hospital waste is defined by the World Health Organisation as the „waste generated by health care activities, including a broad range of materials, from used needles and syringes to soiled dressings, body parts, diagnostic samples, blood, chemicals, pharmaceuticals, medical devices and radioactive materials" [101].

the double-drum evaporator. The saturated steam then leaves the drum and is superheated in two platen heat exchangers situated in the second pass. The average steam flow supplied by this line to the turbine is around 33 t/h. The steam temperature is controlled by a spray water attemperator between the two superheaters. The steam expands in the turbine and is condensed with air to complete the cycle.

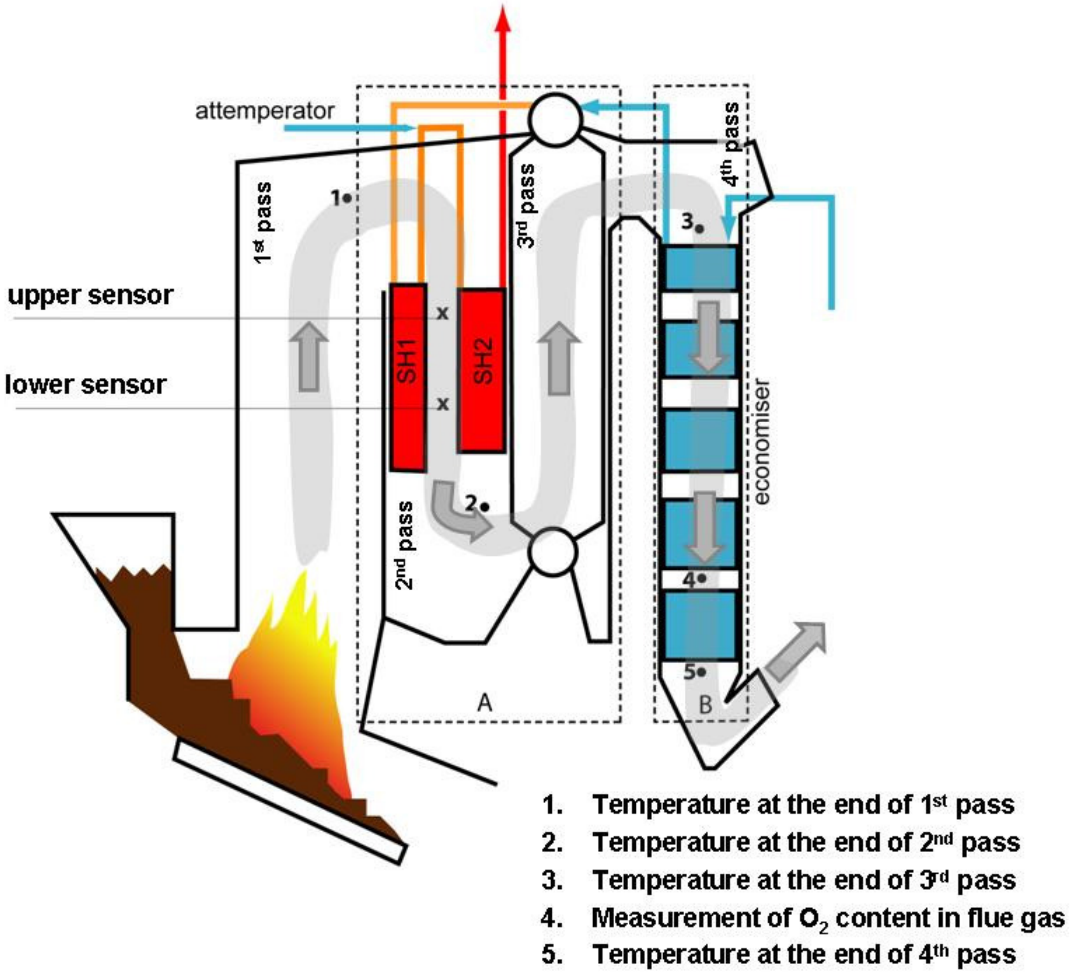

Figure 8.1: Steam and flue gas path in the EfW plant

Some characteristics of this plant concerning corrosion are the following:

1. The superheaters are located in the second pass and are exposed to higher flue gas temperatures than standard superheaters (~800 °C). In Figure 8.2 superheaters 1 and 2 are displayed in the Flingern corrosion diagram.
2. The superheater tubes are parallel to the flue gas flow and not transverse to it, as would usually be the case. The incident flow of flue gas is responsible for

transporting chlorine and alkalis to the superheater tubes and its orientation may have a decisive influence on the corrosion reaction.

3. A relatively high percentage of hospital waste is burnt so that a high concentration of corrosive species is expected in the flue gas.
4. Deposits on the heat exchangers' surfaces are removed periodically by means of explosive cleanings in zone A of the furnace and vibrating units in zone B of the furnace (see Figure 8.1).

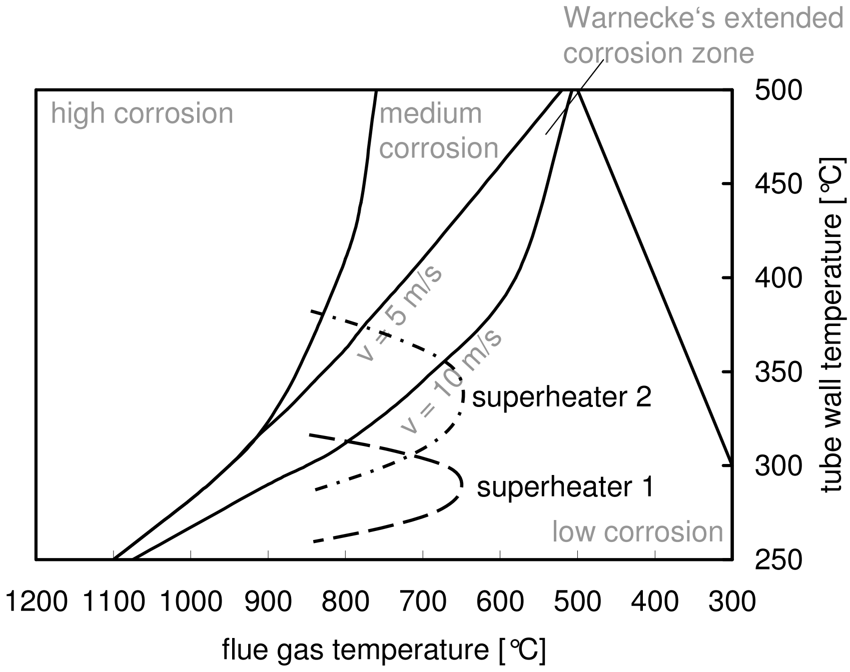

Figure 8.2: Position of the EfW plant superheaters in the Flingern corrosion diagram

8.2 Measuring set-up

Two LPR sensors were installed in the facility at the positions shown in Figure 8.1. Both sensors are located between the two superheaters, whereby the lower sensor is situated half-way along the length of the superheaters, somewhat downstream of the upper sensor with respect to the flow of flue gas. The flue gas temperature at these two positions is between 620 °C and 900 °C. The temperature of the sensors is 380 °C. Both sensors are connected to the potentiostat controlled by the computer. The corrosion signal is sent to the control room of the facility and is accessible to another external computer via the internet. Each sensor head is cooled with pressurised air (at 6 bar) and the tube holding is cooled with water. The sensors are connected to two cooling units that are refilled automatically and regulate the temperature of the sensor head. Apart from the supply of power, water and pressurised air and the internet connection, the system is self-sufficient and restarts automatically in the case of a power failure or a water supply outage.

Due to the proximity of the sensors to the site of explosive cleaning, they were retracted by approximately 1.5 m during the explosions to avoid damage to the sensor heads. Later on in the project it became evident that the sensor heads could withstand the explosive cleanings without being retracted. The position of both sensors in the Flingern corrosion diagram is displayed in Figure 8.3.

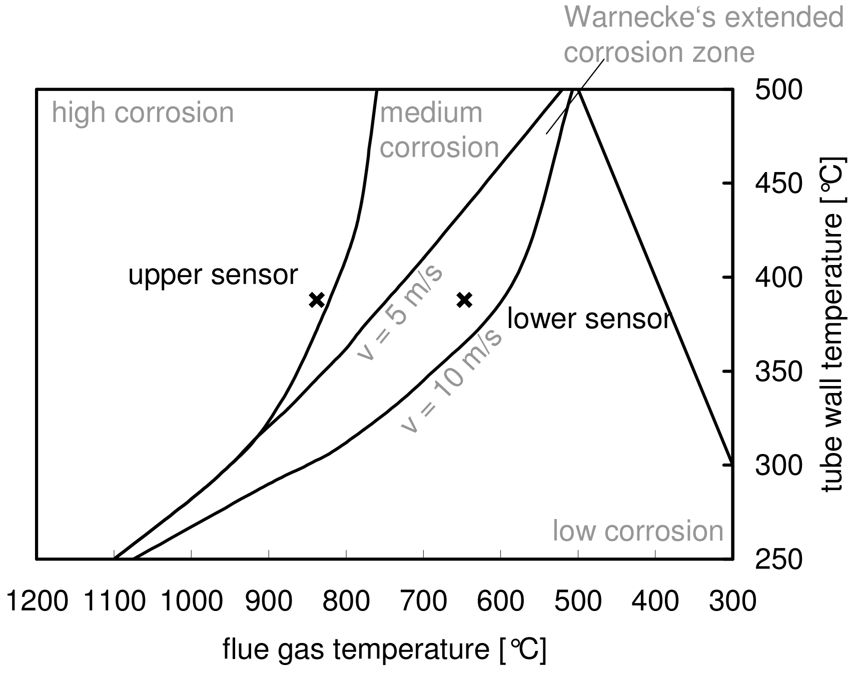

Figure 8.3: Position in the Flingern corrosion diagram of the LPR sensors used for the series of measurements in the EfW plant

8.3 Thermodynamic calculations for the EfW plant

The initial processing of the available data on the operational parameters of the facility showed that some important variables were unknown and others were subject to large uncertainties. This is normal in power plants since they are not designed for research purposes. In order to compensate for the lack of detailed and accurate operational data, a thermodynamic model of the plant was constructed. The model enables a better analysis and understanding of the plant's operation. For the modelling of the plant KED's PowerPlantSimulator&Designer (PPSD) software was used. PPSD is a process simulation programme based on the calculation of mass and energy balances. The main advantage of PPSD over other similar programmes is its high suitability for modelling energy-from-waste plants in particular. PPSD libraries include a wide variety of standard components of EfW plants. The software can be used to simulate the plant's performance under various conditions, enabling the user to check measured parameters (by comparison with calculated values) and to simulate plant modifications.

Each plant component (pump, heat exchanger, etc.) is considered a "black box" with certain properties (geometry, mass loss rate, etc.) to be specified by the user. Solid, liquid or gas flows are inputs to and outputs from these "boxes". The properties of the flow at each point in the process can be calculated by applying heat and mass balances to each component.

In the case of an EfW plant the exhaust gas path and the steam path are modelled separately as shown in Figure 8.4. Each path is divided into different stages that will not be described in more detail here but can easily be identified in the model described in the following sections.

8.3.1 The PPSD model

The PPSD model was first constructed on the basis of the plant documentation and available reference data. As already explained, the superheaters of this facility are platen superheaters situated in the second pass. These superheaters were simulated by standard radiant components, i.e. components situated in the zone of the boiler where radiation is predominant. The specifications of these components were adjusted to correspond as closely as possible to those of the platen superheaters. The final model (of the flue gas and steam path) is shown in Figure 8.4. Once all the components of the model are defined and connected, the model is adjusted by fine-tuning the fouling factor of each heat exchanger in the boiler. The fouling factors are coefficients used in the heat transfer balances in order to take into account the effect of fouling and slagging on the heat exchanger. Table 8.1 compares the values simulated by the model with the measured ones (DATA SET 1). The three first columns show the reference data, the data calculated by the model and the discrepancies between calculated and measured values. The model was optimised until these discrepancies were lower than 5% for all the parameters. This is in the order of magnitude of the uncertainty of the measured values [85].

Once optimised and validated the model was used for the simulation of different periods of operation of the plant (Table 8.2 for DATA SET 2 and Table 8.3 for DATA SET 3).

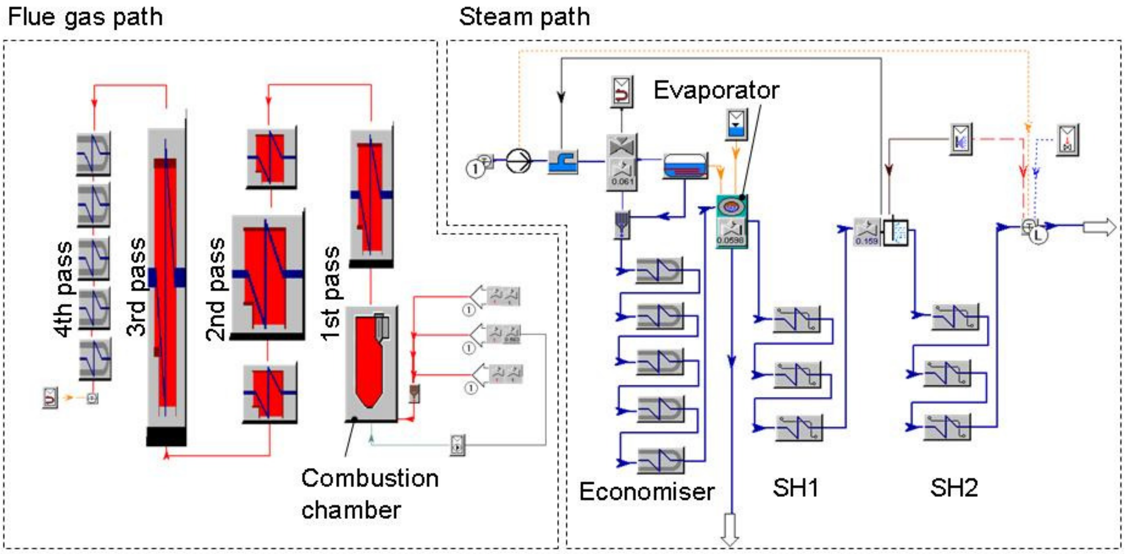

Figure 8.4: Flue gas and steam path in the PPSD model

8.3.2 Conclusions from the experiments based on the PPSD model

Table 8.1, Table 8.2 and Table 8.3 compare the values predicted by the model with the measured values from DATA SETs 2 and 3. The largest discrepancy between calculated and measured values is observed for the flue gas temperatures and for the air flow (these deviations exceed 5%). This disagreement is associated with the following two factors affecting the boiler:

- The first is the fouling of the boiler. DATA SETs 2 and 3 pertain to measurements made shortly after explosive cleanings. The aim of the explosions is to clean the boiler and remove the deposits on the walls and tubes exposed to the flue gases. The removal of the deposits improves the heat exchange between the flue gas and the steam so that the flue gas cools down faster. Thus the flue gas temperature decreases in zones affected by the explosive cleaning. This effect is manifested in the flue gas temperatures measured at the end of the second, third and fourth pass, for instance. Since the fouling factors have only been adjusted for DATA SET 1 the model does not take into account this effect. Therefore the temperatures measured in the second, third and fourth pass (which are affected by the explosive cleaning) are lower than the ones predicted by the model (hence the negative deviations in Table 8.1). The opposite effect (a positive deviation) is observed for the temperature at the end of the first pass, where no explosive cleaning took place.
- The second factor is the ingress of excess air into the plant. The air flow calculated by the model for DATA SETs 2 and 3 is much higher than the measured air flow with errors of about 10% and 30% respectively. One considerable hole in the boiler wall was detected at a later stage of the experiments. Through this hole additional air enters the boiler without being measured and is available for combustion. Hence the measured value underestimates the actual air flow in the plant. Furthermore the difference between the measured and the simulated values supplies a rough quantification of the effective ingress of air into the plant (false air in Table 8.2 and Table 8.3). The increase of the discrepancy from DATA SET 2 to DATA SET 3 indicates a deterioration of the

boiler between the measurements. After compiling DATA SET 3 the plant was shut down for repairs.

One of the benefits of modelling the plant is that certain parameters that are not measured during operation can be calculated. In commercial plants the number of measuring points is limited. Sensors are expensive and require a lot of maintenance. Therefore only the parameters relevant for the operation of the plant are measured. With the energy and mass balances of the model some of the unknown parameters can be calculated. One example is the flue gas flow, which determines the flue gas velocity near the tubes. The flue gas velocity has an influence on the corrosion rate since it is responsible for the supply of reactants taking part in the corrosion reaction. For flue gas velocities significantly higher than 5 m/s (up to 10 m/s) Warnecke proposed a modification of the Flingern corrosion diagram (see Figure 2.1). The flue gas flow calculated by the model is (53344 Nm^3/h). The flue gas flow was measured with a pitot tube during one of the series of measurements, yielding a value of around 51350 Nm^3/h, which is in the same order of magnitude as the calculated value (deviating by less than 4%). The estimated flue gas velocity around the tubes is therefore about 5 m/s, corresponding roughly to that of the standard Flingern corrosion diagram (without Warnecke’s extension).

The use of a PPSD model like the one presented in this section helps to detect and quantify inconsistencies in the energy and mass balances of the plant. They are usually associated with damage on the plant (such as the hole in the wall causing an ingress of air, for instance) or with the deterioration of the sensors (for example due to fouling of the thermocouples). In addition to this the model supplies estimates of all the operational parameters that are not measured in the plant but are relevant for the evaluation of the results.

Table 8.1: Measured and calculated values for DATA SET 1

parameter	units	measured value (DATA SET 1)	value in model	discrepancy [%]
drum pressure	bar	43.2	45.0	-4.2
water flow	t/h	33.8	34.2	-1.2
T flue gas end of 1st pass	°C	863	863	0.1
T flue gas end of 2nd pass	°C	621	621	0.1
T flue gas end of 3rd pass	°C	448	448	0.1
T flue gas end of 4th pass	°C	242	242	0.2
live steam pressure	bar	41.9	42	-0.2
T steam downstream SH1	°C	319	311	2.6
T steam upstream SH2	°C	263	272	-3.3
air flow	Nm^3/h	48918	49656	-1.5

Table 8.2: Measured and calculated values for DATA SET 2

parameter	units	measured value (DATA SET 2)	value in model	discrepancy [%]
drum pressure	bar	43.4	45.1	-3.9
water flow	t/h	33.5	32.8	2.1
T flue gas end of 1st pass	°C	907	844	7.0
T flue gas end of 2nd pass	°C	579	636	-9.8
T flue gas end of 3rd pass	°C	443	464	-4.6
T flue gas end of 4th pass	°C	237	255	-7.8
live steam pressure	bar	42.1	42.1	0.0
T steam downstream SH1	°C	317	309	2.5
T steam upstream SH2	°C	295	283	3.9
air flow	Nm^3/h	51794	57074	-10.2
false air	Nm^3/h	-	~5200	

Table 8.3: Measured and calculated values for DATA SET 3

parameter	units	measured value (DATA SET 3)	value in model	discrepancy [%]
drum pressure	bar	43.4	44.9	-3.5
water flow	t/h	33.9	32.6	3.8
T flue gas end of 1st pass	°C	915	833	9.0
T flue gas end of 2nd pass	°C	600	640	-6.6
T flue gas end of 3rd pass	°C	437	470	-7.4
T flue gas end of 4th pass	°C	233	259	-11.1
live steam pressure	bar	42.1	41.9	0.5
T steam downstream SH1	°C	318	308	3.3
T steam upstream SH2	°C	283	283	0.3
air flow	Nm^3/h	46941	60351	-28.6
false air	Nm^3/h	-	~13400	

8.4 LPR measurements

Three series of measurements were carried out in the EfW plant. An overview of the LPR measurements is given in Table 8.4. For each series of measurements new electrode rings were used. The working and counter electrodes were made of 15Mo3, the same material that constitutes the superheater tubes of the plant. The reference electrode was made of Inconel©. During the first two series of measurements the sensor heads were exposed to the flue gases for about 200 hours. After this time the signals dropped sharply indicating sensor failure.

Figure 8.5 and Figure 8.6 show the linear polarisation conductance (LPC) signals obtained. Once stationary conditions are reached the LPC signals are proportional to the corrosion rates of the rings. The relationship between the LPC and the corrosion rate was explained in detail in chapter 6. The symbol for the LPC is G and its unit is mA/V. The diagrams show two signals: one from the upper and one from the lower sensor.

Table 8.4: Overview of the LPR measurements in the EfW plant

Series of measurements		Series of measurements 1	Series of measurements 2	Series of measurements 3
Exposure time		~300 h	~300 h	~1200 h
Parameters investigated:				
Flue gas temperature				X
Sensor temperature				X
Waste composition				X
Explosive cleanings				X
Metallographic analysis of the rings	Upper sensor	X		X
	Lower sensor	X	X	X

The curves obtained have a similar shape to those from the small-scale measurements and to those obtained in other plants (an overview of LPR measurements carried out in other EfW plants can be found in [21]). Two distinct regions of the graphs can be discerned. In the first the LPC increases sharply (always starting from zero) for a period of 100 to 200 hours and then in the second region the gradient of the curve decreases and shows a fluctuating behaviour. The first period is related to the electrolyte formation already explained in chapter 6. There the duration of this period was called τ. During this period the effect of the electrolyte's resistance cannot be neglected and therefore the polarisation conductance measured cannot be assumed to be proportional to the corrosion rate.

In the second period the signal can be assumed to be proportional to the corrosion rate of the rings. As can be seen in Figure 8.5 and Figure 8.6 the signal of the upper sensor is always higher than that of the lower sensor. This agrees well with the corrosion behaviour observed in the superheaters of the plant. In the upper part of the superheater, which is exposed to higher flue gas temperatures, the metal losses measured are higher than in the middle and lower parts. The conductance values for this period fluctuate between 75 and 100 mA/V for the upper sensor and between 25 and 50 mA/V for the lower sensor. These values are high when compared to those measured in other plants [21]. However the comparison of conductances allone does not suffice to determine the difference in corrosion rates since the calibration factors (the proportionality constants between conductance and corrosion rate) may vary between plants.

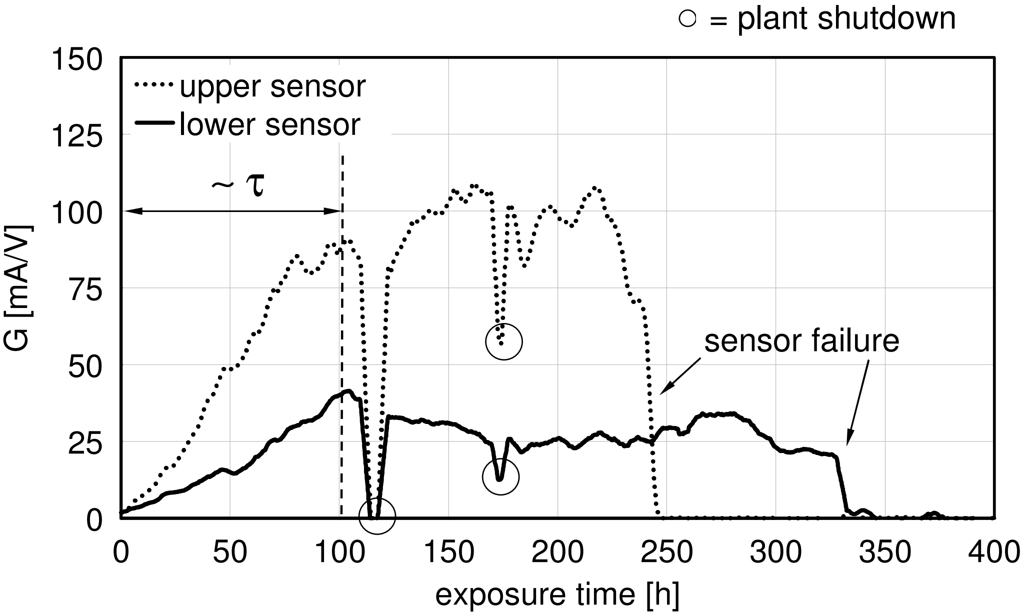

Figure 8.5: LPC signals for the first series of measurements (T_{tube} = 380 °C; $T_{flue\ gas}$ ~ 850 °C (upper sensor); $T_{flue\ gas}$ ~ 650 °C (lower sensor))

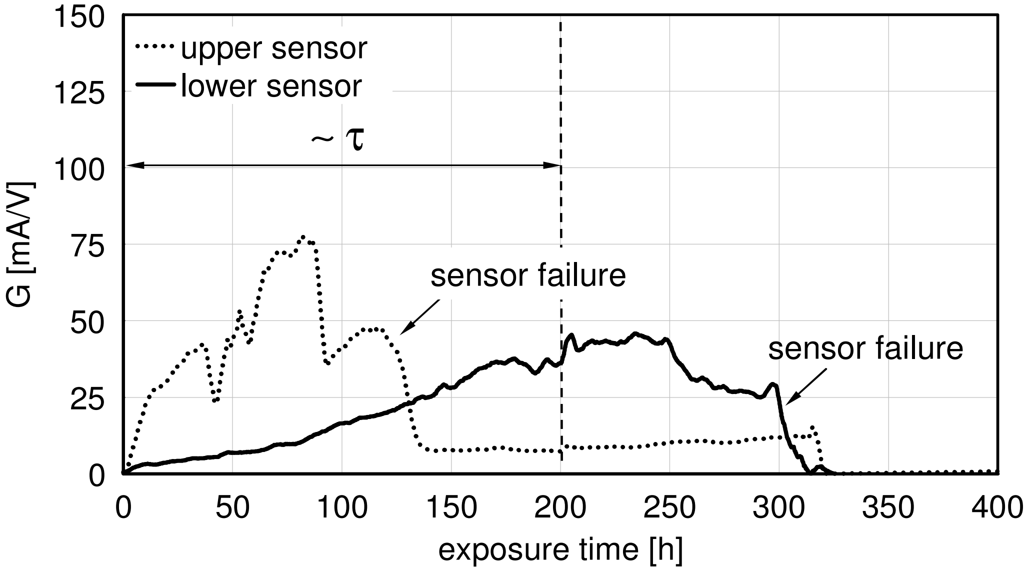

Figure 8.6: LPC signals for the second series of measurements (T_{tube} = 380 °C; $T_{flue\ gas}$ ~ 850 °C (upper sensor); $T_{flue\ gas}$ ~ 650 °C (lower sensor))

In these Figures the effect of plant shutdowns can be seen. In the case of a shutdown the signal drops sharply. The decrease in the LPC signal depends on the temperature decrease in the plant. As soon as the plant restarts its operation the signal returns to the values it had before the interruption. The reaction time of the signal in these cases is very short (< 2 hours).

For the third series of measurements optimised sensor heads were used and the exposure time was increased to more than 1200 hours without sensor failure. The LPC obtained is shown in Figure 8.7. Taking into consideration only the period where the signal is proportional to the corrosion rate (t > τ), one can identify zones of increasing and decreasing corrosion rate. This indicates that the corrosion of the superheaters in the plant is not constant and it may be influenced by the operational conditions in the plant (waste composition, load increase/decrease, etc.). In a later section the influence of some of the plant parameters will be studied in detail. The signal of the upper sensor is always higher than the signal of the lower sensor but the two signals do not vary in the same way (the graphs have different shapes). This is because the corrosive conditions at the two sensors' positions have different dynamics. In this period the reaction of the LPC signal to plant shutdowns corresponds to that observed in the previous series of measurements.

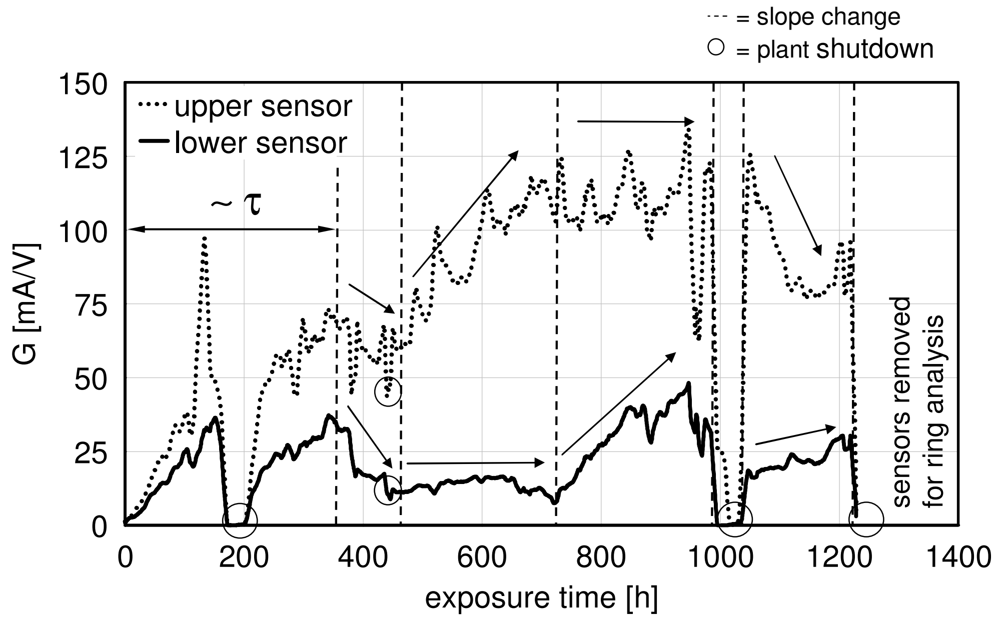

Figure 8.7: LPC signals for the third series of measurements (T_{tube} = 380 °C; $T_{flue\ gas}$ ~ 850 °C (upper sensor); $T_{flue\ gas}$ ~ 650 °C (lower sensor))

After 1200 hours of exposure the sensors were removed from the plant for metallographic analysis. Their weight loss is used in the next section to calculate the calibration factors.

The weight loss of the rings was measured and converted into an average thickness loss. The average thickness loss for the upper sensor was 1.3 mm and for the lower sensor 0.8 mm (exposure time ~ 1200 hours). With these values the calibration factors can be calculated according to equation Eq. 18 in section 6. The calibration factors obtained for this period are $0.9\cdot10^{-8}$ mV/(As) for the lower sensor and $0.37\cdot10^{-8}$ Vm/As for the upper sensor. These calibration factors are slightly lower than the calibration factors obtained in previous measurements with the same LPR sensor. Figure 8.8 shows the corrosion signal obtained from the measured LPC signal and the calculated calibration factors.

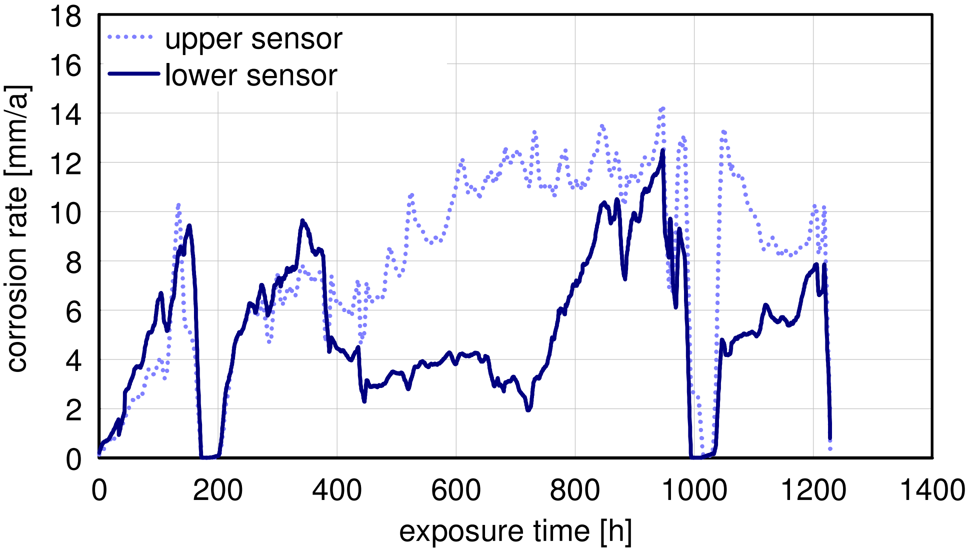

Figure 8.8: Corrosion rate measured in the third series of measurements
(T_{tube} = 380 °C; $T_{flue\ gas}$ ~ 850 °C (upper sensor); $T_{flue\ gas}$ ~ 650 °C (lower sensor))

The corrosion rate varies from 4 to almost 14 mm/a. The corrosion signals of the two sensors are very similar to start with. After 400 hours of exposure the corrosion rate decreases to values around 4 mm/a for the lower sensor whereas the upper sensor's signal increases to values around 14 mm/a. After 500 hours the lower signal increases to values similar to those of the upper sensor with a gradient close to the initial slope. These corrosion rates are very high, much higher than the corrosion rates calculated from the measurements of the plant wall's thickness.

There are some differences between the conditions near the corrosion sensors and the conditions near the superheaters:

- The superheaters in this plant are protected from the flow of flue gas by a metal plate while the sensors are directly exposed to it.
- The corrosion sensors are located between the superheaters where the air flow is very different to that within the superheater bench.
- The sensor heads are perpendicular to the direction of the gas flow while the superheater tubes are parallel to it.

These differences among others may be responsible for the different corrosion rates observed.

If the corrosion rate inferred from the LPC signal is integrated over the exposure time, the thickness loss is obtained as a function of the exposure time, see Figure 8.9.

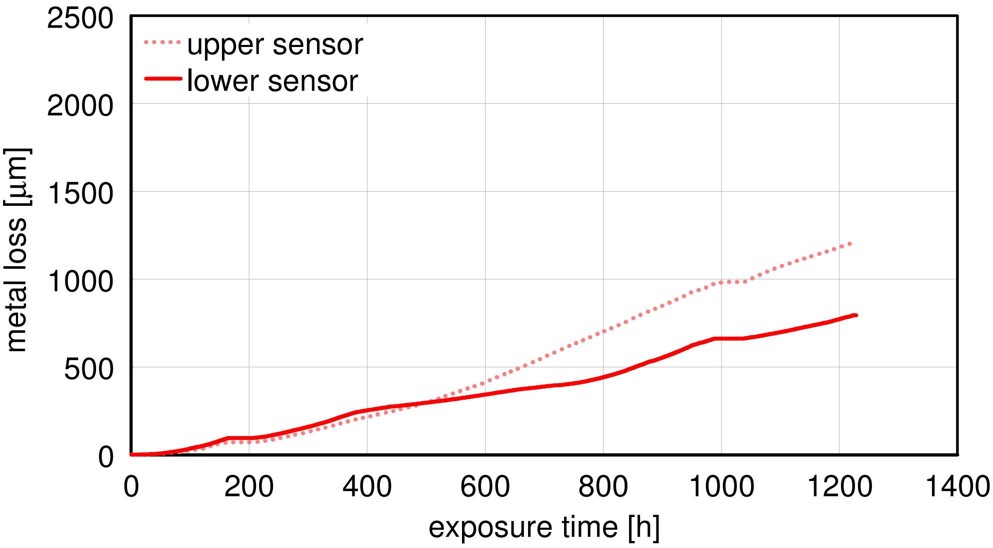

Figure 8.9: Metal loss measured in the third series of measurements
(T_{tube} = 380 °C; $T_{flue\ gas}$ ~ 850 °C (upper sensor); $T_{flue\ gas}$ ~ 650 °C (lower sensor))

The final values of the two curves are 1.5 mm and 0.8 mm. They coincide with the thickness loss measured on the rings. The shutdowns of the facility can easily be identified as the periods where the thickness loss keeps a constant value (after around 200 and 1000 hours of exposure).

8.4.1 Correlation of the LPC signal with operational parameters

Within the framework of this project the influence of different operational parameters on the corrosion signal was investigated. The conditions at the plant were not as accurately determined and could not be monitored as precisely as in the small-scale facility. The correlation of the selected parameters with the corrosion signal is described below.

Flue gas temperature: Flue gas temperature is known to have a decisive influence on the corrosion rate. During all the series of measurement a good correlation between the flue gas temperature and the corrosion signal was observed. The corrosion signal of the upper sensor, exposed to higher flue gas temperatures, was always higher than that of the lower sensor. Figure 8.10 shows the LPC signal as function of glue gas temperature downstream of the superheaters.

The flue gas temperature downstream of the superheater is the operational parameter that correlates best with the measured corrosion rates. The shape of the corrosion signals can be explained by the flue gas temperature measured. The steady increase of the corrosion rate recorded by the upper sensor is parallel to the increase in the flue gas temperature measured downstream of the superheaters. In the case of the lower sensor there are regions where this parallel behaviour is observed but there are also some disagreements that cannot be fully explained. There is a sharp decrease of the corrosion signal at t ~ 380 h and a sharp increase at t ~ 720 h that cannot be fully explained from the measured flue gas temperature.

Waste composition: The composition of the waste is responsible for the amount of corrosive species in the flue gases. Although the composition was not known, it was assumed to be more corrosive than MSW. The amount of hospital waste burnt was not measured directly and could only be estimated roughly by the number of wagons with hospital waste processed per day and their average weight.

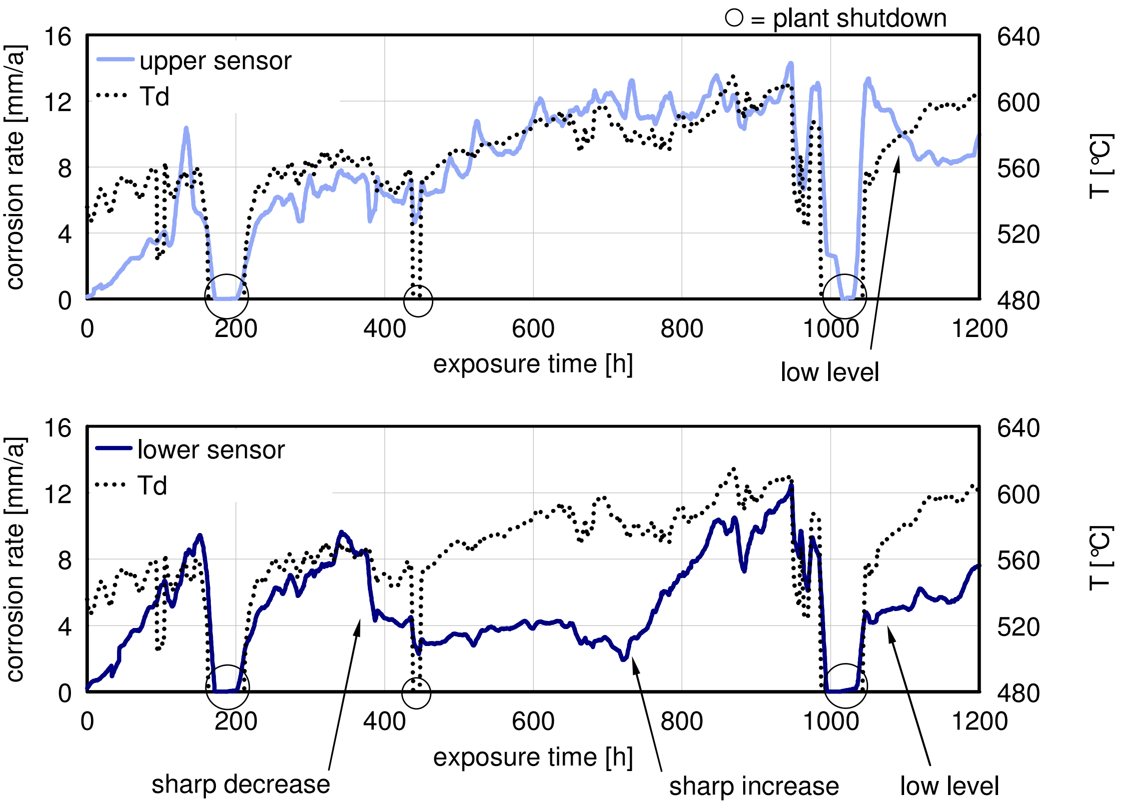

Figure 8.10: Influence of the flue gas temperature downstream of the superheaters T_d on the corrosion signal (T_{tube} = 380 °C; $T_{flue\ gas}$ ~ 850 °C (upper sensor); $T_{flue\ gas}$ ~ 650 °C (lower sensor))

Figure 8.11 shows the corrosion signal and the amount of hospital waste burnt. During this period of time the number of wagons with hospital waste processed varied from almost zero up to the maximum value, but no significant correlation is discernable between the amount of hospital waste and the corrosion signal. Either there is indeed no relevant correlation or the number of wagons with hospital waste included in the daily fuel charges is not a good indicator of the waste composition. The weight of the wagons as well as the composition of the hospital waste may vary too much.

Tube temperature: The temperature of the sensor was increased from 380 °C to 415 °C during a period of approximately two hours in order to observe the influence of this parameter on the corrosion signal. Figure 8.12 shows the resulting corrosion signal. If the sensor temperature is increased by approximately 10% (35 °C) the corrosion signal increases from 7 to 8.5 mm/a on the upper sensor and from 6 to 7.5 mm/a on the lower sensor. This means an increase in corrosion rate of around 30%.

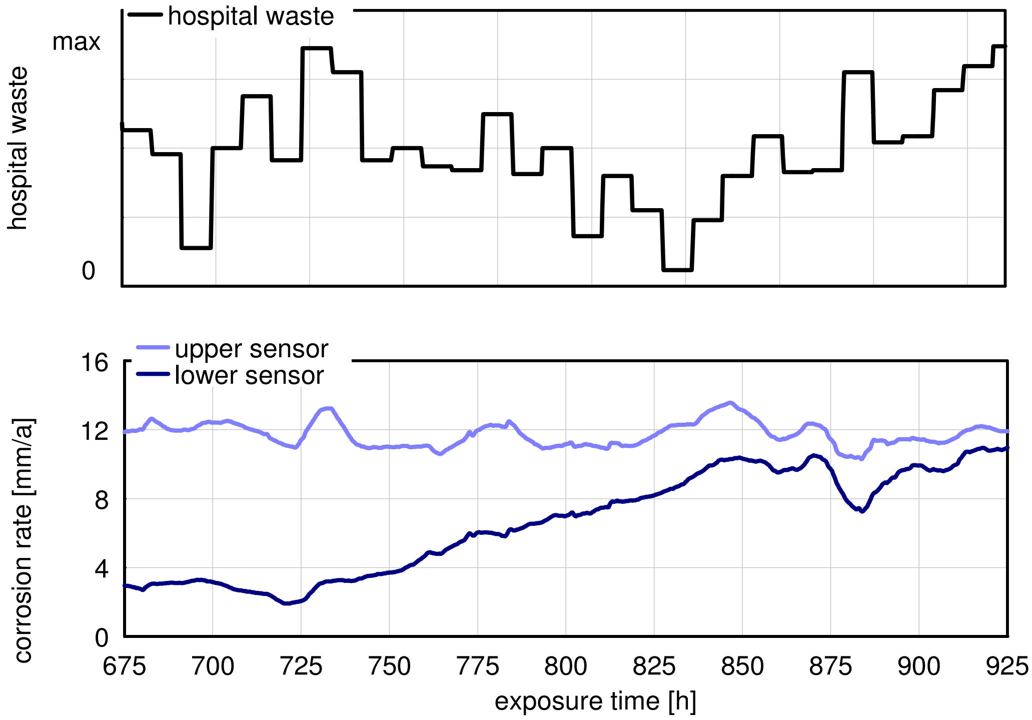

Figure 8.11: Influence of the waste composition on the corrosion signal

(T_{tube} = 380 °C; $T_{flue\ gas}$ ~ 850 °C (upper sensor); $T_{flue\ gas}$ ~ 650 °C (lower sensor))

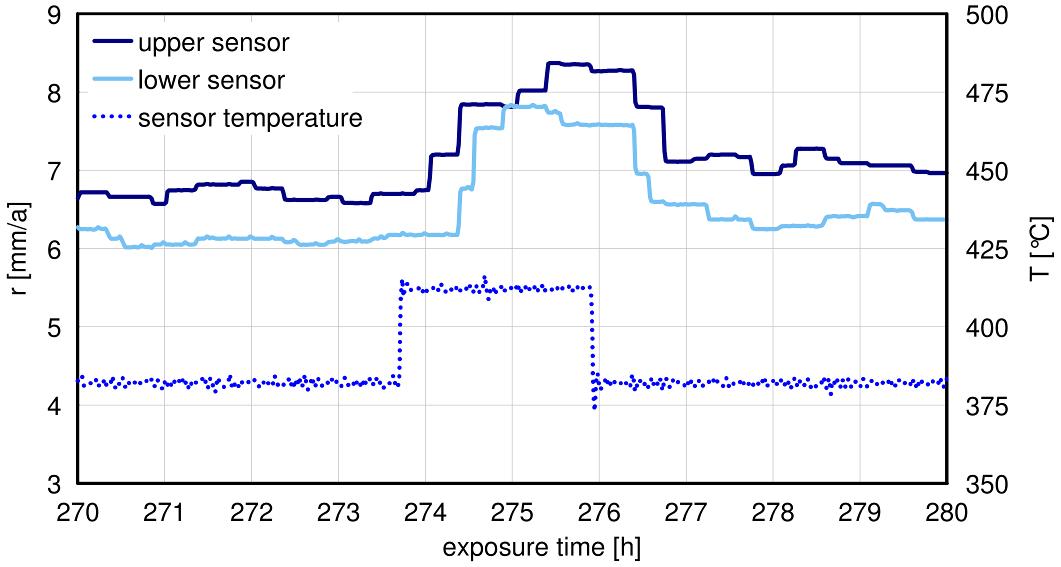

Figure 8.12: Influence of the tube temperature on the corrosion signal

($T_{flue\ gas}$ ~ 850 °C (upper sensor); $T_{flue\ gas}$ ~ 650 °C (lower sensor))

Explosive cleaning: in Figure 8.13 the explosive cleanings carried out at the plant during the series of measurements have been included. It can be seen that the explosive cleanings are responsible for the varying behaviour of the corrosion signals already observed in Figure 8.7 and Figure 8.10. After each explosion the slope of the corrosion signals changes. The effect of the explosive cleaning on the lower sensor is stronger than on the upper sensor. Additionally it can be seen that the retraction of the lower sensor during the explosions changes their effect on the measured signal. When the sensor was retracted the signal decreased while if the sensor was not retracted the signal increased with a gradient similar to that of the first hours of exposure.

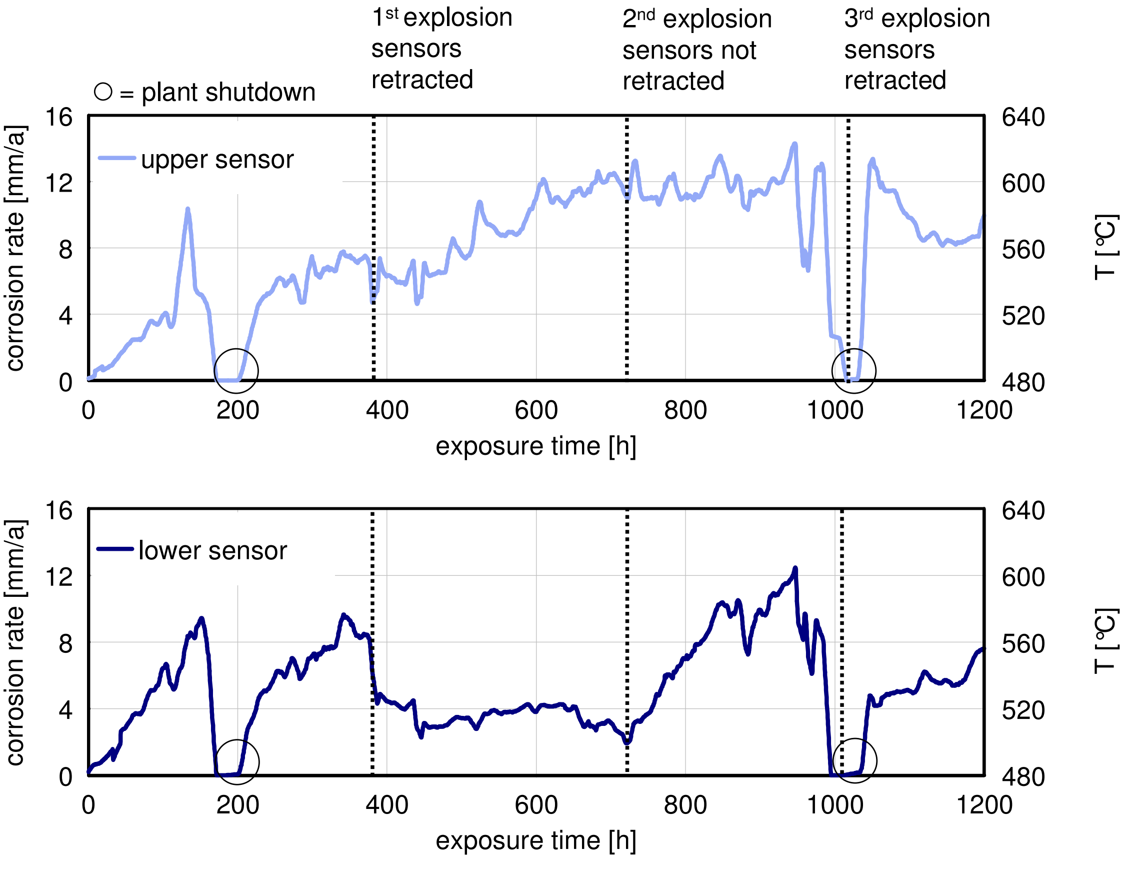

Figure 8.13: Influence of explosive cleaning on the corrosion signal (T_{tube} = 380 °C; $T_{flue\ gas}$ ~ 850 °C (upper sensor); $T_{flue\ gas}$ ~ 650 °C (lower sensor))

The aim of the explosive cleanings is to remove the deposits accumulated on the heat exchangers' surfaces in the convective zone. The changes that the explosive cleanings bring about on these surfaces seem to have a decisive influence on the corrosion rates measured. The monitoring of the deposits and the effect the explosive cleanings have on them (for instance by means of a camera) is thus indispensable in order to understand the behaviour of the corrosion signals and is recommended for future series of measurements.

8.4.2 Metallographic analysis of the LPR sensor's rings

The metallographic analysis of the rings supplied valuable information on the structure of the deposits and oxide layers and the main chemical species involved. The Institute for Experimental Physics I and II of the Augsburg University carried out SEM and EDX analyses of the probes and investigated the morphology and composition of the scales built on the rings. The pictures of the rings from the first series of measurements are shown in Figure 8.14. In the micrographs a well-defined iron chloride layer (thickness ~ 500 μm) can be observed for both lower and upper sensor. Close to the chloride layer there is a thin sulphur-rich layer (thickness ~ 100 μm) followed by an iron oxide layer of about 1 mm thickness. On this layer a mixture of iron oxides with S, Cl and alkalis (mainly Na, Ca and K) is found. Similar structures were described in the introduction and have been observed in other energy-from-waste plants [21].

In the second series of measurements a similar structure is found with more K and Ca and almost no Na, see Figure 8.15.

Figure 8.16 shows the SEM and EDX pictures for the third series of measurements along with information from EDX analysis. In this case the rings were exposed to the flue gases for more than 1200 hours. For the upper sensor a well-defined chloride layer of between around 300 μm (windward side) and 500 μm (lee side) is found. It is followed by a thin sulphur layer and a matrix of iron oxides mixed with S and alkalis. In this case K and Ca are the predominant alkali species and very little Na is present.

On the lower sensor the chloride layer is much thinner (~ 100 μm) and no well-defined sulphur layer is found (see Figure 8.17). A matrix of iron oxides mixed more or less homogeneously with S, K and Na follows the chloride layer. The stratified structure of the deposits shown in these pictures may indicate irregular conditions near the probe. A more detailed description of the metallographic analysis as well as additional information about the corrosion signals obtained in this project can be found in the PhD Thesis of Maisch [22] as well as in [102].

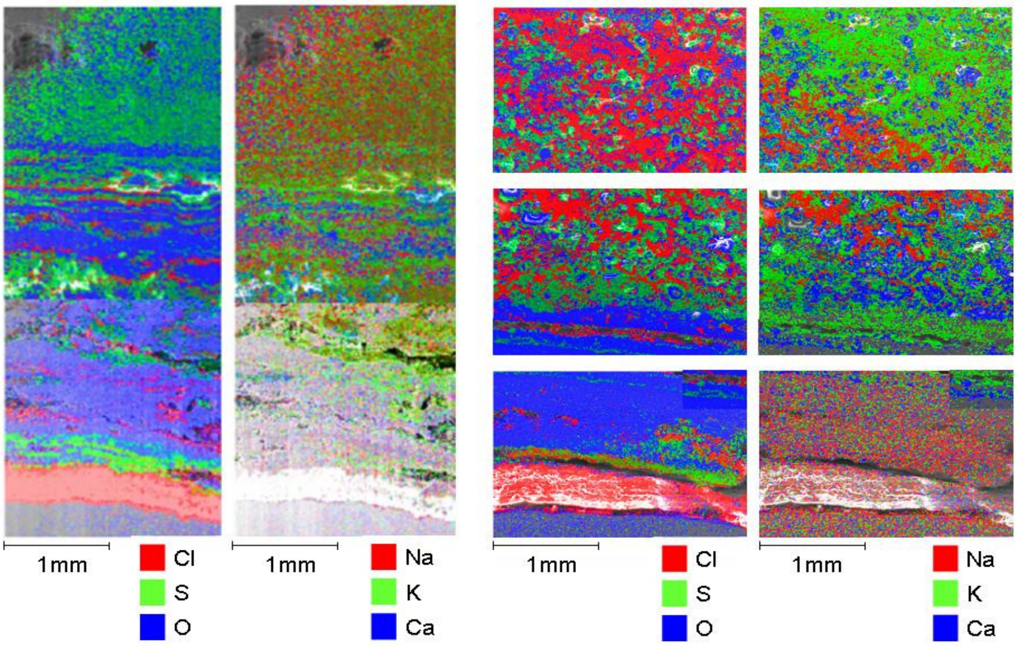

Figure 8.14: SEM and EDX pictures after the first series of measurements; upper sensor (left) and lower sensor (right) (T_{tube} = 380 °C; $T_{flue\ gas}$ ~ 850 °C (upper sensor); $T_{flue\ gas}$ ~ 650 °C (lower sensor))

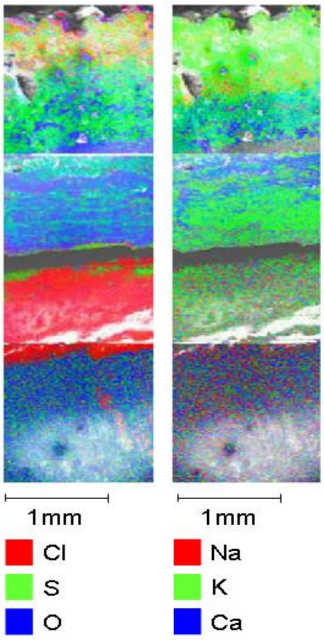

Figure 8.15: SEM and EDX pictures of the rings after the second series of measurements; lower sensor (T_{tube} = 380 °C; $T_{flue\ gas}$ ~ 650 °C)

Images prepared by the Institute for Experimental Physics I and II Augsburg University

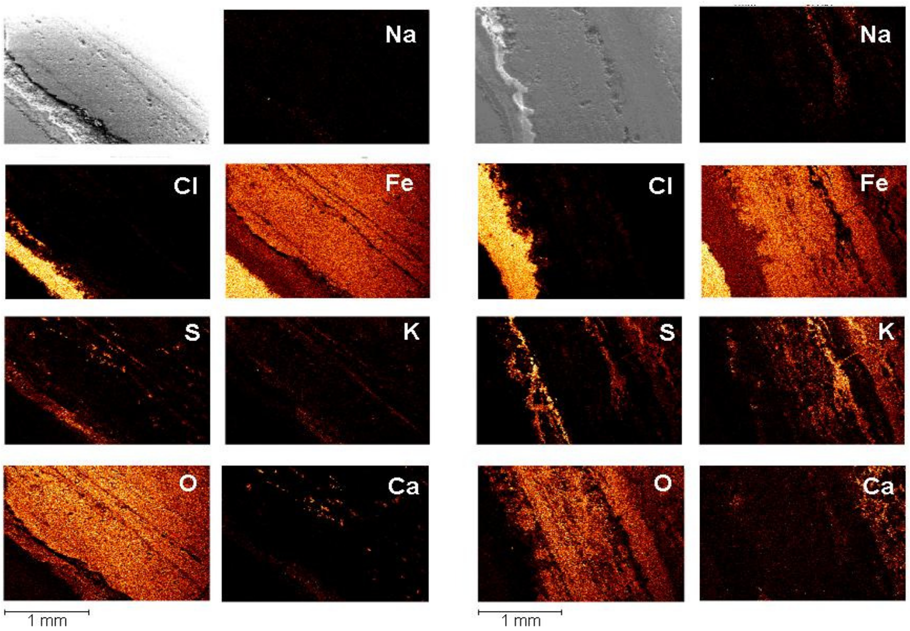

Figure 8.16: SEM and EDX pictures of the rings after the third series of measurements; upper sensor; windward side (left) and lee side (right) (T_{tube} = 380 °C; $T_{flue\ gas}$ ~ 650 °C)

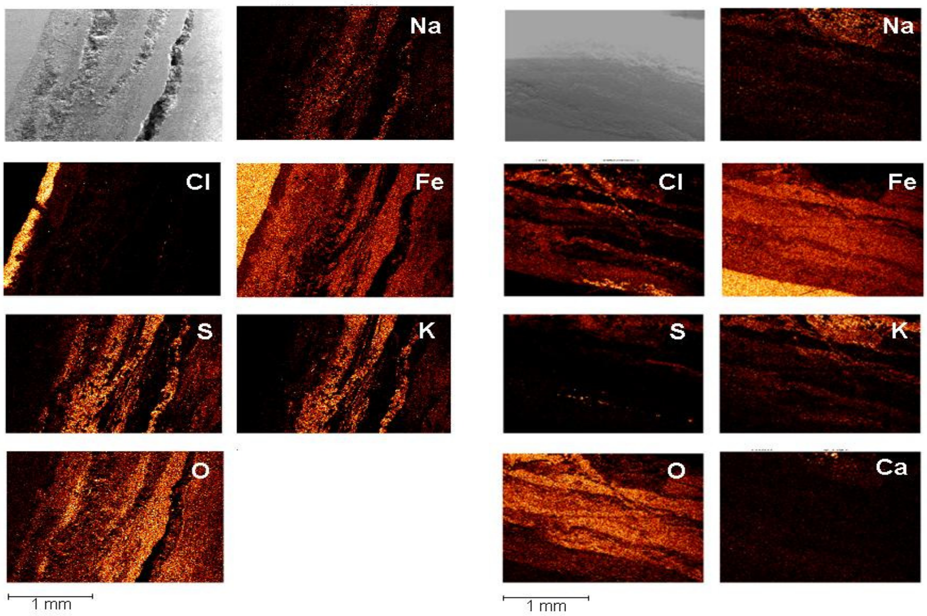

Figure 8.17: SEM and EDX pictures of the rings after the third series of measurements; lower sensor; windward side (left) and lee side (right) (T_{tube} = 380 °C; $T_{flue\ gas}$ ~ 850 °C)

Images prepared by the Institute for Experimental Physics I and II Augsburg University

8.4.3 Comparison of the LPR measurements in small-scale facilities with those in a power plant

The short-term behaviour (first 8 hours) of the signal obtained in the power plant is compared with the corrosion signal from the small-scale tests in Figure 8.18. The signal obtained in the plant is about one order of magnitude higher but the shape of both signals is similar.

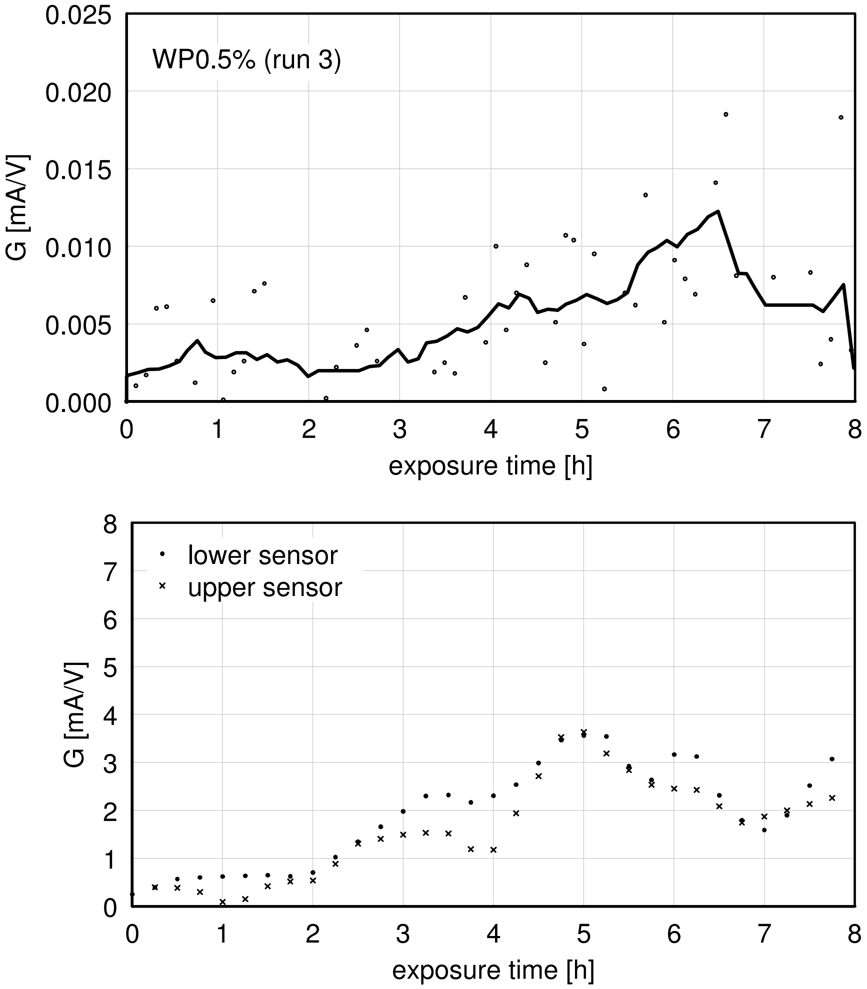

Figure 8.18: Comparison of the short-term behaviour of the measured conductance in the small-scale tests (top) and the power plant tests (bottom)

The restricted control of measurement conditions at the power plant limited the study of the correlation between the corrosion signal and the operational parameters. Reactions of the corrosion signal to changes in the waste composition were difficult to observe. This was not the case for the small-scale tests. During the tests at the small-scale facility changes in fuel composition, for instance, had a significant influence on the corrosion signal.

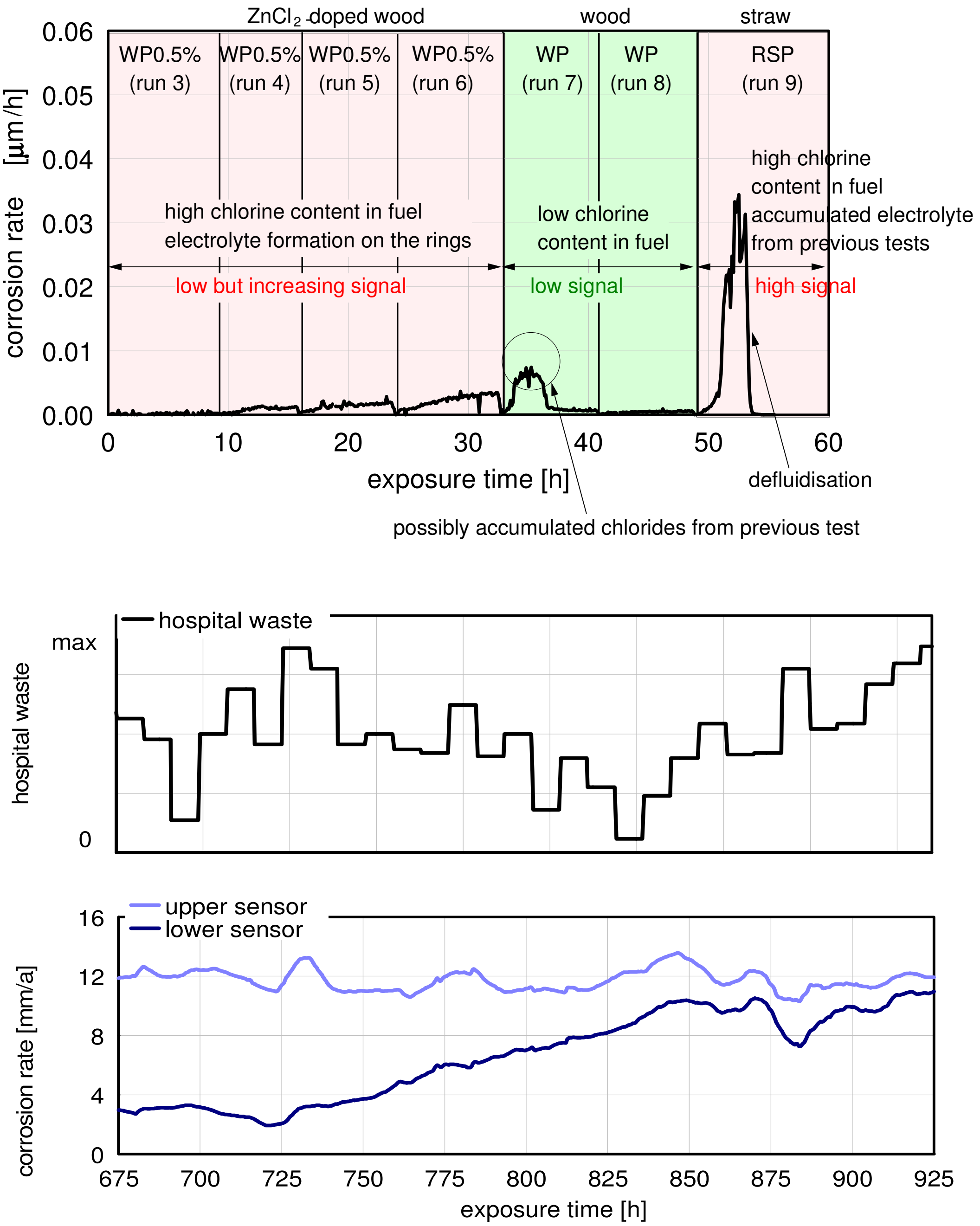

Figure 8.19: Comparison of the influence of fuel composition on the measured corrosion rates in the small-scale tests (top) and the power plant tests (bottom)

The interruption of the chlorine supply rapidly decreased the corrosion rate as shown in Figure 8.19. Both small-scale and power plant tests confirmed that the scales formed on the rings have a notable influence on the corrosion signal measured.

8.5 Summary

It can be concluded that small-scale and power plant tests complement each other in the investigation of corrosion. According to the results shown in this work the main strength of the small-scale tests is the better control and monitoring of the input parameters. During the power plant tests a good correlation of the corrosion signal with some of the operational parameters like the tube or the flue gas temperature could be measured. However the restricted control of measurement conditions at the power plant limited the study of the correlation between the corrosion signal and other important operational parameters like the waste composition. The power plant tests also confirmed that the scales formed on the rings and the processes affecting them (like explosive cleaning) have a notable influence on the corrosion signal measured and should be studied in detail.

9 Conclusions

In this research the feasibility of short-term tests (lasting up to 8 hours) to study the corrosion and agglomeration behaviour of biogenic solid fuels in a fluidised bed reactor has been investigated.

Agglomerates were formed in the bed after less than 8 hours in all of the tests with straw pellets. Melting-induced agglomerates were found in all the tests with straw, while coating-induced agglomerates were only found after the combustion of rye straw pellets and are supposed to be responsible for the defluidisation of the bed. No agglomerates were found after burning wood pellets. Although the K and Si contents of the coating was closer to that of wheat straw ashes than to that of rye straw ashes, no coating-induced agglomerates were found after the tests with wheat straw pellets. This leads one to the conclusion that the interaction between the K from the ashes and the Si from the bed particles is essential for the formation of this kind of agglomerate.

The short-term measurement of corrosion rates by means of metal loss methods (methods that measure changes in a physical property of the material due to corrosion) faced considerable limitations, even when using highly doped fuels at the highest temperatures. The short exposure time led to metal thickness losses in the order of magnitude of a few micrometers (< 5 µm) under the conditions of these tests using low alloy steels. For high alloy steels no significant corrosion was measured. Such small metal losses were difficult to quantify even with metallographic techniques.

For low alloy steels however a well-defined layer of corrosion products accumulated on the rings and the results were reproducible. The thickness of this layer was in the order of magnitude of 5 to 50 µm and could be observed and analysed very accurately. The metallographic analysis supplied an accurate description of the morphology and composition of the corrosion products and deposits. Furthermore it was shown that the corrosion products and deposits obtained in the small-scale facility were very similar to those obtained in power plants and in laboratory experiments. According to the results of this work metal loss techniques may not be adequate for the short-term measurement of corrosion rates under the conditions of these tests. However even after such short exposure times the metallographic analysis supplied useful information for the investigation of the chemical species and mechanisms involved during the first stages of corrosion.

As expected, the use of iron instead of steel led to higher thickness losses. These losses were in the order of magnitude of 5 to 25 µm and could be measured successfully with the procedure proposed in this work, yielding values about one order of magnitude higher than those found in the literature for standard high-temperature steels. However, the accuracy of the method used here was very limited. The measurements were subject to an uncertainty of about ± 5 µm, i.e. in the same order of magnitude as the lowest iron losses measured. Despite its low accuracy, the simplicity and low cost of this method make it interesting for specific applications. For instance in series of measurements with many input parameters this procedure could be used to determine the parameters most relevant for corrosion. These parameters could be then studied in more detail by performing longer tests with more accurate and expensive measuring techniques.

The electrochemical methods (methods based on the measurement of electrochemical variables) may be more suitable for the short-term measurement of corrosion. The monitoring technique used in this work involved the measurement of linear polarisation resistance. Online corrosion signals were successfully obtained in all the tests. However, the signals did not reach a stationary value in the 8-hour tests. The shape of the signal was similar to that obtained during the first hours of the tests in commercial plants but the signal values were about two orders of magnitude lower. In this work the underestimation of the corrosion rate is attributed to an incomplete electrolyte formation between the rings within the short time in which the sensor is exposed to the corrosive environment. The formation of the electrolyte is necessary for the measured linear polarisation resistance to correspond to the corrosion rate. If the electrolyte is not completely formed, an additional ohmic resistance supplements the linear polarisation resistance. Not taking the additional resistance (which is difficult to measure) into account results in an underestimation of the corrosion rate.

Nonetheless, the signals from the 30 h tests supplied valuable information for the study and quantification of this underestimation. In this work an approach was presented for the interpretation of the results based on theoretical considerations and experimental data. It was shown that this interpretation is consistent with measured and expected values and that the initial underestimation can be explained well in terms of the electrolyte's ohmic resistance. Based on this interpretation it is estimated that the LPR measurements may need at least 50 hours in order to produce a stationary signal proportional to the corrosion rate under the conditions of these tests.

The results of these tests presume that for the short-term measurement of corrosion with the LPR technique, the electrolyte's ohmic resistance must be measured. Furthermore the use of a high polarisation for the measurement of this resistance and the consequently correction of the corrosion signal initial underestimation is proposed in this work.

Another important limitation of this approach is that reliable calibration factors could not be calculated. The corrosion signal is not obtained directly. The signals obtained must be calibrated using the measured metal loss of the rings. As already explained, the short exposure time is responsible for very low metal losses that are difficult to measure.

In spite of these limitations the short-term measurements carried out in this work provided experimental evidence for the following observations:

- Corrosion only occurred when the probe was exposed to combustion gases. Even if the probe was already covered with corrosive deposits the corrosion signal only started to increase when combustion began and decreased to zero as soon as combustion was stopped. This confirms previous observations made with this kind of sensor in [21]. The interaction between deposits and flue gas is necessary for the corrosion reaction to continue.

- In the small-scale facility the LPC signal reacted to changes in the flue gas composition. When the other parameters are kept constant, changing the fuel affects the corrosion signal. The use of chlorine-rich fuels resulted in higher signals than those obtained with fuels containing less chlorine.

LPR measurements were also carried out in a EfW plant. The corrosion signals obtained were much higher than in the small-scale plant. The higher the flue gas temperature was, the higher was also the corrosion signal measured. A good correlation was observed between the measured corrosion signal and the corrosion probe temperature. Changes in the fuel composition could not be correlated with changes in the corrosion signal.

However, these tests confirmed that the scales formed on the ring have a significant influence on the measured corrosion signal. Their removal seemed to be one of the main causes of changes in the corrosion signal.

The experiments carried out in this work show that the LPR monitoring technique has a great potential for the short-term investigation of corrosion. For future series of measurements two approaches could be pursued: (1) longer exposure times than the ones tested in this work. Longer tests (~ 50 h) should be carried out in order to determine exactly how long the signal takes to reach a stationary value. In this case the small-scale facility is required to operate automatically. Once the optimal duration of the tests has been determined, the influence of the different parameters could be studied in detail. (2) An alternative approach would be to further develop the measuring technique so that the initial underestimation could be quantified and corrected. In this case it would not be necessary to prolong the tests carried out in this work (or similar ones) in order to accurately measure corrosion rates.

In conclusion, electrochemical monitoring techniques offer promising prospects for the short-term study of the corrosion behaviour of biomass and waste fuels. For short-term measurements the electrolyte’s ohmic resistance plays an important role and must be studied as well. Otherwise the duration of the tests must be long enough for this resistance to become negligible. Though the quantification of corrosion is limited by the high uncertainty in the calibration factors, this method has the advantage of making it possible to measure the signal’s reaction to changes in the input parameters in real-time, a fact that was successfully demonstrated in this work.

Bibliography

[1] U.S. Energy Information Administration; *International Energy Outlook*, 2010.

[2] U.S. Energy Information Administration. *Long Term Oil Supply (A Resource Base/Production Path Analysis)*. (2000). Last access: 2010.10.13. Available from: http://www.eia.doe.gov/pub/oil_gas/petroleum/presentations/2000/long_term_supply/index.htm.

[3] Intergovernmental panel on climate change; *IPCC Fourth Assessment Report: Climate Change*, 2007.

[4] United Nations Framework Convention on Climate Change. (2010). Last access: 20.08.2010. Available from: http://unfccc.int/.

[5] European Commission; *Communication from the commission: Europe 2020, a strategy for smart, sustainable and inclusive growth*. 2010.

[6] European Union; *Directive 2009/28/EC of the European Parliament of the Council of 23 April 2009 on the promotion of the use of energy from renewable sources and amending and subsequently repealing Directives 2001/77/EC and 2003/30/EC*. 2009.

[7] Mantzos, L. and Capros, P.; *European Energy and Transport. Trends to 2030*, Institute of communication and computer systems of national technical university of Athens. Directorate General for Enery and Transport. European Commission, 2005.

[8] Bundesministerium für Umwelt Naturschutz und Reaktorsicherheit; *Erneuerbare Energien in Zahlen. Nationale und internationale Entwicklung*. 2010.

[9] *VGB Forschungsprojekt Nr. 302. Untesuchung von Biomasse- und Altholzheizkraftwerken im Leistungsbereich von 5 bis 20 MWel zur Verbesserung der Wirtschaftlichkeit (Teil 1)*.

[10] European Energy Exchange. *EEX Transparency energy markets*. Last access: 26.08.2010. Available from: http://www.transparency.eex.com/de-/daten_uebertragungsnetzbetreiber/stromerzeugung/.

[11] Schirmer, M.; *Betriebstechnische Erfahrungen im Holz-Heizkraftwerk Dresden*. Proceedings of the conference: *VDI Wissensforum: Beläge und Korrosion, Verfahrenstechnik und Konstruktion und Großfeuerungsanlagen VDI 430507*. Frankfurt am Main, 2009.

[12] ISO 8044: *Corrosion of metals and alloys - Basic terms and definitions*, 1999.

[13] NIELSEN, H.P.; FRANDSEN, F.J.; DAM-JOHANSEN, K. and BAXTER, L.L.; *The implications of chlorine-associated corrosion on the operation of biomass-fired boilers.* Progress in Energy and Combustion Science, 2000. 26: p. 283-298.

[14] SPLIETHOFF, H.; *Power generation from solid fuels.* München. Springer Verlag, 2010. - ISBN 978-3-642-02855-7

[15] BAKKER, W.T.; *The effect of deposits on waterwall corrosion in fossil fueled boilers.* Materials at high temperatures, 2003. 20(2): p. 161-168.

[16] WARNECKE, R.; *Einfluss von Strömung und chemischen Reaktionen in rauchgasseitigen Belag auf Korrosion an Überhitzer-Rohren in Müllverbrennungsanlagen.* VGB PowerTech, 2004. 9(-): p. 52-59.

[17] HERZOG, T.; *Belagsentwicklung und Korrosion aus Dampferzeugerrohren bei der Verbrennung von Abfällen und Biomasse*. Freiberg. TU Bergakademie Freiberg, 2007. Dissertation. - ISBN 978-3-86012-321-8

[18] FOSTER, N.A.; DRÄGER, R.; DAUBLEBSKY VON EICHHAIN, C. and WARNECKE, R.; *Wärmetechnische Auslegung von Kesseln für Verbrennung von Reststoffen-Grundlagen und Korrosionsdiagramm*. Proceedings of the conference: *VDI Wissensforum: Beläge und Korrosion, Verfahrenstechnik und Konstruktion in Großfeuerungsanlagen VDI 430507*. Frankfurt am Main, 2007.

[19] GRABKE, H.; *Incinerating municipal and industrial waste.* Bryers RW, 1989: p. 161.

[20] HORN, S.; HAIDER, F.; WALDMANN, B. and WARNECKE, R.; *Transport der Schadstoffe zur Korrosionsfront- Modell für die Korrosion im Bereich 300°C bis 500°C Rohrwandtemperatur*. Proceedings of the conference: *VDI Wissensforum: Beläge und Korrosion, Verfahrenstechnik und Konstruktion in Großfeuerungsanlagen VDI 430507*. Frankfurt am Main, 2007.

[21] WALDMANN, B.; *Korrosion in Anlagen zur thermischen Abfallverwertung: elektrochemische Korrosionserfassung und Modellbildung*. Augsburg. Mathematisch- Naturwissenschaftliche Fakultät. Universität Augsburg, 2007. Dissertation.

[22] MAISCH, S.; *Identifikation und Quantifizierung von Korrosionsrelevanten Parametern in Müllverbrennungsanlagen mittels Charakterisierung der deponierten Partikel und Elektrochemischer Online-Messungen*. Institut für Physik, Lehrstuhl für Experimentalphysik II, University of Augsburg, 2011.

[23] SCHROER, C. and KONYS, J.; *Rauchgasseitige Hochtemperatur-Korrosion in Müllverbrennungsanlagen. Ergebnisse und Bewertung einer Literaturrecherche.* Technik und Umwelt Wissenschaftliche Berichte, Karlsruhe Forschungszentrum Karlsruhe GmbH, 2002.

[24] GUPTA, R.P.; WALL, T.F.; BAXTER, L.; SALMENOJA, K.; HUPA, M. and BACKMAN, R., *Laboratory Studies on the Influence of Gaseous HCl on Superheater Corrosion*, in *Impact of Mineral Impurities in Solid Fuel Combustion*. Springer US, 1999. p. 513-523.

[25] KAWAHARA, Y.; *High temperature corrosion mechanisms and effect of alloying elements for materials used in waste incineration environment.* Corrosion Science, 2002. 44(2): p. 223-245.

[26] KRAUSE, H.H.; *Assessment of Factors Affecting Boiler Tube Lifetime in Waste-Fired Steam Generators: New Opportunities for Research and Technology Development*, Ohio, National Renewable Energy Laboratory, 1996.

[27] WARNECKE, R.; *Beläge und Korrosion, Verfahrenstechnik und Konstruktion in Chlor-belasteten thermischen Anlagen*. Proceedings of the conference: *VDI Wissensforum: Beläge und Korrosion, Verfahrenstechnik und Konstruktion in Großfeuerungsanlagen*. Frankfurt am Main, 2007.

[28] SKRIFVARS, B.J.; BACKMAN, R.; HUPA, M.; SALMENOJA, K. and VAKKILAINEN, E.; *Corrosion of superheater steel materials under alkali salt deposits Part 1: The effect of salt deposit composition and temperature.* Corrosion Science, 2008. 50(5): p. 1274-1282.

[29] SKRIFVARS, B.J.; WESTÉN-KARLSSON, M.; HUPA, M. and SALMENOJA, K.; *Corrosion of super-heater steel materials under alkali salt deposits. Part 2: SEM analyses of different steel materials.* Corrosion Science. 52(3): p. 1011-1019.

[30] JENSEN, P.A.; FRANDSEN, F.J.; DAM-JOHANSEN, K. and SANDER, B.; *Experimental Investigation of the Transformation and Release to Gas Phase of Potassium and Chlorine during Straw Pyrolysis.* Energy & Fuels, 2000. 14(6): p. 1280-1285.

[31] JENSEN, P.A.; FRANDSEN, F.J.; HANSEN, J.; DAM-JOHANSEN, K.; HENRIKSEN, N. and HORLYCK, S.; *SEM Investigation of Superheater Deposits from Biomass-Fired Boilers.* Energy & Fuels, 2004. 18(2): p. 378-384.

[32] SPIEGEL, M. and GRABKE, H.; *Hochtemperaturkorrosion des 2.25Cr-1Mo-Stahls unter simulierten Müllverbrennungsbedingungen.* Materials and Corrosion, 1995. 46(-): p. 121-131.

[33] SPIEGEL, M.; ZAHS, A. and GRABKE, H.; *Fundamental aspects of chlorine induced corrosion in power plants.* Materials at high temperatures, 2003. 20(2): p. 153-159.

[34] BROSSARD, J.M.; CHAUCHERIE, X.; NICOL, F. and MORIN, R.; *Superheater fireside corrosion mechanisms in WtE facilities. Lab-scale and on field results*. Proceedings of the conference: *6th Beacon Conference. ISWA*. Malmö (Sweden), 2009.

[35] SCHÜTZE, M.; MALESSA, M.; ROHR, V. and WEBER, T.; *Development of coatings for protection in specific high temperature environments.* Surface and Coatings Technology, 2006. 201(7): p. 3872-3879.

[36] SPIEGEL, W.; *Belagsgeschichten*. Proceedings of the conference: *Rauchgasseitige Damferzeugerkorrosion*. Freiberg, 2005.

[37] SPIEGEL, W.; HERZOG, T.; MAGEL, G.; MÜLLER, W. and SCHMIDL, W.; *Dynamische chlor-induzierte Hochtemperaturkorrosion von Verdampfer-*

und Überhitzerbauteilen aufgrund spezieller Belagsentwicklungen - Häufiger Befund in Abfall- und Biomasse-gefeuerten Dampferzeugern. . VGB PowerTech, 2005. 1/2: p. 89-97.

[38] BORN, M.; *Rauchgasseitige Dampferzeugerkorrosion*, ed. Saxonia. Freiberg 2005. - ISBN 3-934409-27-X

[39] DEAN, S.W.; *Overview of Corrosion Monitoring in Modern Industrial Plants.* Proceedings of the conference: *Nondestructive Testing and Electrochemical Methods of Monitoring Corrosion in Industrial Plants.* Montreal Canada, 1986.

[40] HEIKINHEIMO, L.; LAHDENPERÄ, K. and SANDLIN, S.; *Monitoring of oxidation of metals in gas environments for energy production.* Corrosion Science, 2003. 45(-): p. 2143-2161.

[41] LINJEWILE, T.M.; VALENTINE, J.; DAVIS, K.A.; HARDING, N.S. and COX, W.M.; *Prediction and real-time monitoring techniques for corrosion characterisation in furnaces.* Materials at high temperatures, 2003. 20(2): p. 175-183.

[42] KEMA. Last access: 28.02.2010. Available from: http://www.kema.com/services/consulting/Reliability/plant_reliability/fireside-corrosion.aspx.

[43] DAVIS, K.A.; LINJEWILE, T.M.; GREEN, G.C.; COX, W.M.; CARR, R.N. and HARDING, N.S.; *Evaluation of an On-line Technique for Corrosion Characterization in Furnaces*, 2001.

[44] SCRIBNER, L.L.; *The measurement and correction of electrolyte resistance in electrochemical tests.* Philadelphia,PA, 1990. - ISBN 0-8031-1283-1

[45] RUUD HUNIK. *Cordis-KEMCOP.* (2005). Last access: 05.01.2005. Available from: http://www.innovations-report.de/html/berichte/energie_elektrotechnik/bericht-38453.html.

[46] CAPPELN, F.V.; *Measurement of corrosion in power plant boilers*, Masnedo, Dänemark, 2002.

[47] STERN, M.; *A method for determining corrosion rates from linear polarization data.* Corrosion, 1958. 14(-).

[48] STERN, M. and GEARY, A.L.; *A Theoretical Analysis of the Shape of Polarization Curves.* Journal of the electrochemical society, 1957. 104(1): p. 56-63.

[49] *Corrmoran GmbH.* Last access: 28.08.2010. Available from: http://www.corrmoran.de.

[50] SCHETTLER, D.; GÖRNER, K.; KÖNIG, J. and MOSER, P.; *Online-Erfassung der Korrosionsneigung hochlegierter Kesselrohrwerkstoffe unter Hochtemperaturbedingungen*, Essen, Lehrstuhl für Umweltverfahrenstechnik und Anlagentechnik Universität Duisburg-Essen; RWE Power AG, Essen, 2001.

[51] OLOFSSON, G.; YE, Z.; BJERLE, I. and ANDERSSON, A.; *Bed Agglomeration Problems in Fluidized-Bed Biomass Combustion.* Ind. Eng. Chem. Res., 2002. 41(12): p. 2888-2894.

[52] LIN, W.; DAM-JOHANSEN, K. and FRANDSEN, F.; *Agglomeration in bio-fuel fired fluidized bed combustors.* Chemical Engineering Journal, 2003. 96(1-3): p. 171-185.

[53] RISNES, H.; FJELLERUP, J.; HENRIKSEN, U.; MOILANEN, A.; NORBY, P.; PAPADAKIS, K.; POSSELT, D. and SORENSEN, L.H.; *Calcium addition in straw gasification*.* Fuel, 2003. 82(6): p. 641-651.

[54] SCALA, F. and CHIRONE, R.; *An SEM/EDX study of bed agglomerates formed during fluidized bed combustion of three biomass fuels.* Biomass and Bioenergy, 2008. 32(3): p. 252-266.

[55] NUUTINEN, L.H.; TIAINEN, M.S.; VIRTANEN, M.E.; ENESTAM, S.H. and LAITINEN, R.S.; *Coating Layers on Bed Particles during Biomass Fuel Combustion in Fluidized-Bed Boilers.* Energy & Fuels, 2004. 18(1): p. 127-139.

[56] ÖHMAN, M. and NORDIN, A.; *The Role of Kaolin in Prevention of Bed Agglomeration during Fluidized Bed Combustion of Biomass Fuels.* Energy & Fuels, 2000. 14(3): p. 618-624.

[57] OHMAN, M.; NORDIN, A.; SKRIFVARS, B.J.; BACKMAN, R. and HUPA, M.; *Bed Agglomeration Characteristics during Fluidized Bed Combustion of Biomass Fuels.* Energy & Fuels, 2000. 14(1): p. 169-178.

[58] BRUS, E.; OHMAN, M. and NORDIN, A.; *Mechanisms of Bed Agglomeration during Fluidized-Bed Combustion of Biomass Fuels.* Energy & Fuels, 2005. 19(3): p. 825-832.

[59] VALMARI, T.; LIND, T.M.; KAUPPINEN, E.I.; SFIRIS, G.; NILSSON, K. and MAENHAUT, W.; *Field Study on Ash Behavior during Circulating Fluidized-Bed Combustion of Biomass. 1. Ash Formation.* Energy & Fuels, 1999. 13(2): p. 379-389.

[60] VISSER, H.J.M.; VAN LITH, S.C. and KIEL, J.H.A.; *Biomass Ash-Bed Material Interactions Leading to Agglomeration in FBC.* Journal of Energy Resources Technology, 2008. 130(1): p. 011801-6.

[61] ARVELAKIS, S.; JENSEN, P.A. and DAM-JOHANSEN, K.; *Simultaneous Thermal Analysis (STA) on Ash from High-Alkali Biomass.* Energy & Fuels, 2004. 18(4): p. 1066-1076.

[62] SKRIFVARS, B.-J.; BACKMAN, R. and HUPA, M.; *Characterization of the sintering tendency of ten biomass ashes in FBC conditions by a laboratory test and by phase equilibrium calculations.* Fuel Processing Technology, 1998. 56(1-2): p. 55-67.

[63] HANSEN, L.A.; FRANDSEN, F.J.; DAM-JOHANSEN, K. and HENNING SUND, S.; *Quantification of fusion in ashes from solid fuel combustion.* Thermochimica Acta, 1999. 326(1-2): p. 105-117.

[64] DE GEYTER, S.; OHMAN, M.; BOSTROM, D.; ERIKSSON, M. and NORDIN, A.; *Effects of Non-Quartz Minerals in Natural Bed Sand on Agglomeration Characteristics during Fluidized Bed Combustion of Biomass Fuels.* Energy & Fuels, 2007. 21(5): p. 2663-2668.

[65] HOFBAUER, H.; *Scriptum zur Vorlesung Wirbelschichttechnik 2. Auflage*. Institute of Chemical Engineering. Vienna University of Technology.

[66] OTTMANN, M.; *Verbrennung biogener Brennstoffe in stationären Wirbelschichtfeuerungen*. München. Fakultät Wissenschaftszentrum für Ernährung, Landnutzung und Umwelt. Technische Universität München, 2006. Dissertation.

[67] BASU, P.; *Combustion and gasification in fluidized beds*. CRC Press Taylor & Francis Group, 2006. - ISBN 0-8493-3396-2

[68] EUROPEAN COMMISSION; *Biomass action plan SEC(2005)1573*. 2005.

[69] KALTSCHMITT, M.; MERTEN, D.; FRÖHLICH, N. and NILL, M.; *Energiegewinnung aus Biomasse*, 2003.

[70] BUNDESMINISTERIUM FÜR WIRTSCHAFT UND TECHNOLOGIE. *Gesamtausgabe der Energiedaten - Datensammlung des BMWi*. (2010). Last access: 20.09.2010. Available from: http://www.bmwi.de/BMWi/Navigation/Energie/Statistik-und-Prognosen/energiedaten.html.

[71] FACHAGENTUR FÜR NACHWACHSENDE ROHSTOFFE E.V.; *Leitfaden Bioenergie - Planung, Betrieb und Wirtschaftlichkeit von Bioenergieanlagen*, C.A.R.M.E.N., 2006.

[72] THÜRINGER LANDESANSTALT FÜR LANDWIRTSCHAFT. Last access: 2010.02.29. Available from: http://www.tll.de/nawaro/nr_tznr.htm.

[73] HÄRDTLEIN, M.; ELTROP, L. and THRÄN, D.; *Voraussetzungen zur Standardisierung biogener Festbrennstoffe*. Münster. Landwitschaftsverlag GmbH, 2004.

[74] KALTSCHMITT, M.; HARTMANN, H. and HOFBAUER, H.; *Energie aus Biomass. Grundlagen, Techniken und Verfahren*. Heidelberg. Springer, 2009. - ISBN 978-3-540-85094-6

[75] OTTMANN, M.; *Verbrennung biogener Brennstoffe in stationären Wirbelschichtfeuerungen*. München. Technische Universität München, 2005. - ISBN

[76] BANKIEWICZ, D.; YRJAS, P. and HUPA, M.; *High-Temperature Corrosion of Superheater Tube Materials Exposed to Zinc Salts.* Energy & Fuels. 23(7): p. 3469-3474.

[77] BANKIEWICZ, D.; ALONSO-HERRANZ, E.; YRJAS, P.; LAURÉN, T.; SPLIETHOFF, H. and HUPA, M.; *Role of ZnCl2 in High-Temperature Corrosion in a Bench-Scale Fluidized Bed Firing Simulated Waste Wood Pellets.* Energy & Fuels, 2011. 25(8): p. 3476-3483.

[78] KROOK, J.; MARTENSSON, A. and EKLUND, M.; *Sources of heavy metal contamination in Swedish wood waste used for combustion.* Waste management, 2006. 26: p. 158-166.

[79] DIN EN 1911: *Stationary source emissions - Determination of mass concentration of gaseous chlorides expressed as HCl*, 2008.

[80] LAURÉN, T.; *Methods and instrument for characterizing deposit buildup on heat exchangers in combustion plants*. Turku. Process Chemistry Center, Faculty of Technology, Abo Akademi, 2008. Licentiate Thesis.

[81] VDI 3955: *Assessment of effects on materials due to corrosive ambient conditions*, 1996.

[82] VAN LITH, S.C.; FRANDSEN, F.J.; MONTGOMERY, M.; VILHELMSEN, T. and JENSEN, S.A.; *Lab-scale investigation of Deposit-induced Chlorine Corrosion of Superheater Materials under Simulated Biomass-firing conditions. Part 1: Exposure at 560°C.* Energy & Fuels, 2009. 23(4): p. 3457-3468.

[83] DAVIDSSON, K.O.; STEENARI, B.M. and ESKILSSON, D.; *Kaolin Addition during Biomass Combustion in a 35 MW Circulating Fluidized-Bed Boiler.* Energy & Fuels, 2007. 21(4): p. 1959-1966.

[84] DUNN, P.D. and REAY, D.A.; *Heat pipes*. Pergamon, 1994. - ISBN 0-08-041903-8

[85] NORDSIECK, H.; LANGER, S.; MÜLLER, V. and WARNECKE, R.; *ChlorOut und Temperaturmessungen am Gemeinschaftskraftwerk Schweinfurt*. Proceedings of the conference: *VDI Fachkonferenz, Feureung und Kessel-Beläge und Korrosion- in Großfeuerungsanlagen*. Stuttgart, 2009.

[86] FISCHER, H.; *Elektrolytische Abscheidung und Elektrokristallisation von Metallen*. Berlin. Springer, 1954.

[87] DIN 1319-3: *Grundlagen der Meßtechnik*, 1996.

[88] ANDERSSON, P. and NORELL, M.; *Field test of superheater corrosion in a CFB waste boiler: Part II - Scale formation characteristics.* Materials and Corrosion, 2005. 56(8): p. 550-560.

[89] ANDERSSON, P. and NORELL, M.; *Field test of superheater corrosion in a CFB waste boiler: Part I - Metal loss characteristics.* Materials and Corrosion, 2005. 56(7): p. 449-458.

[90] HENDERSON, P.; SZAKÁLOS, P.; PETTERSSON, R.; ANDERSSON, C. and HÖGBERG, J.; *Reducing superheater corrosion in wood-fired boilers.* Materials and Corrosion, 2006. 57(2): p. 128-134.

[91] VETTER, K.J.; *Elektrochemische Kinetik*. Berlin-Dahlem. Fritz Haber Institut der Max-Planck-Gesellschaft. Springer Verlag, 1961.

[92] VETTER, K.J.; *Electrochemical kinetics*. New York Academic Press Inc., 1967. - ISBN 978-0127202501

[93] GELLINGS, P.J.; *Introduction to corrosion prevention and control for engineers*. Delft. Delft University Press, 1976. - ISBN 90-298-0600-1

[94] FORKER, W.; *Elektrochemische Kinetik*. Akademie-Verlag-Berlin Technische Hochschule Karl-Marx-Stadt, 1966.

[95] CORRMORAN GMBH. Last access: 28.08.2010. Available from: http://www.corrmoran.de.

[96] HAIDER, F.; HORN, S.; MAISCH, S.; WALDMANN, B.; SCHRUPP, D.; STÖCKER, B. and WARNECKE, R.; *Online measurement of high temperature corrosion*. Proceedings of the conference: *DVV-TOTEM Meeting* Freising, 2008.

[97] DIN EN 10028-2: *Flat products made of steels for pressure purposes - Part 2: Non-alloy and alloy steels with specified elevated temperature properties*, 2009.

[98] HAIDER, F.; HORN, S.; WALDMANN, B. and WARNECKE, R.; *Korrosionssonden-Ergebnisse zu Messungen in verschiedenen Anlagen*. Proceedings of the conference: *VDI Wissensforum: Beläge und Korrosion, Verfahrenstechnik und Konstruktion in Großfeuerungsanlagen VDI 430507*. Frankfurt am Main, 2007.

[99] DIN 51719:1997-07: *Testing of solid fuels-solid mineral fuels-dertermination of ash content*, 1997.

[100] BRUS, E.; OHMAN, M.; NORDIN, A.; BOSTROM, D.; HEDMAN, H. and EKLUND, A.; *Bed Agglomeration Characteristics of Biomass Fuels Using Blast-Furnace Slag as Bed Material.* Energy & Fuels, 2004. 18(4): p. 1187-1193.

[101] WORLD HEALTH ORGANISATION. Last access: 2010.03.05. Available from: http://www.who.int/en/.

[102] WARNECKE, R.; MÜLLER, V.; HORN, S.; HAIDER, F.; MAISCH, S.; KMETH, R.; LANG, W. and BIEGEL, W.; *Korrosion in Anlagen zur thermischen Abfallbehandlung Weiterentwicklung und Optimierung einer online Korrosionssonde. Abschlussbericht*, Vorhaben EU 46, 2009.